Spring 2022

STRATEGIES TO IMPROVE SHRINKAGE RESISTANCE OF CEMENT-BASED MATERIALS FOR EXTRUSION-BASED 3D PRINTING

Kavya Vallurupalli
Missouri University of Science and Technology

Department: Civil, Architectural and Environmental Engineering

Recommended Citation
Vallurupalli, Kavya, "STRATEGIES TO IMPROVE SHRINKAGE RESISTANCE OF CEMENT-BASED MATERIALS FOR EXTRUSION-BASED 3D PRINTING" (2022). *Doctoral Dissertations*. 3204.
https://scholarsmine.mst.edu/doctoral_dissertations/3204

STRATEGIES TO IMPROVE SHRINKAGE RESISTANCE OF CEMENT-BASED MATERIALS FOR EXTRUSION-BASED 3D PRINTING

by

KAVYA VALLURUPALLI

A DISSERTATION

Presented to the Graduate Faculty of the

MISSOURI UNIVERSITY OF SCIENCE AND TECHNOLOGY

In Partial Fulfillment of the Requirements for the Degree

DOCTOR OF PHILOSOPHY

in

CIVIL ENGINEERING

2022

Approved by:

Kamal H. Khayat, Advisor
Aditya Kumar
Dimitri Feys
Nicolas Ali Libre
V. A. Samaranayake

PUBLICATION DISSERTATION OPTION

This dissertation consists of the following four articles, formatted in the style used by the Missouri University of Science and Technology:

Paper I, found on pages 19–62, has been published in the *Cement and Concrete Composites Journal* in April 2021.

Paper II, found on pages 63–93, has been submitted to the *ACI Materials Journal.*

Paper III, found on pages 94–125, has been prepared for submission for publication.

Paper IV, found on pages 126–169, has been submitted to the *Cement and Concrete Composites Journal*.

ABSTRACT

The main objective of this study is to develop new generation of shrinkage-resistant 3D printable mortar mixtures. To this end, the research work was carried out to: i) identify key material and processing parameters that affect printability; ii) investigate the influence of water-to-cement ratio, superplasticizer dosage, and welan gum content on mortar printability; iii) propose a “printability window” where rheological properties and desorptivity can secure successful printing; iv) investigate effect of shrinkage mitigation materials (expansive agent (EA), pre-saturated lightweight sand (LWS), superabsorbent polymers (SAP), and shrinkage reducing admixture) on printability and shrinkage performance of mortar; and v) evaluate the effect of EA, LWS, steel and synthetic fibers on chloride-induced corrosion and transport properties of concrete.

The research work indicated that: i) in addition to rheology and printing parameters, desorptivity (the rate of fluid filtration during extrusion) can also present a significant influence on printability; ii) for extrusion speed of 2.5 mm/s, extruder capacity of 135 N, and nozzle size of 9 mm, the printability window encompasses yield stress of 100-470 Pa, plastic viscosity of 10-60 Pa.s, and desorptivity values $< 3\times10^{-3}\ s^{-0.5}$; iii) the use of welan gum can enable development of print materials that are most suitable for 3D printing. The addition of welan gum (up to 0.6%) significantly reduced the desorptivity, which enabled extrusion of print material with yield stress > 400 Pa and contributed to lower mass loss due to plastic shrinkage; and iv) the use of SAP is effective at reducing desorptivity and such polymers with slower absorption and desorption kinetics are more effective to ensure shape stability and efficient internal curing of print materials.

ACKNOWLEDGMENTS

Firstly, I would like to express my sincere gratitude to my advisor Dr. Kamal H. Khayat for the continuous support of my Ph.D. study and related research, for his patience, encouragement, motivation, and immense knowledge. I would like to express my gratitude to Dr. Nicolas Ali Libre for letting me use the ram extrusion test setup for performing the extrudability studies pertaining to the scope of my dissertation. I would like to thank my advisory committee members Dr. Aditya Kumar, Dr. Dimitri Feys, Dr. Nicolas Ali Libre, and Dr. V.A. Samaranayake for their time to review my work and their insightful and valuable input through this process.

My sincere thanks also go to my colleagues and friends at Missouri S&T, including Dr. Nima Farzadnia, Dr. Wiena Meng, Dr. Zemei Wu, Dr. Le Teng, Dr. Jianhui Liu, Ms. Ricarda Sposito, Mr. Haodao Li, Mr. Yucun Gu, Mr. Jingjie Wei, Mr. Alfred Addai-Nimoh, Mr. Kamran Aghaee, Mr. Xiaolong Xia, and Ms. Sara Fayek. The cooperation and support from Mr. Jason Cox, Ms. Gayle Spitzmiller, Mr. Logan Wilson, and Ms. Abigayle Sherman from Center for Infrastructure Engineering Studies, and Mr. Gary Abott from High-bay Structural Engineering Research Laboratory is greatly acknowledged.

I would like to express special appreciation for my family in India and the US for their selfless love, care, and support throughout writing this thesis and my life in general.

TABLE OF CONTENTS

Page

PUBLICATION DISSERTATION OPTION iii

ABSTRACT... iv

ACKNOWLEDGMENTS v

LIST OF ILLUSTRATIONS xii

LIST OF TABLES xv

SECTION

1. INTRODUCTION.. 1

1.1. GENERAL BACKGROUND AND RESEARCH OBJECTIVES 1

1.2. EXTRUSION-BASED 3D PRINTING PROCESS 6

1.3. SHRINKAGE OF 3D PRINTED ELEMENTS 9

1.4. CHLORIDE-INDUCED REBAR CORROSION 12

1.5. ORGANIZATION OF DISSERTATION 16

PAPER

I. EFFECT OF FLOW BEHAVIOR AND PROCESS-INDUCED VARIATIONS ON SHAPE STABILITY OF 3D PRINTED ELEMENTS – A REVIEW 19

ABSTRACT 19

NOMENCLATURE 20

1. INTRODUCTION.. 22

2. EXTRUSION-BASED 3DP: KEY MATERIAL AND PROCESSING PARAMETERS 23

2.1. PUMPING PROCESS 24

    2.1.1. Extent of Shearing in Bulk Material.. 27
        2.1.1.1. Material parameter - η_{LL}/μ_p...27
        2.1.1.2. Material parameter - τ_{dy}/μ_p..28
  2.2. EXTRUSION PROCESS 29
    2.2.1. Extent of Shearing in Print Material... 33
        2.2.1.1. Bingham number (B_N). 33
    2.2.2. Degree of Fluid Filtration and Consolidation.. 34
        2.2.2.1. Drainage number (D_c)...34
    2.2.3. Ratio of Aggregate Volume Fraction to Maximum Packing Fraction (V_s/V_{sm}).. 35
3. PRINT MATERIAL FLOW BEHAVIOR DURING 3DP 37
  3.1. PRINT MATERIAL COMPOSITION AND PROCESSING PARAMETERS 37
    3.1.1. Print Material Composition and Parameters. 38
    3.1.2. Processing Parameters.. 39
  3.2. PRINT MATERIAL FLOW BEHAVIOR DURING PUMPING.................... 40
    3.2.1. Estimation of Extent of Shearing in Bulk Material............................... 40
        3.2.1.1. Material parameter- η_{LL}/μ_p...40
        3.2.1.1. Material parameter- τ_{dy}/μ_p..44
    3.2.2. Estimation of Print Material Flow Behavior. 44
  3.3. PRINT MATERIAL FLOW BEHAVIOR DURING EXTRUSION 44
    3.3.1. Estimation of Extent of Shearing in Print Material (B_N)........................ 45
    3.3.2. Estimation of Degree of Fluid Filtration and Consolidation (D_c). 45
        3.3.2.1. Coefficient of consolidation (C_v)...46

3.3.3. Estimation of Ratio of Aggregate Volume Fraction To Maximum Packing Fraction (V_s/V_{sm}). 46

3.3.4. Estimation of Print Material Flow Behavior. 47

4. SHAPE STABILITY – MATERIAL FLOW BEHAVIOR AND PROCESS-INDUCED VARIATION 47

5. FUTURE WORK 50

6. SUMMARY 52

REFERENCES 54

II. CHARACTERIZATION OF PRINT MATERIAL EXTRUDABILITY USING RHEOLOGY AND DESORPTIVITY 63

ABSTRACT 63

1. INTRODUCTION 64

2. MATERIALS AND EXPERIMENTAL PROCEDURES 68

2.1. MATERIALS AND MIXTURE PROPORTIONS 68

2.2. RHEOLOGY 69

2.3. FLUID FILTRATION 71

2.4. RAM EXTRUSION 72

3. RESULTS AND DISCUSSIONS 73

3.1. INFLUENCE OF W/C AND WG CONTENT ON SP DEMAND 73

3.2. INFLUENCE OF MIXTURE PROPORTIONING PARAMETERS ON MATERIAL PROPERTIES 75

3.2.1. Effect of w/c. 75

3.2.2. Effect of SP Dosage. 77

3.2.3. Effect of WG Content 79

3.3. RELATIONSHIP BETWEEN MATERIAL PROPERTIES AND EXTRUDABILITY 82

3.4. STATISTICAL MODELING OF MATERIAL PROPERTIES AND EXTRUDABILITY 85

4. CONCLUSIONS 87

REFERENCES 89

III. EFFECT OF SHRINKAGE MITIGATING MATERIALS ON PRINT ABILITY AND SHRINKAGE RESISTANCE OF 3D PRINTABLE MORTAR 94

ABSTRACT 94

1. INTRODUCTION 95

2. MATERIALS AND EXPERIMENTAL PROCEDURES 99

2.1. MATERIALS AND MIXTURE PROPORTIONS 99

2.2. EXPERIMENTAL PROCEDURE 100

2.2.1. SAP Absorption (Tea Bag Method). 100

2.2.2. Rheology. 102

2.2.3. Fluid Filtration. 103

2.2.4. Ram Extrusion. 103

2.2.5. Plastic Shrinkage (Mass Loss). 103

2.2.6. Autogenous Shrinkage. 104

2.2.7. Drying Shrinkage. 104

2.2.8. Compressive Strength. 104

2.2.9. Hydration Kinetics. 105

3. RESULTS AND DISCUSSIONS 105

3.1. INFLUENCE OF SHRINKAGE MITIGATING MATERIALS AND WG ON PRINTABILITY 105

3.2. MASS LOSS IN PLASTIC STATE 108

3.3. AUTOGENOUS SHRINKAGE 110

3.4. DRYING SHRINKAGE 111

3.5. COMPRESSIVE STRENGTH 114

3.6. EARLY-AGE HYDRATION 115

4. CONCLUSIONS 117

REFERENCES 119

IV. EFFECT OF SHRINKAGE MITIGATING MATERIALS ON CHLORIDE-INDUCED CORROSION RESISTANCE OF FIBER-REINFORCED CONCRETE 126

ABSTRACT 126

1. INTRODUCTION 127

2. MATERIALS AND EXPERIMENTAL PROCEDURES 131

2.1. MATERIALS AND MIXTURE PROPORTIONS 131

2.2. SPECIMEN PREPRATION 134

2.3. EXPERIMENTAL PROCEDURE 136

2.3.1. Corrosion Test Setup and Analysis. 136

2.3.1.1. Experimental procedure. 136

2.3.1.2. Rebar corrosion analysis procedure. 137

2.3.2. Concrete Properties. 140

2.3.2.1. Drying shrinkage 140

2.3.2.2. Transport properties. 141

2.3.2.3. Mechanical properties. 142

3. RESULTS AND DISCUSSIONS 142

3.1. REBAR CORROSION 142

3.1.1. Initial Current (I_{in}). 144

3.1.2. Onset of Increase in Current (T_{onset}). 146

3.1.3. Time of Spike in Current (T_{spike}). 147

3.2. CONCRETE PROPERTIES 149

3.2.1. Drying Shrinkage. 149

3.2.2. Transport Properties. 151

3.2.2.1. Water absorption. 151

3.2.2.2. Bulk resistivity. 152

3.2.3. Mechanical Properties. 153

3.2.3.1. Compressive strength. 153

3.2.3.2. Flexural properties. 155

3.3. RELATIONSHIP BETWEEN REBAR CORROSION AND CONCRETE PROPERTIES 156

4. CONCLUSIONS 161

REFERENCES 163

SECTION

2. CONCLUSIONS AND RECOMMENDATIONS 170

2.1. SUMMARY AND CONCLUSIONS OF DISSERTATION WORK 170

2.2. RECOMMENDATIONS FOR FUTURE WORK 177

APPENDIX 180

BIBLIOGRAPHY 181

VITA 190

LIST OF ILLUSTRATIONS

SECTION Page

Figure 1.1. Extrusion-based 3DP process. 2

Figure 1.2. Poor shape stability at yield stress of 1400 Pa (left) and high shape stability at yield stress of 2000 Pa (right). 3

Figure 1.3. High quality of extruded layers at slump of 11mm. 3

Figure 1.4. Loss of adhesion between layers as a result of drying with the increase in time gap from 1 min (top) to 20 min (bottom). 5

Figure 1.5. Rebar corrosion and concrete cracking process. 15

Figure 1.6. Organization of the dissertation. 18

PAPER I

Figure 1. Pumping process and flow behavior. 27

Figure 2. Ram extrusion process. 30

Figure 3. Process-induced variations during 3DP and its effect on shape stability. 53

PAPER II

Figure 1. Ram extrusion process. 65

Figure 2. Particle size distributions for cement and sand. 70

Figure 3. Filtration test. 71

Figure 4. Extrusion test. 74

Figure 5. Influence of w/c on τ_y (left) and μ_p (right) at initial mini-slump flow of 120 mm. 76

Figure 6. Influence of w/c dosage on D_e at 20 min (left) and 90 min (right) at initial mini-slump flow of 120 mm. 76

Figure 7. Influence of SP dosage on τ_y (left) and μ_p (right). 78

Figure 8. Influence of SP dosage on D_e at 20 min (left) and 90 min (right). 79

Figure 9. Influence of WG content on τ_y (left) and μ_p (right) at initial mini-slump flow of 170 mm. 80

Figure 10. Influence of WG content on D_e at 20 (left) and 90 (right) min age (initial mini-slump flow of 170 mm). 81

Figure 11. Relationship between material properties and extrudability of mortar with τ_y of 120 (left) and 320 Pa (right). 85

Figure 12. Printability window of mortar encompassing yield stress (100-470 Pa) plastic viscosity (10-60 Pa.s) and desorptivity ($< 3x10^{-3}$ $s^{-0.5}$). 86

PAPER III

Figure 1. Particle size distributions of SAPs. 102

Figure 2. Absorption kinetics of SAPL and SAPS in filtered pore solution. 107

Figure 3. Mass loss in plastic state during first 1.2 h (left) and 24 h (right) when exposed to evaporation rate of 1.6 kg/m^2·h. 112

Figure 4. Autogenous shrinkage results of investigated mortar mixtures. 112

Figure 5. Effect of shrinkage mitigating materials and WG on drying shrinkage when sample are exposed to evaporation rate of 1.6 kg/m^2·h. 113

Figure 6. 1-d (left) and 7-d (right) compressive strength results of mortar mixtures relative to the strength of REF mixture subjected to identical curing conditions. 116

Figure 7. Rate of heat (left) and total heat flow (right) results of investigated mixtures. 116

PAPER IV

Figure 1. Particle size distribution of aggregates. 133

Figure 2. Dimensions of corrosion test sample. 135

Figure 3. Schematic of corrosion test setup. 137

Figure 4. Schematic of a) macro-cell corrosion process, b) partial cracking of concrete cover which results in onset of increase in current, and c) concrete cover cracking which results in a spike in current. 138

Figure 5. Typical macro-cell current data along with the smoothed and curvature values. 139

Figure 6. Current variation with time for individual rebars of REF-7D mixture at cover depths of a) 25 mm and b) 38 mm. 144

Figure 7. Current data (blue) at 25 mm cover along with smoothed (black), curvature (green), and corrosion indicators (red) for selected concrete mixures: a) STST+EA-7D, b) SYN+EA-7D, c) STST+EA+LWS-7D, and d) STST+EA+LWS-1D... 145

Figure 8. a) Variation of relative initial current (ratio of I_{in} for concrete at specific cover depth to I_{in} for REF-7D at same cover depth) and b) duration between onset of increase and sudden spike in current for concrete with rebar cover of 25 mm. 149

Figure 9. Strain variation with time for a) 7-d moist cured and b) 1-d moist cured samples... 150

Figure 10. Water absorption as function time for a) 7-d and b) 1-d moist cured concrete mixtures.. 154

Figure 11. Sorptivity results of investigated mixtures: a) initial sorptivity and b) secondary sorptivity.. 154

Figure 12. a) Bulk resistivity results of investigate mixtures, and b) relationship between conductivity (1/resistivity) and water absorption of steel-FRC. 155

Figure 13. a) Compressive strength, b) MOR and toughness results of investigated mixtures. 156

Figure 14. Stages of rebar corrosion and concrete cracking; key parameters affecting duration of each sub-stage are indicated. 157

Figure 15. Relationship between corrosion indicators and concrete properties. 160

LIST OF TABLES

PAPER I

Page

Table 1. Influence of key parameters on material flow behavior during pumping........... 29

Table 2. Influence of key parameters on material flow behavior during extrusion.......... 36

Table 3. Information on print materials' composition, key material and processing parameters.. 42

Table 4. Expected flow behavior during pumping stage of 3DP..................................... 45

Table 5. Expected flow behavior during extrusion stage of 3DP. 48

Table 6. Influence of print material flow behavior on shape stability............................. 51

PAPER II

Table 1. Influence of print material properties on flow behavior and extrudability......... 66

Table 2. Oxide composition of Type I/II cement... 70

Table 3. Mixture proportions and initial mini-slump flow of investigated mixtures........ 70

Table 4. Influence of mixture parameters on material properties and extrudability......... 82

Table 5. Material properties and maximum extrusion of investigated mixtures. 84

Table 6. Multiple regression analysis of extrudability results... 86

PAPER III

Table 1. Chemical composition and physical properties of powder constituents........... 101

Table 2. Mixture proportions of investigated mixtures. 102

Table 3. Material properties and maximum extrusion of investigated mixtures. 106

PAPER IV

Table 1. Chemical composition and physical properties of powder constituents........... 133

Table 2. Physical properties of aggregates. 133

Table 3. Physical properties of fibers. 133

Table 4. Mixture proportions of investigated mixtures. 134

Table 5. Corrosion indicators of investigated mixtures. 146

1. INTRODUCTION

1.1. GENERAL BACKGROUND AND RESEARCH OBJECTIVES

3D printing (3DP) has emerged as a revolutionary technology that has contributed to advancements in a wide range of industries, such as aerospace, automotive, and healthcare. Over the past decade, there has been a growing interest in 3DP of cement-based materials in concrete construction [1-3]. Concrete construction is one of the leading industries in the U.S. with annual production of 260M m^3 of ready-mixed concrete [4] and 75M m^3 of precast concrete [5]. One of the key challenges with concrete construction is the cost associated, and up to 60% of the cost is related to formwork construction and labor work associated with it [6, 7]. The use of 3DP technology in concrete construction eliminates the need for formwork and reduces the cost associated with it and improves work safety. 3DP can also increase the architectural freedom while minimizing the material usage and the error in the construction process and reducing the construction time [6, 8].

3DP of cement-based materials is typically done using two different techniques, i.e., particle-bed binding (also known as binder jetting) and material extrusion [9, 10]. Depending on the technique selected, the key material properties that influence the printability (i.e., suitability of the material for 3DP process) vary [11] and the current work focuses on 3DP using the extrusion-based technique. The extrusion-based 3DP involves the extrusion of cement-based material through a printhead nozzle into filaments, which are deposited layer-by-layer at a controlled speed [12, 13] by an automated system, as illustrated in Figure 1.1.

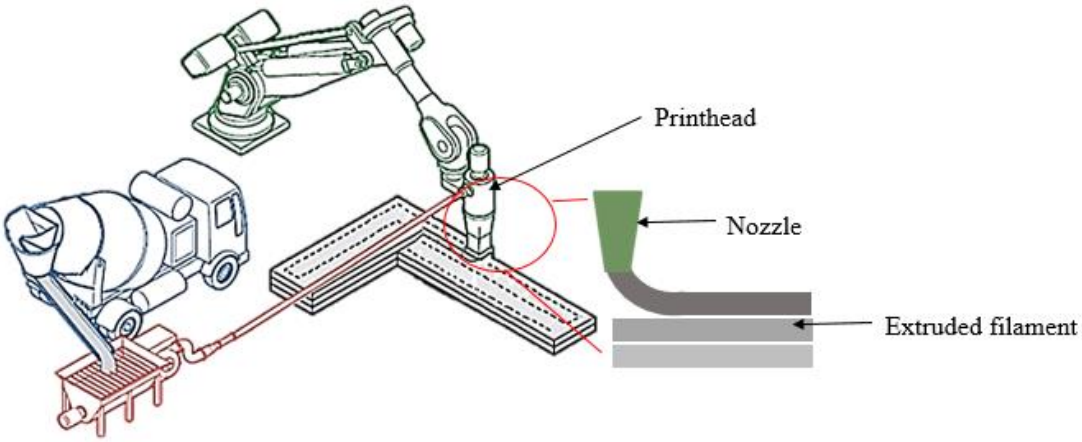

Figure 1.1. Extrusion-based 3DP process.

The processing steps involved during extrusion-based 3DP are: a) transport of the print material (either mixed on-site or premixed) to the printhead (also referred to as extruder); b) the extrusion of the material by the printhead; and c) the deposition of extruded material into layers. The transportation of the print material to the printhead typically requires pumping of the material through a pipeline. The extrusion is performed by forcing the print material through a ram or screw-type extruder [14-16] and the extruded material is deposited into layers by the printhead. In this study, a ram extruder was used. During pumping and extrusion, the print material is subjected to shearing, and as a result, typically lower yield stress and viscosity are preferred for the material to reduce the force needed for pumping and extrusion [17]. At the same time, the material must be self-supporting after extrusion as there is no formwork to offer support. Low yield stress of the print material can result in poor shape stability of the printed layers [18], as illustrated in Figure 1.2. The use of high yield stress can cause blockage in the extruder and lead to extrusion of filaments with poor quality, as illustrated in Figure1.3.

This can have a detrimental effect on mechanical and transport properties of the printed elements. Tailoring the material properties to meet these contradictory requirements is one of the key challenges with application of 3DP to concrete construction.

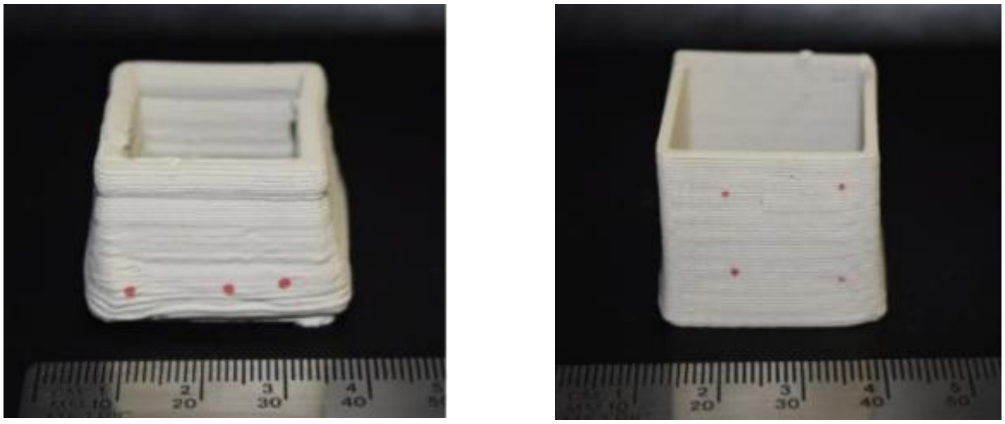

Figure 1.2. Poor shape stability at yield stress of 1400 Pa (left) and high shape stability at yield stress of 2000 Pa (right) [19].

Figure 1.3. High quality of extruded layers at slump of 11mm i.e., low yield stress (left) and poor quality of extruded layers at slump of 6 mm i.e., high yield stress (right) [20].

Furthermore, to meet the contradictory requirements for material properties during 3DP, the print materials often include the use of supplementary cementitious materials such as fly ash [13, 21] and silica fume [22] as partial replacement of portland cement [23-27]. From a rheological point of view, the use of supplementary cementitious materials can enhance particle packing density [13, 28] thereby reducing viscosity and consequently the force needed for extrusion [29, 30]. Rapid setting cement i.e., calcium sulphoaluminate was used to increase the rate of structural buildup thereby improving shape stability [23-27]. The water-to-binder ratio of the print materials was kept low (typically < 0.4) to increase the rheological properties and shape stability [31, 32]. Additionally, different types of chemical admixtures, such as superplasticizers, retarders, and rheology-modifying admixtures were used. Superplasticizers were incorporated to ensure dispersion of binder thereby enhancing particle packing density and lowering w/b [33-35]. Retarders were used to delay the hydration kinetics of the cement-based materials to extend the time window during which the material can be printed [36-39]. Rheology-modifying admixtures such as viscosity-modifying and thixotropy-enhancing admixtures were used to improve the shape stability of the extruded material [40-43] and increase the water retentivity of print material [44]. Relatively smaller aggregates (lower maximum aggregate size) and lower aggregate contents were used to prevent blockage at the nozzle entry during extrusion [45-49]. The particle size distribution and volume fraction of the aggregate were selected primarily to optimize particle packing density of aggregate [30] or total solid particles (i.e., aggregate + binder) [13, 28].

The relatively low w/b and high binder content of print material can increase the risk of early-age shrinkage cracking [50]. The lack of coarse aggregate, the high surface-to-volume ratio of the printed layers, and the absence of formwork also increase the susceptibility of the printed element to drying [51]. Drying of printed layers can also hinder hydration, ultimately impairing the strength of the printed elements [44]. The drying of layers during printing can result in poor adhesion between the layers leading to high porosity at the interface [52], as shown in Figure 1.4. The differential shrinkage deformation in the layers can result in residual stresses in the printed elements resulting in poor interlayer bond and cracking [53]. The increased porosity at the interface as a result of drying and shrinkage cracking can increase the possibility of ingress of various deleterious substances into printed elements consequently shortening the design life of the structure. Despite this understanding, limited emphasis was placed in the 3DP literature on assessment and improvement of printed elements' shrinkage resistance.

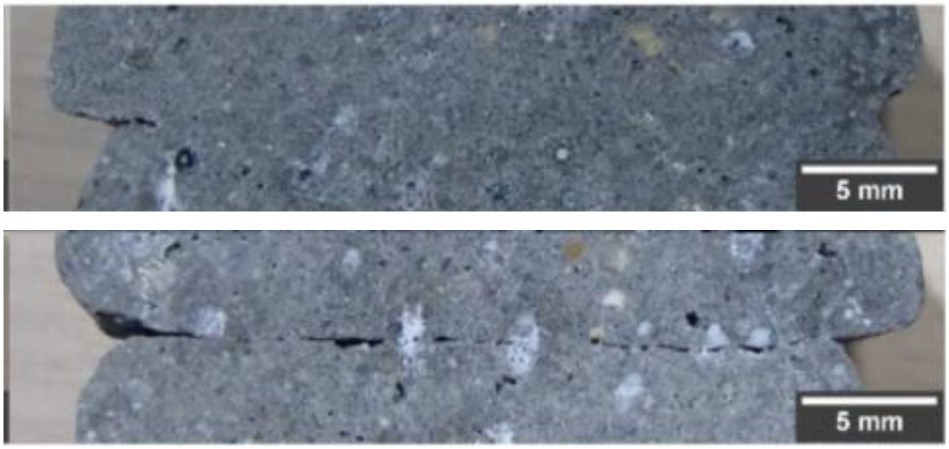

Figure 1.4. Loss of adhesion between layers as a result of drying with the increase in time gap from 1 min (top) to 20 min (bottom) [54].

3DP can offer numerous benefits in terms of structural, environmental, and safety aspects of construction. To facilitate the implementation of 3DP technology in concrete construction and realize its potential benefits, this project aims to develop 3D printable shrinkage-resistant mortars. To this end, the research work contained in this dissertation was carried out to: i) identify the key material properties and processing parameters that affect the printability of mortar mixtures; ii) investigate the influence of water-to-cement ratio, superplasticizer dosage, and welan gum content on extrudability and shape stability of mortar mixtures; iii) develop printability window i.e., suitable ranges of material properties for successful extrusion-based 3DP; iv) investigate the effect of shrinkage mitigation materials i.e., expansive agent, pre-saturated lightweight sand, super absorbent polymers, and shrinkage reducing admixture on printability and shrinkage performance of printable mortar mixtures; and v) evaluate the effect of the expansive agent, pre-saturated lightweight sand, steel and synthetic fibers on chloride-induced rebar corrosion and transport properties concrete mixtures exposed to drying. In the following sub-sections 1.2 to 1.4, the background information necessary to understand the research work in this dissertation is presented.

1.2. EXTRUSION-BASED 3D PRINTING PROCESS

As shown in Figure 1.1, the transportation of the print material to the printhead often requires pumping of the material through a pipeline and extrusion can be performed by forcing the print material through a ram-type extruder. The print material's flow behavior during pumping and extrusion stages is important, as it can have a significant impact on the rheology and quality of the extruded material (i.e., different material composition compared to the material before it is subjected to pumping and extrusion). The extruded material is deposited into layers by the printhead, and the shape stability of these printed layers is a function of the extruded material properties and their variations with time, printing speed, and geometrical characteristics of the printed element [18, 55, 56]. Different flow behaviors could occur for cement-based materials during pumping and extrusion stages of 3DP depending on the material and processing parameters in use. Understanding the flow behavior of the print material during pumping and extrusion helps characterize the variations in material properties during these critical stages of 3DP and provides valuable information on the material characteristics to consider for the formulation of 3D printable mixtures.

During pumping, the application of pressure results in shear stress difference across the cross-section of the pipeline (i.e., high shear stress at the pipeline wall and zero shear stress at the center of the pipeline)**.** This gradient in shear stress causes migration of relatively large aggregate particles to the lower shear rate region (i.e., towards the center of the pipeline), leaving a more fluid micro-mortar layer near the pipe wall [57]. The migration of the aggregates can occur when the aggregate volume fraction is lower than 0.8 times the maximum particle packing fraction [58-60]. The lack of such migration can result in blockage within the pipeline [61-63]. The micro-mortar layer that forms during shearing at the pipe wall is known as the “lubrication layer (LL)”, and the remaining material is known as the “bulk material”. The LL undergoes shearing during pumping owing to its relatively low yield stress and viscosity [64-66]. In addition to LL, the bulk material can undergo shearing and the extent of shearing depends on the rheology of the bulk material, the pumping rate, and pipeline dimensions [67]. In the absence of shearing of bulk material, the material flow behavior during pumping is referred to as ‘plug flow’. Alternatively, the shearing of both LL and bulk materials is referred to as ‘shearing flow’.

During ram extrusion, the material is filled in a barrel, and force is applied on the ram to push the material into a contraction i.e., nozzle. The application of extrusion force results in the shearing of the material along the barrel wall while the remaining material close to the center moves along unsheared. At low shearing, only the material close to the barrel wall is sheared, while the remaining material moves along the extruder un-sheared. The extrusion flow behavior in such a case is described as ‘plastic’ [68-70].

Alternatively, at high shearing, most of the material in the barrel undergoes shearing, and the extrusion flow behavior in such case is described as ‘visco-plastic’ [69, 71, 72]. The extent of shearing depends on the rheology of the print material, extruder dimensions, and extrusion speed [69].

During the plastic and visco-plastic flow, the print material stays homogenous in the barrel. However, the existence of a pressure gradient between the ram and nozzle entry and the confinement of the material within the barrel (between the ram and nozzle) can result in material heterogeneity. The pressure gradient causes fluid filtration and consolidation of the material located near the ram. The extrusion of this consolidated material would require a significant increase in extrusion force and may lead to blockage within the extruder [73-75]. This flow behavior is classified as ‘frictional-plastic’. The extent of fluid filtration depends on desorptivity i.e., rate at which fluid drains out of material under pressure [76, 77]. This phenomenon is also observed for print material with high concentration of aggregate i.e., aggregate volume fraction is close to or greater than 0.8 times the maximum particle packing fraction. In such a case, the application of extrusion force results in aggregate interlocking and fluid filtration through granular skeleton of the aggregate [58-60].

The shape stability of the extruded printed elements is a function of yield stress, elastic modulus of the extruded material and their variations with time, as well as the printing speed, geometry and dimensions of individual layers and the printed element [55, 56, 78]. The yield stress and elastic modulus and their variation with time are a function of material constituents [79, 80], as well as the flow history of the material [81, 82]. The flow history for the extruded material includes the extent of shearing in the bulk material during pumping as well as the extent of shearing and the degree of filtration and consolidation during extrusion. In other words, if the material undergoes significant shearing during pumping and extrusion, the shearing results in structural breakdown and lower rheological properties for the printed material. Furthermore, the shearing can also result in increased temperature and changes in the air content of the material thereby impacting the rheology of extruded material. Additionally, the fluid filtration during extrusion can result in higher water content for the extruded material suggesting decreased rheological properties and poor mechanical and durability performance. Understanding this dependency of the printed material performance on the 3DP process and the changes in material flow behavior during 3DP is key for determining the optimum processing parameters and printing material properties that could lead to successful 3DP.

In Paper I, the material flow behavior during pumping and extrusion and its influence on process-induced variations on shape stability of the printed elements is discussed in detail. This information was used to identify the strategies that can be implemented to reduce the negative impact of the pumping and extrusion on shape stability. In Paper II, these strategies are utilized for the development of mortar mixtures that can be extruded into shape stable filaments.

1.3. SHRINKAGE OF 3D PRINTED ELEMENTS

The 3D printed layers in the fresh state are exposed to the environment due to the lack of formwork. This causes evaporation of the water and consequent shrinkage of the printed layers in plastic state i.e., plastic shrinkage. Typically for cement-based materials, at the early ages i.e., during the 1 h, the bleed water is transported to the specimen surface and the evaporation occurs mainly from the bleed water [83]. Once the bleed water is consumed by evaporation, the rate at which bleed water forms can no longer compensate for the water lost due to evaporation. This results in the formation of menisci, and this exerted capillary tensile stresses in the pore system [84, 85]. These tensile stresses cause shrinkage and can have a detrimental effect on the hydration process. Furthermore, if the shrinkage is restricted, cracking could occur which can have a detrimental effect on the transport properties of printed elements.

In addition to plastic shrinkage, the low water-to-binder ratio and high volume of paste content of print material also result in self-desiccation due to the consumption of water from the pores during the hydration process. In the absence of exchange of moisture with the external environment and at a constant temperature, the shrinkage in the test specimens due to self-desiccation is referred to as autogenous shrinkage. Similar to the plastic shrinkage, the drying of the pore system and consequent shrinkage occurs in the hardened cement system over an extended period and this shrinkage is referred to as the drying shrinkage.

Various shrinkage mitigating materials such as expansive agents, internal curing agents (lightweight sand and superabsorbent polymers), shrinkage reducing admixtures, and fibers have been successfully employed in literature to reduce the shrinkage of cement-based materials in conventionally cast applications [33, 86-88]. In this study, CaO-based expansive agents, pre-saturated lightweight sand, superabsorbent polymers, steel and synthetic fibers are used to improve the shrinkage resistance of mortar and concrete mixtures. The hydration of CaO-based expansive agent results in the formation of calcium hydroxide (CH) crystals. The growth of CH crystals exerts expansive stress on concrete at an early age which compensates for the shrinkage of cement-based materials [89]. The pre-wetted lightweight sand can supply the water needed for curing concrete internally thereby compensating for the water lost during drying or due to hydration [90]. The superabsorbent polymers can absorb and retain water from the matrix which can then be released upon the drop in the relative humidity of the matrix [91]. The shrinkage reducing admixtures can reduce the surface tension of pore solution [83, 92], and this results in the reduction in the capillary pressure exerted on the pore system and the resulting shrinkage. The fibers can reduce the cracking potential of concrete due to plastic and drying shrinkage [93, 94].

In addition to their individual effects, a favorable shrinkage-compensating effect was observed by [93]with the use of expansive agents along with fibers. This is due to the chemical prestressing effect of the expansive agent on fibers. An improvement in the shrinkage mitigation was reported by [95] when using expansive agent along with lightweight sand due to a significant increase in the hydration of expansive agent with an increase in the amount of water available in the matrix in the presence of pre-wetted lightweight sand. A significant reduction in autogenous shrinkage of mortar mixtures was reported by [96] with the combined use of superabsorbent polymers and shrinkage reducing admixtures. This was attributed to the internal curing provided by superabsorbent polymers and reduction in surface tension of pore solution by the shrinkage reducing admixture. The beneficial effect of the individual and combined shrinkage mitigation methods is well documented in the literature, however, less attention was given to the effect these shrinkage mitigating materials on transport properties [88].

Furthermore, to facilitate their use for 3DP application, the influence of the shrinkage mitigating materials on the material properties that govern printability needs to be evaluated. In Paper III, the influence of CaO-based expansive agent, pre-saturated lightweight sand, superabsorbent polymers, and shrinkage reducing admixture on the printability of mortar mixtures as well as plastic, autogenous, and drying shrinkage is investigated. In Paper IV, the individual and combined effect of the CaO-based expansive agent, pre-saturated lightweight sand, steel and synthetic fibers on the drying shrinkage, chloride-induced rebar corrosion resistance, and transport properties of concrete mixtures is assessed.

1.4. CHLORIDE-INDUCED REBAR CORROSION

The mechanism of the chloride-induced macro-cell corrosion process and the progress of cracking in concrete cover as a result of rebar corrosion is summarized in this section. The background information presented here is utilized in Paper IV to evaluate the influence of shrinkage mitigating materials and fibers on the chloride-induced corrosion resistance of concrete mixtures.

The chloride-induced macro-cell corrosion process involves two phases i.e., corrosion initiation and propagation phase [97]. During the corrosion initiation phase, the detrimental Cl^- permeates through concrete and this causes the breakdown of the passive layer that forms on the rebar as a result of the high pH of the concrete pore solution. The breakdown of the passive layer occurs once the Cl^-concentration at the rebar-concrete interface reaches a critical value. The time needed for the Cl^- to penetrate through concrete and reach the critical concentration at the interface is referred to as the corrosion initiation phase [98]. The corrosion initiation phase is a function of the transport properties of concrete cover and critical chloride concentration [99]. The rate of transport of detrimental agents depends on the sorptivity, permeability, diffusivity, and electrical conductivity of the bulk concrete, quality of the porous zone at the rebar-concrete interface, and concrete cover depth [99].

The de-passivation results in the dissolution of iron (Fe^{+2}) at the anode (rebar) and the flow of the electrons released at the anode through the electrical connection to the cathode (stainless steel mesh) which results in the oxygen reduction reaction at the cathode i.e., formation of OH^- [97]. The Fe^{+2} and OH^- react to form the ferrous hydroxide which further hydrates to form the expansive corrosion products. These products exert expansive stresses on concrete and initiate cracking at the rebar interface when the tensile stress exerted by the corrosion products exceeds the tensile strength of surrounding concrete [100, 101]. The cracking at the interface increases the rate of transport of Cl^-, Fe^{+2}, and OH^- ions and this can further increase the rate of corrosion product formation [102]. The expansive pressure generated by the products results in crack propagation and ultimately complete cracking of concrete cover [103]. The time from the de-passivation of the rebar to the complete cracking of concrete cover is referred to as the corrosion propagation phase.

The propagation phase of corrosion can be further divided into four sub-phases based on the extent of deterioration of concrete cover [104]. These four sub-phases are: free expansion of the corrosion product, stress initiation on the concrete cover, partial and complete cracking of the concrete cover. The corrosion rate (i.e., current) variation with time for the rebar exposed to chlorides along with the four sub-phases of corrosion propagation phase is shown in Figure 1.5.

During the free expansion phase, the corrosion products gradually occupy the porous regions at the rebar-concrete interface (i.e., pre-existing cracks in the concrete due to the shrinkage stresses, entrapped and entrained air voids, and capillary voids in the paste matrix) and do not exert any tensile stress on the surrounding concrete. As a result, no significant changes occur in the current during this phase (as shown in Figure 1.5) and the duration of this stage depends on the volume of interconnected pores present around the rebar as well as the rate of corrosion product formation which is in itself a function of concrete porosity and pore connectivity [101].

As the concrete porous regions are occupied with the corrosion products, the further increase in the corrosion products exerts expansive pressure on the surrounding concrete and this sub-phase is known as the stress initiation phase. During this stage, the expansive pressure on concrete continues to increase, however, no significant cracking occurs within the concrete cover. As a result, no significant changes occur in the current at the onset of the stress initiation phase, as shown in Figure 1.5. The duration of the stress initiation phase (in Figure 1.5) depends on the tensile strength of concrete and the expansive stress exerted by the corrosion products on concrete. The expansive stress exerted by the corrosion products is a function of the rate of corrosion product formation, rebar diameter, concrete cover depth, and concrete properties (i.e., elastic modulus, creep coefficient, and Poisson’s ratio) [100, 101].

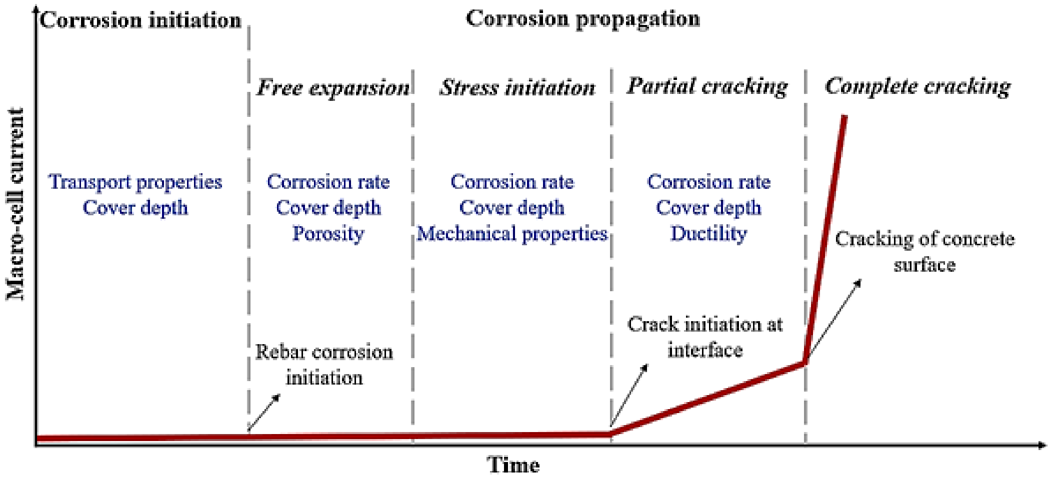

Figure 1.5. Rebar corrosion and concrete cracking process. Key parameters affecting the duration of each phase of corrosion are shown in blue.

The expansive pressure continues to increase with the formation of corrosion products and when the tensile stress exerted by the corrosion products exceeds the tensile strength of surrounding concrete, cracks will be initiated in the concrete starting from the interface towards the concrete surface and this sub-phase is referred to as ‘partial cracking of concrete cover’. At this stage, concrete at the interface is cracked while the concrete close to the surface is uncracked i.e., no sign of surface cracking. However, the cracking at the interface results in a decrease of the cell resistance leading to an onset of increase in current as shown in Figure 1.5. The duration of the partial cracking stage (in Figure 1.5) depends on the rate of corrosion product formation, concrete cover depth, and residual strength of cracked concrete i.e., ductility of concrete [104].

The internal cracking of concrete increases the penetration rate of the detrimental agents which leads to further growth of the corrosion products. The expansive pressure generated by the products results in crack propagation and ultimately causes complete cracking of concrete cover. This sub-phase is called the ‘complete cracking of concrete cover' and the onset of this phase results in a sudden spike in the current results as shown in Figure 1.5. The onset of this phase is also evident from the presence of rust stains and cracking on the surface of the concrete cover. Different phases of the corrosion and concrete deterioration, and the key material parameters affecting the duration of each phase are summarized in Figure 1.5.

1.5. ORGANIZATION OF DISSERTATION

The general introduction to the extrusion-based 3DP process, the advantages of using 3DP technology in concrete construction, the key challenges that need to be addressed to make 3DP a viable alternative to conventional concrete construction, and the relevant background information pertaining to the research work carried out are presented in Section 1. This dissertation document is comprised of four papers that have already been published, submitted, or prepared for publication. The organization of this dissertation is illustrated in Figure 1.6.

In Paper I, a comprehensive review of the processing stages of 3DP i.e., pumping and extrusion, is carried out. The print material flow behavior during pumping and extrusion stages of 3DP and key material and processing parameters that govern the flow behavior are identified. The influence of the flow behavior and process-induced variations in material properties on the shape stability is highlighted. The strategies that can be implemented to reduce the negative impact of the pumping and extrusion on shape stability are suggested. Future work needed for better prediction of material flow behavior during 3DP and influence of process-induced variations on shape stability of the printed elements is recommended.

In Paper II, the influence of rheology and fluid filtration characteristics of mortar mixtures on extrudability are evaluated and printable mortar mixtures are developed. A printability window i.e., the acceptable ranges of material properties within which the material can be extruded into shape-stable layers is determined.

In Paper III, the shrinkage resistance and compressive strength performance of 3D printable mortar mixtures are evaluated. The influence of shrinkage mitigating materials i.e., expansive agent, internal curing agents (lightweight sand and superabsorbent polymers), and shrinkage reducing admixture on the printability and their potential to improve the plastic, autogenous, and drying shrinkage of the printable mortar mixtures is studied.

In Paper IV, the influence of the expansive agent, lightweight sand, steel and synthetic fibers on the chloride-induced rebar corrosion and its associated cracking of concrete as well as the drying shrinkage, transport properties, and mechanical performance are explored. This study is conducted on concrete mixtures used in conventional concrete applications. However, the findings of this paper i.e., the influence of shrinkage mitigating materials on the rebar corrosion resistance, transport properties, drying shrinkage, and mechanical performance can be applied to 3DP application.

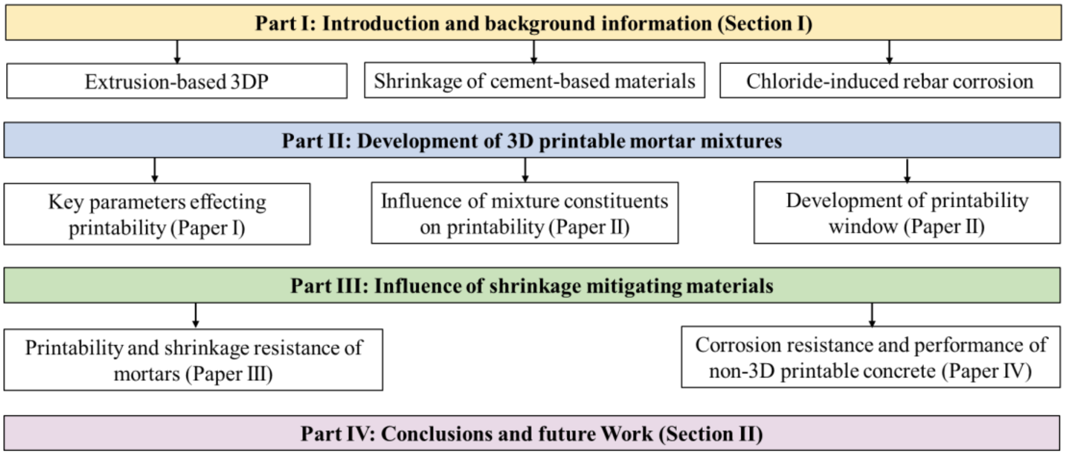

Figure 1.6. Organization of the dissertation.

PAPER

I. EFFECT OF FLOW BEHAVIOR AND PROCESS-INDUCED VARIATIONS ON SHAPE STABILITY OF 3D PRINTED ELEMENTS – A REVIEW

Kavya Vallurupalli, Nima Farzadnia, Kamal H. Khayat*

Department of Civil, Architectural and Environmental Engineering, Missouri University of Science and Technology, Rolla, Missouri, USA

*Corresponding author

ABSTRACT

Successful implementation of extrusion-based 3D printing (3DP) of concrete requires knowledge of material flow behavior during pumping and extrusion and its influence on shape stability of printed elements. Limited emphasis exists on flow behavior and process-induced variations in material properties (rheology and composition) during printing. This paper delineates the effect of flow behavior and process-induced variations on shape stability. A comprehensive review of material flow behavior during pumping and extrusion is discussed, and its influence on shape stability of 3DP elements is highlighted. The extent of shearing in print material is shown to govern process-induced variations during pumping and extrusion. During extrusion, the degree of filtration and consolidation plays a significant role on shape stability. Accurate assessment of process-induced changes in material properties is required to ensure steady and continuous flow of material during 3DP and secure proper shape stability of printed elements.

Keywords**:** 3D printing; Extrusion; Process-induced variations; Pumping; Shape stability.

NOMENCLATURE

μ_P	Plastic viscosity of cement-based material (Pa.s)
μ_{PLL}	Plastic viscosity of lubrication layer (Pa.s)
A_{fines}	Total surface area of dry powders (cm^2/m^3)
B_E	Ratio of nozzle entry diameter to maximum size of aggregate
BF_{bi}	Blaine fineness values each binder component
B_N	Bingham number
Cv	Consolidation coefficient (m^2/s)
D_B	Barrel diameter (m)
D_c	Drainage number
d_{min}	Minimum size of aggregate (m)
D_N	Nozzle diameter (m)
$D_{N\text{-}entry}$	Nozzle entry diameter (m)
$D_{N\text{-}exit}$	Nozzle exit diameter (m)
e	Material porosity
E	Elastic modulus of cement-based material (Pa)
F_E	Extrusion force (N)
L_{DZ}	Dead-zone length (m)
L_E	Extruder length (m)
L_N	Nozzle length (m)

L_P	Pipeline length (m)
M_{bi}	Mass of each binder component
η_{LL}	Viscous constant of lubrication layer (Pa.s/m)
P_P	Pumping pressure (Pa)
Q_P	Pumping rate (m^3/s)
R_P	Pipeline radius (m)
T_E	Extrusion time (s)
V_{cr}	Critical volume fraction of aggregate (%)
V_{Ph}	Printhead speed (m/s)
V_R	Extrusion speed (m/s)
V_s	Volume fraction of aggregate (%)
V_{sm}	Maximum aggregate packing fraction (%)
γ'_{max}	Maximum shear rate acting on cement-based material (1/s)
τ_B	Shear stress at boundary of lubrication layer and bulk material (Pa)
τ_{BW}	Shear stress at barrel wall (Pa)
τ_{BW0}	Shear stress at barrel wall at start of extrusion (Pa)
τ_{dy}	Yield stress of cement-based material (Pa)
τ_{dyLL}	Yield stress of lubrication layer (Pa)
τ_{PW}	Shear stress at pipeline wall (Pa)
τ_{sy}	Static yield stress of cement-based material (Pa)
φ	Internal frictional angle of cement-based material
φ_N	Angle of nozzle

1. INTRODUCTION

The 3D printing (3DP) of cement-based materials involves adding the material layer-by-layer to build complex geometrical shapes based on a digital model of the printed element with limited or no need for formwork. Recently, there has been a growing interest in 3DP of cement-based materials in concrete construction. The use of 3DP can increase architectural freedom and work safety, minimize material usage, and reduce construction time, labor and formwork cost [1, 2]. Commonly used 3DP methods for concrete construction include material extrusion and particle-bed binding (also known as binder jetting) [3, 4]. In the material extrusion method, the print material is extruded through a nozzle into filaments, which are deposited layer-by-layer at a controlled printing speed [5-7]. While the particle-bed binding method involves layer-by-layer placement of a particle material bed and selective deposition of a binder liquid onto the particle-bed [8-10]. Depending on the 3DP method used, the processing stages associated with printing and material parameters that govern the flow behavior vary. Compared to particle-bed binding, the material extrusion method has been successfully implemented in 3DP of large-scale structures [11-13]. This paper focuses on 3DP of cement-based materials using the extrusion method.

Despite the successful implementation of extrusion-based 3DP (simply referred as 3DP in this paper) for concrete construction, the detailed knowledge about the influence of the 3DP process on the shape stability of the printed elements is limited. Limited emphasis is placed on the material flow behavior during processing stages of 3DP and its influence on material rheology and composition of the extruded material. Such changes in material rheology and composition are referred to as process-induced variations. In the current 3DP literature, the print material formulation is done based on shape stability requirements for the extruded material [14-18]. The 3DP processing parameters such as the extrusion and printing speeds are often selected on trial and error basis [19-21]. Further studies are required to determine the optimum parameters that could lead to printing of shape-stable elements while reducing the printing time.

This paper reviews the different flow behaviors that could occur for print materials during the pumping and extrusion stages of 3DP. Key material and processing parameters that govern the flow behavior of the print material are also identified. Additionally, the influence of the process-induced variations in material properties on the shape stability is highlighted. Future work needed for better prediction of material flow behavior during 3DP and influence of process-induced variations on shape stability of the printed elements is recommended.

2. EXTRUSION-BASED 3DP: KEY MATERIAL AND PROCESSING PARAMETERS

The processing steps involved during 3DP are: a) transport of the print material (either mixed on-site or premixed) to the printhead (also referred to as the extruder); b) extrusion of the material by the printhead; and c) deposition of extruded material into successive layers. The transportation of the print material to the printhead typically requires pumping of the material through a pipeline. The extrusion is performed by forcing the print material through a ram or screw-type extruder [22-24]. The extruded material is deposited into layers by the printhead, and the shape stability of these printed layers is a function of the extruded material properties and their variations with time, printing speed, and geometrical characteristics of the printed element [20, 25, 26]. The pumping and extrusion processes can cause variations in material properties compared to their characteristics before being pumped. Different flow behaviors could occur for cement-based materials during pumping and extrusion stages of 3DP depending on the material and processing parameters in use. Understanding the flow behavior of the print material during pumping and extrusion helps characterize the variations in material properties during these critical stages of 3DP

2.1. PUMPING PROCESS

Extending the 3DP technique to large-scale concrete construction would require pumping for the continuous transport of print material to the printhead. The flow behavior during pumping can have a significant influence on the properties of the pumped material [27-29], and quality and shape stability of the extruded material. During pumping, given pipeline of length (L_P) and radius (R_P), the application of pressure results in shear stress difference across the cross-section (i.e., high shear stress at the pipeline wall (τ_{PW}) and zero shear stress at the center of the pipeline), as illustrated in Figure 1a**.** This gradient in shear stress causes migration of relatively large aggregate particles to the lower shear rate region (i.e., towards the center of the pipeline), leaving a more fluid micro-mortar layer near the pipe wall [30]. This micro-mortar layer is known as the “lubrication layer (LL)”, and the remaining material is known as the “bulk material”, as shown in Figure 1b.

The LL offers less resistance to shearing compared to bulk material owing to the relatively low yield stress (τ_{dyLL}) and viscosity (μ_{PLL}) of LL [28, 31, 32]. In addition to LL, the bulk material can undergo shearing, depending on the shear stress acting at the boundary (τ_B) between the LL and bulk material (in Figure 1b). If the τ_B is lower than the bulk material's yield stress (τ_{dy}), the bulk material remains un-sheared during pumping and moves along the pipeline as a 'plug'. The velocity profile for the plug flow behavior is shown in Figure 1c.

Alternatively, if the $\tau_B > \tau_{dy}$, then the portion of bulk material closer to the boundary undergoes shearing, while the remaining bulk material moves along as a plug. The flow behavior in such a case can be described as 'shearing flow', and its velocity profile is shown in Figure 1d.

For some cement-based materials with a high aggregate volume fraction (V_s), the pumping process may not induce the formation of LL. In this case, the shearing happens primarily in the bulk material when $\tau_{PW} > \tau_{dy}$. However, the application of shear stress on such highly concentrated materials results in aggregate interlocking leading to blockage in the pipeline [29, 33, 34]. As a result, the cement-based materials with high V_s are not suitable for large-scale 3DP, where pumping of the material to the printhead is needed.

The green region in Figure 1c and Figure 1d refers to the un-sheared bulk material that moves along the pipeline at constant velocity. In case of a plug flow (Figure 1c), the entire bulk material is un-sheared, and as a result fewer changes are expected in the material rheology during pumping [27]. For shearing flow (Figure 1d), the shearing in the bulk material typically results in a structural breakdown and drop in yield stress and viscosity of the material during the pumping process [27]. The structural breakdown is due to the partial breaking of connections between the particles formed by flocculation and hydration [35-38]. Therefore, the degree of drop in yield stress and viscosity during pumping depends on the extent of shearing in the bulk material (i.e., shearing rate).

Cement-based materials for 3DP are designed to have high structural buildup at rest (i.e., high rate of flocculation and hydration) following extrusion to meet the shape stability requirements of printed layers. Structural buildup can also occur in the un-sheared bulk material during pumping. In case of plug flow during pumping, this can lead to an increase in yield stress and viscosity of the print material. Similarly, during shearing flow an increase/decrease in rheological properties could occur depending on the extent of shearing in the bulk material.

In addition to the structural breakdown and buildup, an increase in the extent of shearing leads to higher viscous heat dissipation leading to an increase in material temperature [39] as well as dissolution or incorporation of air into the bulk material leading to changes in air content [35, 40, 41]. These changes in temperature and air content can also influence the rheology of the pumped material [42-44].

Based on the above information, the flow behavior of the print material during pumping and the resulting process-induced variations are shown to depend mainly on the extent of shearing in the bulk material. Therefore, key material and processing parameters that affect the extent of shearing are discussed below.

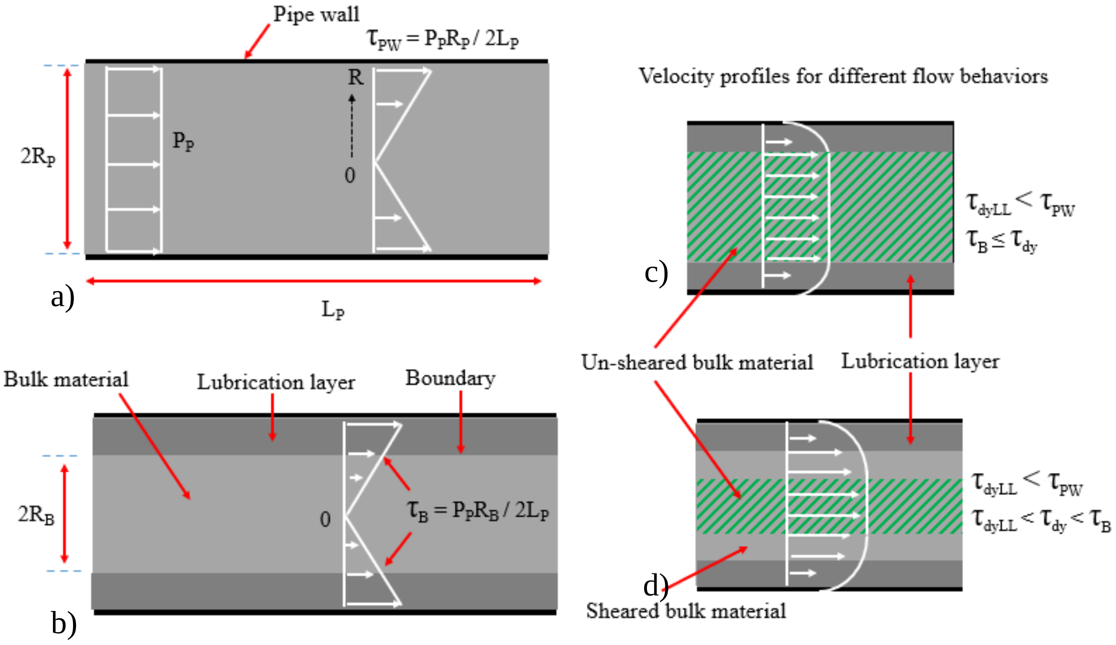

Figure 1. Pumping process and flow behavior: a) schematic of pumping process; b) shear stress distribution across pipeline cross-section and formation of LL; c) velocity profile during plug flow; and d) velocity profile during shearing flow. Regions in green indicate un-sheared bulk material during pumping.

2.1.1. Extent of Shearing in Bulk Material. The extent of shearing in the bulk material depends on bulk material rheology (i.e., τ_{dy} and plastic viscosity (μ_P)), LL thickness and μ_{PLL}, and processing parameters (i.e., R_P and pumping rate (Q_P)) [27]. The ratio of μ_{PLL} to LL thickness is known as the viscous constant of LL (η_{LL}). Based on the theoretical and experimental analysis reported by Feys [27], for fixed material parameters (i.e., fixed τ_{dy}, μ_P, and η_{LL}), the extent of shearing in the bulk material increases with the increase in Q_P and decrease in R_P. Additionally, for fixed Q_P and R_P, the extent of shearing in the bulk material increases with an increase in η_{LL}/μ_p and decrease in τ_{dy}/μ_p.

2.1.1.1. Material parameter - *η_{LL}/μ_p*. The lower values of η_{LL}/μ_p indicate easier formation of LL during pumping. The parameter η_{LL}/μ_p depends on the amount of paste that can be filtered through the material under the application of pressure [39] as well as the amount of space available within the material for shear-induced migration of aggregate under pressure [28, 45]. Secrieru et al. [39] showed that the amount of paste that can filter-out of the material increases with the decrease in μ_P and increase in the amount of free water available in the material. Such water can vary with the total surface area of dry powder (A_{fines}). The high values of μ_P and A_{fines} result in less filtration of the paste and hence lower LL thickness leading to a higher value of η_{LL}/μ_p.

Choi et al. [28] and Spangenberg et al. [45] reported that aggregate migration occurs when V_s is lower than a critical value (V_{cr}). The value of V_{cr} for cement-based materials is estimated to be equal to $0.8V_{sm}$ [46-48], where V_{sm} is the maximum aggregate packing fraction. A lower value of V_s/V_{sm} results in higher degree of aggregate migration and higher LL thickness leading to a lower value of η_{LL}. At V_s/V_{sm} approaching or exceeding 0.8 of the pumped concrete, the LL cannot form during pumping leading to a blockage in the pipeline [28, 45].

Choi et al. [28] reported that for concrete mixtures with low τ_{dy} (~ 10^1 - 10^2 Pa) and pumping parameters of $R_P = 62.5$ mm and $Q_P = 30$, 40, and 50 m^3/h, the amount of shearing in the bulk material can be neglected when η_{LL}/μ_p is lower than 30 (assuming the LL thickness to be 2 mm). This means during 3DP of print material with low values of η_{LL}/μ_p, the flow behavior during pumping can be considered as 'plug flow' even if the τ_B exceeds τ_{dy}. Also, an increase in yield stress and viscosity can be expected in such case owing to the high structural buildup of the print material compared to conventional concrete.

2.1.1.2. Material parameter - τ_{dy}/μ_p. The value of τ_{dy}/μ_p relates to the size of the plug zone and a higher value of τ_{dy}/μ_p means that more amount of bulk material moves along the pipeline un-sheared resulting in less structural breakdown. Based on the shearing data presented in [27], the amount of shearing in the bulk material is less significant for concrete with τ_{dy}/μ_p higher than 10 s^{-1}, when pumping along a pipeline with R_P of 62.5 mm at Q_P of 29 m^3/h. However, this number can vary with Q_P and R_P used. An un-sheared bulk material at low Q_P and high R_P can undergo shearing as Q_P is increased and R_P is reduced. Table 1 summarizes the pumping flow behavior of the print material as a function of key material and pumping parameters.

Table 1. Influence of key parameters on material flow behavior during pumping.

Pumping flow behavior	**Material parameters**				**Pumping parameters**	
	τ_{dy}^{*}	η_{LL}/μ_P	τ_{dy}/μ_P	$V_s/V_{sm}^{\dagger}$	Q_p	R_p
Plug flow	High	Low	High	Low	Low	High
Shearing flow: low shearing in bulk material	Low	Low	High	Low	Low	High
Shearing flow: high shearing in bulk material	Low	High	Low	Low	High	Low

*High and low value of τ_{dy} is in comparison to τ_B applied shear stress.

†Low V_s/V_{sm} refers to $V_s/V_{sm} << 0.8$.

2.2. EXTRUSION PROCESS

The extrusion of soft solids such as cement-based materials is done typically using a ram or screw-type extruder [22-24]. In ram extrusion, the material is filled in a barrel, and force is applied on the ram to push the material into a contraction (i.e., nozzle located at the end of the barrel), as shown in Figure 2a. In the case of screw extrusion, an Archimedes screw is used to covey the material towards the nozzle. The Archimedes screw allows for a continuous supply of the material to the extruder while the ram extruder requires a periodic filling of the barrel during extrusion. Despite this advantage of a screw-type extruder, the extrusion of cement-based materials is mainly done using a ram extruder, and the flow behavior of the cement-based materials through a screw-type extruder is not well researched. As a result, in the current paper, the discussion is limited to extrusion process of the print material using a ram extruder.

The ram extrusion process has some similarities to pumping process. In both processes, the pressure is applied on the cement-based material to move it along a barrel (during extrusion) or a pipeline (during pumping). This results in similar shear stress distribution in the extruder (in Figure 2a) and the pipeline (in Figure 1a). However, extrusion occurs over a considerably shorter distance compared to pumping. In other words, extruder length (L_E) in Figure 2a, is significantly smaller than the pipeline length (L_P) in Figure 1a. At such a short distance, the migration of aggregate towards the center and formation LL are insignificant. As a result, during extrusion, the shearing happens primarily in the bulk material, when the shear stress at the barrel wall (τ_{BW}) > τ_{dy}.

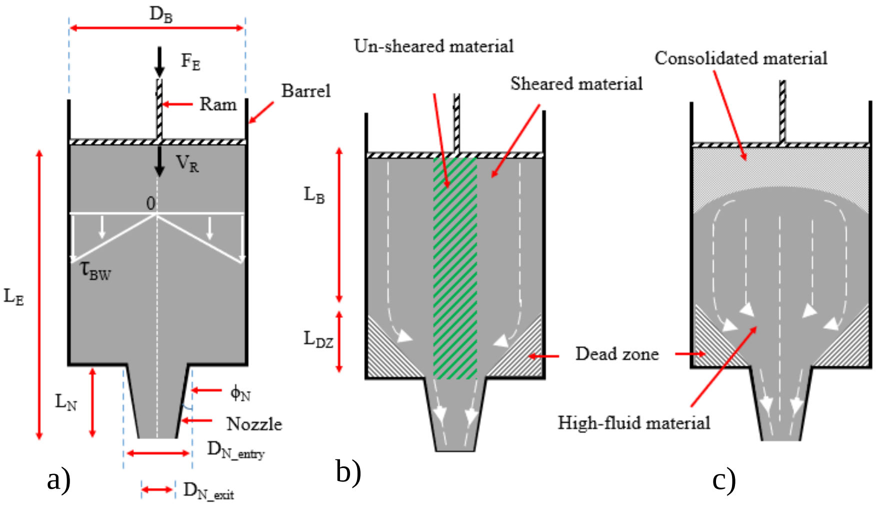

Figure 2. Ram extrusion process: a) ram extruder setup; b) homogenous extrusion behavior (plastic and visco-plastic flow); and c) heterogeneous extrusion behavior (frictional-plastic flow).

Despite the similarities in shear stress distribution in the pipeline (during pumping) and in the barrel (during extrusion), the change in the diameter (contraction) at the nozzle entry results in the formation of ‘dead-zone’ as shown in Figure 2b. The dead-zone shapes the cement-based materials and facilitates its flow into the nozzle. Within the nozzle, the material undergoes shearing along the nozzle wall before it extrudes out at the nozzle exit [49-51]. Typically, the nozzle length (L_N) is significantly smaller compared to L_E. For some extruder geometries, L_N=0, i.e., the nozzle is replaced with an orifice. As a result, the contribution of ‘shearing within the nozzle’ to the extrusion force (F_E) is often lower compared to the shearing within the barrel and at the nozzle entry [52]. However, in case of complex nozzle geometry, such as the tapered nozzle shown in Figure 2a, a significant contribution to F_E can come from the shearing of the print material in the nozzle [51]. In this paper, such complex nozzle geometries are not considered and shearing during extrusion is assumed to primarily occur at the barrel wall and the nozzle entry (i.e., at the dead zone). Based on the above information, the extent of shearing in print material is shown to be a critical parameter during extrusion, and it is a function of τ_{dy} and μ_P, as well as the extrusion parameters (i.e., barrel diameter (D_B), and extrusion speed (V_R)). At low shearing, only the material close to the barrel wall is sheared, while the remaining material moves along the extruder un-sheared (i.e., larger green region in Figure 2b). The extrusion flow behavior in such case is described as ‘plastic’ [50, 53, 54].

Alternatively, at high shearing, most of the material in the barrel undergoes shearing, and the extrusion flow behavior in such case is described as ‘visco-plastic’ [49, 54, 55]. The plastic behavior of the print material during extrusion stage of 3DP can result in structural buildup in the material, which can have a beneficial effect on the shape stability of the printed layers. Whereas for visco-plastic flow behavior, the shearing in the print material can result in structural breakdown leading to decrease in shape stability of the extruded layers.

During the plastic and visco-plastic flow, the print material stays homogenous in the barrel. However, the existence of a pressure gradient between the ram and nozzle entry and the confinement of the material within the barrel (between the ram and nozzle) can result in material heterogeneity. The pressure gradient causes fluid filtration and consolidation of the material located near the ram, as indicated in Figure 2c. The filtered fluid migrates towards the nozzle (low-pressure region) and results in dry and consolidated material near the ram, and a relatively high fluid material near the nozzle (material heterogeneity). The extruded material will contain higher amount of water leaving behind a relatively dry consolidated material in the barrel. The extrusion of this consolidated material would require a significant increase in F_E and may lead to blockage within the extruder [56-58]. This flow behavior is classified as 'frictional-plastic'. This phenomenon is also observed for print material with high concentration of aggregate (V_s approaching or exceeding $V_{cr} = 0.8V_{sm}$), where the application of F_E results in aggregate interlocking and fluid filtration through granular skeleton of the aggregate [46-48]. The frictional-plastic flow behavior can result in undesirable process-induced variations in material properties which can have a detrimental effect on shape stability of the printed element. Perrot et al. [56] reported up to a 50% drop in static yield stress (τ_{sy}) during extrusion of mortar with high V_s. Such decrease in τ_{sy} can result in poor shape stability of printed layers.

Based on the above information, the extrusion behavior of the print material and the process-induced variations in the material properties are shown to depend on the extent of shearing in the material, degree of fluid filtration and consolidation, and ratio of aggregate volume fraction to maximum packing fraction (V_s/V_{sm}). The key material and processing parameters that affect the extent of shearing, fluid filtration and consolidation, and V_s/V_{sm} are discussed below.

2.2.1. Extent of Shearing in Print Material. From Section 2.1.1, it is understood that the extent of shearing in the material is a function of the material rheology (i.e., τ_{dy}, μ_P, and η_{LL}) and processing parameters. During extrusion, the formation of the LL is insignificant (due to the small L_B), and the processing parameters of importance are D_B and V_R. Perrot et al. [54] used the Bingham number (B_N) to evaluate the extent of shearing and it considers the effect of material rheology (τ_{dy} and μ_P) and the extrusion parameters (D_B and V_R).

2.2.1.1. Bingham number (B_N). The parameter B_N is a function of τ_{dy}, μ_P, and the maximum shear rate acting on the material (γ'_{max}), as shown in Eq. 1. The value of γ'_{max} increases with increase of V_R and decrease in D_B and the apparent value of γ'_{max} can be estimated using Eq. 2.

At higher values of B_N (>100); i.e., high τ_{dy}/μ_p and low γ'_{max}, the contribution of material viscosity to the shearing is negligible and the print material flow behavior can be classified as 'plastic'[50, 53, 54]. Alternatively, at low values of B_N (≤ 100); i.e., low τ_{dy}/μ_p and high γ'_{max}, the viscosity contribution cannot be neglected, and more amount of the material within the extruder undergoes shearing, thus leading to a visco-plastic flow behavior [49, 54, 55].

$$B_N = \frac{\tau_{dy}}{\mu_p \dot{\gamma}_{max}} \qquad \text{Eq. 1}$$

$$\gamma'_{max} = \frac{8V_R}{D_B} \qquad \text{Eq. 2}$$

2.2.2. Degree of Fluid Filtration and Consolidation. Perrot et al. [54] introduced a drainage number (D_C) to measure the degree of fluid filtration and consolidation during the extrusion of cement-based materials. The D_C parameter takes into account the effect of print material properties (τ_{dy} and consolidation coefficient (C_V)), extrusion parameters (extrusion time (T_E) and L_E), as well as changes in the rheology of the material in the extruder as a result of filtration and consolidation.

2.2.2.1. Drainage number (D_c). The parameter D_C is measured using Eq. 3, and it is a function of C_V, T_E, L_E, and shear stress near the barrel wall at the start of the extrusion (τ_{BW0} at time zero). It is also a function of the evolution of τ_{BW} with decrease in the material porosity (e) as a result of material consolidation ($\left[\frac{d\tau_{BW}}{de}\right]_0$). Perrot et al. [54] observed that the material behaves as 'frictional-plastic' when values of D_c are larger than 25.

$$D_c = \left(\frac{C_v T_E}{{L_E}^2}\right)\left(\frac{1}{\tau_{BW0}}\left[\frac{d\tau_{BW}}{de}\right]_0\right) \qquad \text{Eq. 3}$$

In the first part of Eq. 3, $\left(\frac{C_V T_E}{{L_E}^2}\right)$, C_V represents the filtration and consolidation characteristics of the material. It takes into accounts the amount of fluid (paste) available for filtration as well as its rate of filtration. The term $\left(\frac{{L_E}^2}{C_V}\right)$ represents the characteristic filtration time. The term T_E is inversely related to V_R (i.e., high V_R results in low T_E) and is equal to L_E/V_R for extruder with an orifice opening instead of a nozzle, the latter is shown in Figure 2. The term $\left(\frac{C_v T_E}{{L_E}^2}\right)$ represents the ratio of T_E to the filtration time [54]. If the value of $\left(\frac{C_v T_E}{{L_E}^2}\right)$ is < 0.1, it means that T_E is smaller by at least one order of magnitude compared to $\left(\frac{{L_E}^2}{C_v}\right)$. In that case, no significant filtration and consolidation would occur in cement-based material during extrusion [54].

The second part of Eq. 3, $\left(\frac{1}{\tau_{BW0}}\left[\frac{d\tau_{BW}}{de}\right]_0\right)$, represents the changes in material rheology as a result of filtration and consolidation; i.e., ($d\tau_{dy}/de$). The parameter τ_{BW0} is a function of τ_{dy} and internal frictional angle of material (ϕ). The term $\left[\frac{d\tau_{BW}}{de}\right]_0$ is a function of τ_{dy}, ϕ, radial stress acting on the material near the ram, and the decrease in 'e' with the consolidation of the material [57]. The term $\left[\frac{d\tau_{BW}}{de}\right]_0$ is only significant at high values of $\left(\frac{C_v T_E}{{L_E}^2}\right)$.

2.2.3. Ratio of Aggregate Volume Fraction to Maximum Packing Fraction (V_s/V_{sm}).

The frictional-plastic flow behavior is expected for the print material with approaching or exceeding 0.8. However, at low values of V_s (i.e., V_s/V_{sm} <<0.8), the extrusion flow behavior of the print material can be plastic, visco-plastic, or frictional-plastic depending on the values of B_N and D_c, as mentioned in Sections 2.2.2. and 2.2.3. Table 2 summarizes the extrusion flow behavior of the print material as a function of key material and extrusion parameters.

Table 2. Influence of key parameters on material flow behavior during extrusion.

Extrusion flow behavior	**Material parameters**				**Extrusion parameters**†		
	$\boldsymbol{\tau_{dy}/\mu_P}$	$\mathbf{V_s/V_{sm}}^{*}$	$\mathbf{C_V}$	$\mathbf{d\tau_{dy}/de}$	$\mathbf{V_R}$	$\mathbf{D_B}$	$\mathbf{L_E}$
Plastic	High	Low	Low		Low	High	
Visco-plastic	Low	Low	Low		High	Low	
Frictional-plastic		Low	High	High	Low		Low
		High					

$^{\dagger *}$Low V_s/V_{sm} refers to $V_s/V_{sm} << 0.8$.
† $T_E = L_E/V_R$ for extruder with an orifice instead of a nozzle.

From Table 1 and Table 2, the common material parameters that influence the flow behavior during pumping and extrusion consist of the print material rheological parameters (τ_{dy} and μ_p) and V_s/V_{sm}. The amount of paste available for filtration is also a common parameter as it controls η_{LL}/μ_p during pumping, as indicated in Table 1, and C_V during extrusion, as indicated in Table 2.

During 3DP, high value of τ_{dy}/μ_p can result in less shearing and less structural breakdown in the print material. High values of V_s/V_{sm} that are approaching or exceeding 0.8 can lead to blockage in the pipeline and the extruder. This results in significant drop in the quality of the extruded material leading to poor shape stability.

However, the effect of filtration is opposite on the extrusion and pumping processes. During pumping, higher amount of paste available for filtration can translate into an easier formation of LL resulting in low η_{LL} and lower extent of shearing in the bulk material. Whereas, during extrusion, higher paste filtration can lead to frictional-plastic flow behavior (especially at low V_R), hence resulting in material heterogeneity and poor quality of the extruded material. Therefore, during the selection of cement-based materials for 3DP, the amount of paste available for filtration should be optimized to ensure pumping and extrusion of the print material without blockage and to minimize process-induced variations in material properties.

3. PRINT MATERIAL FLOW BEHAVIOR DURING 3DP

The successful pumping and extrusion of a cement-based material requires selection of material and processing parameters that facilitate formation of LL during pumping, while minimizing the possibility of filtration and consolidation during extrusion. However, in 3DP literature the print material formulation and selection of processing parameters are mainly based on shape stability requirements with limited emphasis on pumping and extrusion flow behavior and its influence on shape stability.

This section offers a comprehensive review of 3DP literature regarding the print materials and processing parameters used for printing shape-stable elements. Attempt is made to relate the available knowledge of cement-based materials flow behavior during pumping and extrusion to the properties of the print material and processing parameters that govern the shape stability of the 3D printed elements.

3.1. PRINT MATERIAL COMPOSITION AND PROCESSING PARAMETERS

From Table 1 and Table 2, the flow behavior and process-induced variations in material properties are shown to be dependent on the material parameters (τ_{dy}, μ_P, η_{LL}, V_s/V_{sm}, and C_V) and processing parameters (Q_p, R_p, V_R, D_B, and L_E). However, the values of η_{LL} and C_V of the print materials are not available in 3DP literature. The lack of information on η_{LL} is due to the limitation of the test methods available for measuring LL properties. The LL assessment methods available for pumped concrete are not suitable for the assessment of LL properties of print materials owing to their high τ_{dy} [21]. Whereas the absence of information on C_V is due to the lack of emphasis on the filtration and consolidation characteristics of the print material in 3DP literature. In this section, the print material parameters and composition as well as processing parameters used in the 3DP literature are presented. An estimation of η_{LL} and C_V based on the composition and processing parameters is attempted in Sections 3.2 and 3.3.

3.1.1. Print Material Composition and Parameters.

The information on print material composition and key material parameters are shown in Table 3. As indicated in this table, print materials often include a supplementary cementitious material (SCM) such as fly ash (FA) [7, 59] and silica fume (SF) [60] or fillers such as limestone powder [51] as partial replacement of portland cement (PC) [61-65]. From a rheological point of view, the use of SCMs and fillers can enhance particle packing density [7, 19] and reduce μ_P [14, 66]. Rapid-setting cements such as calcium sulphoaluminate cement (CSA) is used to increase the rate of structural buildup of the print material thereby improving shape stability [61-65]. Table 3 also indicates that the water-to-binder ratio (w/b) of the print materials is kept low to improve shape stability [67] and mechanical performance of the printed elements [68].

As indicated in Table 3, different types of chemical admixtures, such as superplasticizers, retarders, and rheology-modifying admixtures are used in print materials. Superplasticizers are incorporated to ensure dispersion of the binder thereby enhancing the particle packing density and producing low w/b to improve mechanical properties and durability [69-71]. Set-controlling admixtures such as retarders are used to delay the hydration kinetics of the cement-based materials to extend the time window during which the material can be printed [72-75]. Rheology-modifying admixtures such as viscosity-modifying and thixotropy-enhancing admixtures (including nanomaterials) are used to improve the shape stability of the extruded material [76-79] and increase the resistance to drying [80].

Relatively smaller aggregates (lower maximum aggregate size (MAS)) are used for print materials. This is done to prevent blockage at the nozzle entry during extrusion [81-84]. El Cheikh et al. [85] reported that nozzle diameter (D_N) to MSA ratio ($B_E = D_N$ /MSA) needs to be larger than 4.25 to prevent blockage during extrusion [85]. For the print materials, the B_E values are calculated using the MSA values and assuming D_N to be equal to the smaller dimension of the nozzle for non-circular nozzles. These calculated B_E values range between 4.5 and 50 that meet the criterion proposed by El Cheikh et al. [85]. The particle size distribution and volume fraction of the aggregate were selected primarily to optimize particle packing density of aggregate [66] or total solid particles (i.e., aggregate + binder) [7, 19].

3.1.2. Processing Parameters. Published values of processing parameters are shown in Table 3. The optimization of the processing parameters is needed for minimizing the changes in material properties as well as maintaining a steady and continuous supply of the material to the printhead. Such optimization ensures a uniform cross-section of the printed layers [19]. A steady and continuous supply of the print material to the printhead requires balancing of Q_P and V_R (increase of Q_P increases V_R at fixed D_B). Additionally, the printhead speed (V_{Ph}) i.e., the moving speed of the printhead in the print direction needs to be balanced with V_R [19]. The increase of V_{Ph} necessitates an increase of V_R to maintain a uniform cross-section of the printed layers. The information on all the processing parameters used is necessary for accurate prediction of print material flow behavior and estimation of process-induced variations in material properties during pumping and extrusion stages of 3DP. However, the 3DP literature provides limited information on processing parameters pertaining to nozzle size and V_{Ph} and values of other key processing parameter (Q_P, R_P, L_E, D_B, and V_R) are not available.

3.2. PRINT MATERIAL FLOW BEHAVIOR DURING PUMPING

From Section 2.1, the print material can exhibit plug or shearing flow behavior during pumping depending on the extent of shearing in the bulk material. The extent of such shearing is a function of material parameters (η_{LL}/μ_p and τ_{dy}/μ_p) as well as processing parameters (R_P and Q_P). However, no information is available on R_P and Q_P values in 3DP literature. As a result, the print material flow behavior during pumping is estimated based on the material parameters.

3.2.1. Estimation of Extent of Shearing in Bulk Material.

3.2.1.1. Material parameter- η_{LL}/μ_p. The lower value of η_{LL}/μ_p results in easier formation of LL and it decreases with decrease in A_{fines} and decrease in V_s/V_{sm}.

Total surface area of dry powders (A_{fines})

Assuming complete dispersion of the binder particles in the print material, the value of A_{fines} can be estimated by multiplying the mass of each binder component (M_{bi}) in the print material with the corresponding Blaine fineness value (BF_{bi}) [39], as shown in Eq. 4.

$$\mathrm{A_{fines}} = \frac{\sum \mathrm{M_{bi}BF_{bi}}}{\text{Volume of print material } (1\ \mathrm{m}^3)} \qquad \text{Eq. 4}$$

The estimated values of A_{fines} for the print materials in Table 3 range between 3×10^9 to 5×10^9 cm^2/m^3. For conventional concrete, Secrieru et al. [39] reported formations of thick LL for concrete with A_{fines} ranging between 1×10^9 to 2×10^9 cm^2/m^3. The high values of A_{fines} for print materials compared to the conventional concrete indicate either low chance of LL formation or formation of relatively thin LL during pumping.

Ratio of aggregate volume fraction to maximum packing fraction (V_s/V_{sm})

The V_s values of the print materials in Table 3 vary from 16% to 60%. However, the V_{sm} values of aggregate are not provided in referenced papers. As suggested by [46, 91, 92], the value of V_{sm} can be estimated using the semi-empirical relation proposed by Hu and de Larrard [93], shown in Eq. 5.

$$\mathrm{V_{sm}} = 1 - 0.45\left(\frac{\mathrm{d_{min}}}{\mathrm{MSA}}\right)^{0.19} \qquad \text{Eq. 5}$$

where d_{min} is the minimum size of the aggregate.

The minimum size of aggregate is considered to be 0.05 mm, and the values of V_{sm} and V_s/V_{sm} are estimated accordingly. The V_s/V_{sm} values of the print materials can then range between 0.21 and 0.81.

For print materials with $V_s/V_{sm} << 0.8$, shear-induced aggregate migration is possible, indicating the possibility of LL formation. Whereas for print materials with high V_s/V_{sm}, LL cannot form and so these mixtures are not suitable for large-scale 3DP applications where pumping is needed.

Table 3. Information on print materials' composition, key material and processing parameters.

Ref	Material composition*					Material parameters			3DP parameters		Estimated parameters		
	Binder (by mass)	**Admixture**	**MSA (mm)**	**V_s (%)**	**w/b**	**τ_{dy} (kPa)**	**μ_P (Pa.s)**	**τ_{dy}/μ_P (s^{-1})**	**N. size (mm)**	**V_{Ph} (mm/s)**	**B_E**	**$A_{fines}.10^9$ (cm^2/m^3)**	**V_s/V_{sm}**
[86]	100% PC	S+T	1	36	0.35	0.2	3.8	47.4	20	133	20.0	3.8	0.81
[87]	100% PC		0.3	45	0.38				15x25	12	50.0	3.1	0.66
[62]	93% PC 7% CSA	S	2.0	42	0.35				10		5.0	3.4	0.54
[16]	90% PC 10% SF	S+T	4.8	53	0.43				25x38	60	5.3	3.1	0.65
[82]	41% PC 39% FA 20% SF	S	1.0	47	0.40	3.0-3.6	110-190	16.1-32.0	10x20; 8	150	8.0	3.5	0.63
[7]	70% PC 20% FA 10% SF	S+R	2.0	60	0.26				9		4.5	3.0	0.77
[19]	70% PC 20% FA 10% SF	S	1.0	43	0.27				8x25	450	8.0	4.2	0.58
[66]	48% PC 47% FA 5% SF	S	1.2	16	0.30	0.2-0.5	17-33	12.5-37.1	20	95	16.7	5.0	0.21
[88]	70% PC 20% FA 10% SF	S+T S+V	1.0	47	0.32				20x30	44	20.0	3.6	0.63

Table 3. Information on print materials' composition, key material and processing parameters (cont.).

[89]	40% PC 57% FA 3% CSA	S+T	0.3	19	0.28	0.2	3.6	63.6	20	100	66.7	4.4	0.28
[14]	37% PC 56% FA 7% SF	S	2.5	22	0.26	0.2			15x15	100	6.0	5.0	0.28
[90]	70% PC 20% FA 10% SF	S	4.8	44	0.32	1.2			25	60	5.3	3.8	0.54

[*] Blaine fineness values for PC, SF, CSA, and FA are assumed as 400, 1100, 450, and 300 m^2/kg respectively.

Chemical admixtures S, R, T and V refer to superplasticizers, retarders, thixotropy-enhancing and viscosity-modifying admixtures, respectively.

3.2.1.2. Material parameter- τ_{dy}/μ_p. The τ_{dy}/μ_p values of the print materials in Table 3 range from 12 to 64 s^{-1}. For convention concrete, Feys [27] observed less shearing in the bulk material for concretes with τ_{dy}/μ_p >10 s^{-1} at Q_P and R_P values of 29 m^3/h and 62.5 mm, respectively. The high values of τ_{dy}/μ_p for print material compared to conventional concrete in [27] suggest low possibility of shearing for the print material during pumping.

3.2.2. Estimation of Print Material Flow Behavior. Based on estimated values of A_{fines} and V_s/V_{sm}, a thin layer of LL is anticipated to form for the print materials during pumping (i.e., high value of η_{LL}/μ_p). Based on Table 1, the high value of η_{LL}/μ_p combined with a high value of τ_{dy}/μ_p may result in shearing flow behavior during pumping. However, the extent of shearing in the bulk material cannot be estimated at this stage due to the lack of information on the processing parameters, R_P and Q_P. Additionally, the print materials in Table 3 with V_s/V_{sm} approaching or exceeding 0.8, may be considered suitable for printing shape-stable layers at lab-scale. However, for large-scale 3DP that requires pumping, use of such materials is not recommended as they may cause blockage in the pipeline. The expected flow behaviors for the print material with different key during pumping stage of 3DP is summarized in Table 4.

3.3. PRINT MATERIAL FLOW BEHAVIOR DURING EXTRUSION

As shown in Section 2.2, the print material can exhibit plastic, visco-plastic, or frictional-plastic flow behavior during extrusion. This depends on the extent of shearing in the material, which can be estimated using B_N, degree of fluid filtration and consolidation, which can be estimated using D_C, and V_s/V_{sm}.

Table 4. Expected flow behavior during pumping stage of 3DP.

Material parameter	**Value for print material**	**Expected flow behavior**
η_{LL}/μ_P	High*	Shearing flow - Low shearing at high R_P and low Q_P - High shearing at low R_P and high Q_P
τ_{dy}/μ_P	High*	
V_s/V_{sm}	<< 0.8	
	close to or > 0.8 (undesirable)	Not suitable for pumping

*In comparison to conventional concrete.

3.3.1. Estimation of Extent of Shearing in Print Material (B_N). For computing the values of B_N (using Eq. 1), the information about the ranges of τ_{dy}, μ_p, and γ'_{max} is needed. Typical values of τ_{dy} and μ_p used for 3DP are reported in Table 3. The apparent values of γ'_{max} can be calculated using Eq. 2. However, B_N cannot be estimated because limited information is available on the values of V_R and D_B needed for the estimation of γ'_{max}. Based on the comparison presented in Section 3.2 for the values of τ_{dy}/μ_p that can be obtained for print material and conventional concrete, a lower extent of shearing is expected for the print material during extrusion. This means for a given extruder with a given D_B, high V_R is needed for significant shearing of the print material and visco-plastic flow behavior during extrusion.

3.3.2. Estimation of Degree of Fluid Filtration and Consolidation (D_c). The estimation of D_c using Eq. 3 requires information on the material parameters (i.e., C_v, τ_{BW} and $\left[\frac{d\tau_{BW}}{de}\right]_0$) and processing parameters (i.e., L_E and T_E). However, there is limited information available on such parameters in the 3DP literature. As indicated in Section 2.2.2, the first term in Eq. 3 $\left(\frac{C_v T_E}{{L_E}^2}\right)$ determines the extent of filtration and consolidation during the extrusion process, while the second term $\left(\frac{1}{\tau_{BW0}}\left[\frac{d\tau_{BW}}{de}\right]_0\right)$ represents the changes in material rheology. The second term is only significant when $\left(\frac{C_v T_E}{{L_E}^2}\right)$ is high, and the C_v is a function of the amount of paste available for filtration and the filtration rate.

3.3.2.1. Coefficient of consolidation (C_v). The amount of paste available for filtration was assessed in Section 3.2 using the parameter A_{fines}. The estimated A_{fines} values for the print material ranged from $3x10^9$ to $5x10^9$ cm^2/m^3 and were identified to be significantly higher than those of conventional concrete. This means less amount of paste is available for filtration in print material. Additionally, as noted in Section 3.1, the print material constituents are often selected to optimize the particle packing density, hence indicating low permeability (low rate of filtration) compared to conventional concrete. Based on the above information, the C_v is expected to be lower for print material compared to conventional concrete. Consequently, for fixed extrusion parameters (fixed T_E and L_E), the values of $\left(\frac{C_v T_E}{{L_E}^2}\right)$ is expected to be lower for the print material compared to conventional concrete. This also means that the second term of Eq. 3 $\left(\frac{1}{\tau_{BW0}}\left[\frac{d\tau_{BW}}{de}\right]_0\right)$ is less significant for the print material compared to conventional concrete.

3.3.3. Estimation of Ratio of Aggregate Volume Fraction To Maximum Packing Fraction (V_s/V_{sm}). As established in Section 3.2, for print materials with $V_s/V_{sm} << 0.8$, the material can behave like plastic, visco-plastic, or frictional-plastic depending on B_N and D_C. However, neither of these parameters can be determined at this stage due to the lack of information available in the 3DP literature pertaining to the extrusion process parameters and print material characteristics. For print materials with V_s/V_{sm} approaching or exceeding 0.8, despite the lack of information for estimation of B_N

and D_C, the material flow behavior during extrusion can be expected to be frictional-plastic. In such case, the print material no longer stays homogenous within the extruder, and the extruded material can have low τ_{sy} leading to poor shape stability of the printed elements.

3.3.4. Estimation of Print Material Flow Behavior. The flow behavior for the print material cannot be predicted accurately at this stage due to limited information on extrusion parameters (L_E, D_B, and V_R) and material properties (such as C_v and $d\tau_{dy}/de$). For print material with $V_s/V_{sm} << 0.8$, the expected low value of C_v, and consequently low value of D_c, means that the print material will most likely behave as visco-plastic during extrusion at high V_R/D_B. At low V_R/D_B, plastic flow behavior is expected; however, an assessment of D_c is needed for more accurate prediction. If the D_c is significant, the successful extrusion requires increasing V_R to reduce T_E, thereby reducing $\left(\frac{C_v T_E}{{L_E}^2}\right)$ and D_c. For cement-based materials with V_s/V_{sm} approaching or exceeding 0.8, the material flow behavior is frictional-plastic at any V_R that can lead to poor shape stability. Print materials with high V_s, are not suitable for 3DP especially at large-scale where pumping is needed. The expected flow behavior for the print material with different key parameters during the extrusion stage of 3DP is summarized in Table 5.

4. SHAPE STABILITY – MATERIAL FLOW BEHAVIOR AND PROCESS-INDUCED VARIATION

Based on the theoretical and analytical analysis presented by Wangler et al. [94], Roussel [26], and Suiker [25], the shape stability of the printed elements is a function of τ_{sy} and elastic modulus (E) of the extruded material and their variations with time, printing speed, and geometry and dimensions of individual layers and the printed element. The variation of τ_{sy} and E with time refers to the rate of structural buildup in the material. The rheological properties τ_{sy} and E are function of the particle size distribution, chemical reactivity, and relative proportions of the material constituents [95, 96], as well as the flow history of the material [36, 37]. The flow history of the extruded material includes the extent of shearing in the bulk material during pumping, the extent of shearing and the degree of filtration and consolidation during extrusion.

Table 5. Expected flow behavior during extrusion stage of 3DP.

Material parameter	**Value for print material**	**Expected flow behavior**
τ_{dy}/μ_P	High[*]	- Plastic at low V_R/D_B and high L_E^2/T_E[†] - Frictional-plastic at low V_R/D_B and L_E^2/T_E - Visco-plastic at high V_R/D_B
C_V	Low[*]	
V_s/V_{sm}	<< 0.8	
	close to or > 0.8 (undesirable)	Frictional-plastic

[*] In comparison to conventional concrete.

[†] $T_E = L_E/V_R$ for extruder with an orifice instead of a nozzle. In this case, $L_E^2/T_E = V_R L_E$.

As indicated in Section 3.2, the print material is expected to undergo shearing in the LL and bulk material during pumping. The shearing of the bulk material in the pipeline can cause structural breakdown as well as increase in material temperature and changes in air content [27]. The structural breakdown decreases the values of τ_{dy}, μ_p, τ_{sy}, and E [36, 37], while the increase in temperature results in decrease of μ_p and increase of τ_{dy}, τ_{sy}, and E [44, 97]. Additionally, the incorporation of air during pumping can result in a decrease of μ_p and a drop in fluid filtration [58]. These changes in τ_{dy}, μ_p, and fluid filtration during pumping means that the print material that reaches the printhead can have different values of B_N and D_c and consequently different flow behavior during extrusion compared to the freshly-mixed print material.

As indicated in Table 5, during extrusion, the print material can behave as plastic, visco-plastic, frictional-plastic. The print material can undergo further shearing and phase separation (due to filtration and consolidation) in the extruder. This can lead to higher water content and lower τ_{sy} and E in the extruded material compared to the freshly-mixed print material. The increase in water content causes a reduction in the rate of structural buildup (i.e., low rate of increase in τ_{sy} and E with time) [95]. Such drop in τ_{sy} and E and rate of structural buildup during pumping and extrusion can hinder the shape stability of the printed element if the printing speed and the thickness of the printed layers are not reduced accordingly [26, 94].

The printing speed is a function of V_{Ph} and time gap between printing of successive layers, while the thickness of the printed layers is a function of nozzle size and the distance between the nozzle opening and surface of the existing layer. As noted in Section 3.1, any adjustments to V_{Ph} requires balancing of Q_P and V_R, to ensure a continuous supply of the print material to the printhead and to maintain uniform cross-section of the printed layers. However, changing the processing parameters (Q_P and V_R) can alter the extent of shearing during pumping and extrusion and the degree of filtration during extrusion, which consequently affects the τ_{sy} and E values of the extruded material. Accurate assessment of this interdependency between the material and processing parameters is key for determining the optimum processing parameters that could lead to printing of shape-stable elements while reducing the printing time. The expected flow behavior for print material during 3DP and its anticipated influence on shape stability is summarized in Table 6.

The influence of process-induced variations during 3DP on shape stability of the printed elements is highlighted in Figure 3. This flow chart illustrates the influence of the selected processing parameters on the shape stability of the 3D printed elements. The strategies that can be implemented to reduce the negative impact of the pumping and extrusion on shape stability are also recommended.

5. FUTURE WORK

The successful 3DP of cement-based materials requires the selection of print materials and processing parameters that can facilitate the formation of LL during pumping, while minimizing the structural breakdown and phase separation during pumping and extrusion. Providing some guidelines for the selection of print materials and processing parameters necessitates developing more information in the following aspects:

- Develop suitable test methods to assess the properties of the LL of print materials. The interface rheometers available for assessment of LL typically do not measure LL properties for cement-based materials with high yield stress which are used for 3DP.
- Evaluate the influence of complex nozzle geometries on the extent of shearing and its effect on shape stability of 3D printed elements. This is important since material can undergo shearing in the nozzle and such shearing can have a significant influence on the shape stability of printed elements.

- The present understanding of the material flow behavior in the screw-type extruders is rather limited, and more work is needed to adapt the screw-type extruders for large-scale 3DP.

Table 6. Influence of print material flow behavior on shape stability.

Expected flow behavior	**Effect on shape stability**[*]	**Required processing parameters**
Pumping		
Shearing flow – Less shearing in bulk material	+	High R_P and low Q_P
Shearing flow – Higher shearing in bulk material	-	Q_P needs to be decreased to reduce extent of shearing. This decreases V_R/D_B and L_E^2/ T_E[†], and can change extrusion flow behavior.
Extrusion		
Plastic	+	Low V_R/D_B and high L_E^2/ T_E
Visco-plastic	-	Lowering V_R to reduce extent of shearing can lower L_E^2/ T_E. It can change flow behavior to frictional-plastic.
Frictional-plastic	- -	V_R needs to be increased to ensure high L_E^2/ T_E. It can change flow behavior to visco-plastic.

[*] + indicates improvement in shape stability.
- indicates drop in shape stability.
- - indicates significant drop in shape stability.
[†] $T_E = L_E/V_R$ for extruder with an orifice instead of a nozzle. In this case, $L_E^2/ T_E = V_R L_E$.

- Develop systems to evaluate inline changes of key properties that affect flow behavior of the print material and shape stability of the printed element. This includes fluid filtration during pumping and extrusion, and the increase of τ_{sy}, E, and rate of structural buildup in the extruded material. Such process-induced variations need to be considered during the print material formulation to avoid loss of shape stability during 3DP.
- Numerical and analytical models that take into account the effect of processing parameters, material properties at the start of printing, as well as the process-induced changes, need to be developed to ensure a steady and continuous flow of

the materials during pumping and extrusion, and to prevent failure of the printed elements.

6. SUMMARY

The successful implementation of 3DP for concrete construction requires knowledge of material flow behavior during processing stages of 3DP. In this paper, a comprehensive review of the processing stages of 3DP, pumping and extrusion, is carried out. The print material flow behavior during pumping and extrusion stages of 3DP and key material and processing parameters that govern the flow behavior are identified. Additionally, the influence of the flow behavior and process-induced variations in material properties on the shape stability is highlighted. Future work needed for better prediction of material flow behavior during 3DP and influence of process-induced variations on shape stability of the printed elements is recommended. The main findings from the analysis carried out in this paper are summarized here.

1. The flow behavior of cement-based materials during pumping for 3DP depends on the material properties (μ_P, τ_{dy}, η_{LL}, and V_s/V_{sm}) as well as processing parameters pertaining to pumping (R_P and Q_P).
2. The assessment of η_{LL} and values of R_P and Q_P are needed for estimation of the extent of shearing within the bulk material. High V_s can be unsuitable for 3DP where pumping is required.
3. Limited information is available on the η_{LL} of print materials. However, given the print material composition for 3DP, η_{LL} of print materials can be high compared

to conventional concrete. The flow behavior of the print material during pumping is expected to involve the 'shearing of LL and bulk material' provided that V_s is significantly lower than $0.8V_{sm}$.

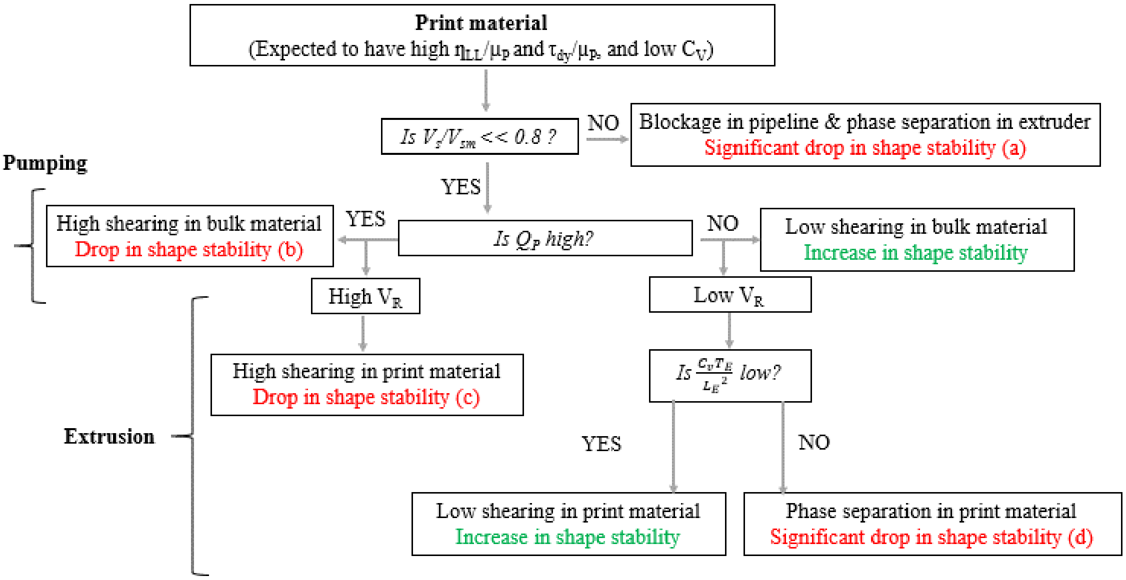

Strategies to improve shape stability:

a) Particle packing density of aggregate needs to be increased to reduce extent of shearing (at fixed V_R).
b) L_E particle packing density of aggregate needs to be adjusted to increase V_{sm} (at fixed V_s).
c) R_P needs to be increased to reduce extent of shearing (at fixed Q_P).
d) D_B needs to be increased to reduce extent of phase separation (at fixed V_R).

Figure 3. Process-induced variations during 3DP and its effect on shape stability. 3DP process can result in an increase (shown in green) or drop (shown in red) in shape stability.

4. The flow behavior of cement-based material during extrusion change with B_N and D_C. These parameters are dependent on material properties (μ_P, τ_{dy}, V_s/V_{sm}, C_v, and $d\tau_{dy}/de$) and processing parameters pertaining to extrusion (D_B, L_E, and V_R).

5. Print materials typically have low C_v and $d\tau_{dy}/de$ values compared to conventional concrete. The flow behavior of the print material during extrusion is expected to be 'plastic' at low V_R/D_B, and 'visco-plastic' at high V_R/D_B, provided the V_s is

significantly lower than $0.8V_{sm}$. Cement-based materials with high V_s are unsuitable for extrusion-based 3DP. Proper assessment of C_v and $d\tau_{dy}/de$ and accurate values of D_B, L_E, and V_R are necessary to predict flow behavior of the print material during extrusion.

6. The shearing of the print material during pumping can change material properties (τ_{dy}, μ_p, τ_{sy}, E, and fluid filtration), which can influence the flow behavior during extrusion. The shearing, filtration and consolidation during extrusion can further alter τ_{sy}, E, and the rate of structural buildup of the print material.
7. The reduction of τ_{sy}, E, and the rate of structural buildup during pumping and extrusion of 3DP can result in poor shape stability of the printed elements. Ensuring proper shape stability requires accurate assessment of process-induced variations in the material properties and adjusting the processing parameters, such as V_{Ph}, Q_P, and V_R, based on the anticipated changes in material properties.

REFERENCES

[1] N. Hack, W.V. Lauer, Mesh-mould: Robotically fabricated spatial meshes as reinforced concrete formwork, Architectural Design 84(3) (2014) 44-53.

[2] J. Zhang, J. Wang, S. Dong, X. Yu, B. Han, A review of the current progress and application of 3D printed concrete, Composites Part A: Applied Science and Manufacturing 125 (2019) 105533.

[3] R.A. Buswell, W.R.L. da Silva, F.P. Bos, H.R. Schipper, D. Lowke, N. Hack, H. Kloft, V. Mechtcherine, T. Wangler, N. Roussel, A process classification framework for defining and describing digital fabrication with concrete, Cement and Concrete Research 134 (2020) 106068.

[4] A. Bhardwaj, S.Z. Jones, N. Kalantar, Z. Pei, J. Vickers, T. Wangler, P. Zavattieri, N. Zou, Additive manufacturing processes for infrastructure construction: A review, International Manufacturing Science and Engineering Conference, American Society of Mechanical Engineers, 2019, p. V001T01A005.

[5] B. Khoshnevis, Automated construction by contour crafting—related robotics and information technologies, Automation in Construction 13(1) (2004) 5-19.

[6] B. Khoshnevis, D. Hwang, K.-T. Yao, Z. Yeh, Mega-scale fabrication by contour crafting, International Journal of Industrial and Systems Engineering 1(3) (2006) 301-320.

[7] T.T. Le, S.A. Austin, S. Lim, R.A. Buswell, A.G. Gibb, T. Thorpe, Mix design and fresh properties for high-performance printing concrete, Materials and Structures 45(8) (2012) 1221-1232.

[8] G.J. Gibbons, R. Williams, P. Purnell, E. Farahi, 3D printing of cement composites, Advances in Applied Ceramics 109(5) (2010) 287-290.

[9] M. Xia, J. Sanjayan, Method of formulating geopolymer for 3D printing for construction applications, Materials & Design 110 (2016) 382-390.

[10] B. Utela, D. Storti, R. Anderson, M. Ganter, A review of process development steps for new material systems in three dimensional printing (3dp), Journal of Manufacturing Processes 10(2) (2008) 96-104.

[11] T.A. Salet, Z.Y. Ahmed, F.P. Bos, H.L. Laagland, Design of a 3D printed concrete bridge by testing, Virtual and Physical Prototyping (2018) 1-15.

[12] Yingchuang building technique co.Ltd. (winsun). http://www.winsun3d.com/En/. (Accessed January 17 2019).

[13] Apis cor. www.apis-cor.com/en. (Accessed January 17 2019).

[14] Z. Liu, M. Li, Y. Weng, T.N. Wong, M.J. Tan, Mixture design approach to optimize the rheological properties of the material used in 3D cementitious material printing, Construction and Building Materials 198 (2019) 245-255.

[15] Y.W.D. Tay, Y. Qian, M.J. Tan, Printability region for 3D concrete printing using slump and slump flow test, Composites Part B: Engineering 174 (2019) 106968.

[16] A. Kazemian, X. Yuan, E. Cochran, B. Khoshnevis, Cementitious materials for construction-scale 3D printing: Laboratory testing of fresh printing mixture, Construction and Building Materials 145 (2017) 639-647.

[17] G. Ma, Z. Li, L. Wang, F. Wang, J. Sanjayan, Mechanical anisotropy of aligned fiber reinforced composite for extrusion-based 3D printing, Construction and Building Materials 202 (2019) 770-783.

[18] B. Panda, S.C. Paul, L.J. Hui, Y.W.D. Tay, M.J. Tan, Additive manufacturing of geopolymer for sustainable built environment, Journal of Cleaner Production 167 (2017) 281-288.

[19] G. Ma, Z. Li, L. Wang, Printable properties of cementitious material containing copper tailings for extrusion based 3D printing, Construction and Building Materials 162 (2018) 613-627.

[20] A.S.J. Suiker, R.J.M. Wolfs, S.M. Lucas, T.A.M. Salet, Elastic buckling and plastic collapse during 3D concrete printing, Cement and Concrete Research 135 (2020) 106016.

[21] V. Mechtcherine, F.P. Bos, A. Perrot, W.L. da Silva, V. Nerella, S. Fataei, R.J. Wolfs, M. Sonebi, N. Roussel, Extrusion-based additive manufacturing with cement-based materials–production steps, processes, and their underlying physics: A review, Cement and Concrete Research 132 (2020) 106037.

[22] V. Nerella, M. Näther, A. Iqbal, M. Butler, V. Mechtcherine, Inline quantification of extrudability of cementitious materials for digital construction, Cement and Concrete Composites 95 (2019) 260-270.

[23] A. Perrot, D. Rangeard, V.N. Nerella, V. Mechtcherine, Extrusion of cement-based materials-an overview, RILEM Technical Letters 3 (2018) 91-97.

[24] I. Aydin, F.R. Biglari, B.J. Briscoe, C.J. Lawrence, M.J. Adams, Physical and numerical modelling of ram extrusion of paste materials: Conical die entry case, Computational Materials Science 18(2) (2000) 141-155.

[25] A.S.J. Suiker, Mechanical performance of wall structures in 3D printing processes: Theory, design tools and experiments, International Journal of Mechanical Sciences 137 (2018) 145-170.

[26] N. Roussel, Rheological requirements for printable concretes, Cement and Concrete Research (2018).

[27] D. Feys, How much is bulk concrete sheared during pumping?, Construction and Building Materials 223 (2019) 341-351.

[28] M. Choi, N. Roussel, Y. Kim, J. Kim, Lubrication layer properties during concrete pumping, Cement and Concrete Research 45 (2013) 69-78.

[29] G. De Schutter, D. Feys, Pumping of fresh concrete: Insights and challenges, RILEM Technical Letters 1 (2016) 76-80.

[30] M. Choi, K. Park, T. Oh, Viscoelastic properties of fresh cement paste to study the flow behavior, International Journal of Concrete Structures and Materials 10(3) (2016) 65-74.

[31] D. Feys, K.H. Khayat, R. Khatib, How do concrete rheology, tribology, flow rate and pipe radius influence pumping pressure?, Cement and Concrete Composites 66 (2016) 38-46.

[32] D. Feys, K.H. Khayat, A. Perez-Schell, R. Khatib, Prediction of pumping pressure by means of new tribometer for highly-workable concrete, Cement and Concrete Composites 57 (2015) 102-115.

[33] D. Kaplan, L. François de, T. Sedran, Avoidance of blockages in concrete pumping process, ACI Materials Journal 102(3) (2005) 183.

[34] D.B. Roger, B.B. Phillip, Tests to establish concrete pumpability, ACI Journal Proceedings 74(5).

[35] D. Feys, G. De Schutter, K.H. Khayat, R. Verhoeven, Changes in rheology of self-consolidating concrete induced by pumping, Materials and Structures 49(11) (2016) 4657-4677.

[36] N. Roussel, A thixotropy model for fresh fluid concretes: Theory, validation and applications, Cement and Concrete Research 36(10) (2006) 1797-1806.

[37] J.E. Wallevik, Rheological properties of cement paste: Thixotropic behavior and structural breakdown, Cement and Concrete Research 39(1) (2009) 14-29.

[38] N. Roussel, G. Ovarlez, S. Garrault, C. Brumaud, The origins of thixotropy of fresh cement pastes, Cement and Concrete Research 42(1) (2012) 148-157.

[39] E. Secrieru, D. Cotardo, V. Mechtcherine, L. Lohaus, C. Schröfl, C. Begemann, Changes in concrete properties during pumping and formation of lubricating material under pressure, Cement and Concrete Research 108 (2018) 129-139.

[40] J. Vosahlik, K.A. Riding, D. Feys, W. Lindquist, L. Keller, S. Van Zetten, B. Schulz, Concrete pumping and its effect on the air void system, Materials and Structures 51(4) (2018) 94.

[41] A. Das, Y. Song, S. Mantellato, T. Wangler, R.J. Flatt, D.A. Lange, Influence of pumping/extrusion on the air-void system of 3D printed concrete, RILEM International Conference on Concrete and Digital Fabrication, Springer, 2020, pp. 417-427.

[42] O.H. Wallevik, J.E. Wallevik, Rheology as a tool in concrete science: The use of rheographs and workability boxes, Cement and Concrete Research 41(12) (2011) 1279-1288.

[43] A. Rust, M. Manga, Effects of bubble deformation on the viscosity of dilute suspensions, Journal of Non-newtonian Fluid Mechanics 104(1) (2002) 53-63.

[44] J.-Y. Petit, E. Wirquin, K.H. Khayat, Effect of temperature on the rheology of flowable mortars, Cement and Concrete Composites 32(1) (2010) 43-53.

[45] J. Spangenberg, N. Roussel, J. Hattel, H. Stang, J. Skocek, M. Geiker, Flow induced particle migration in fresh concrete: Theoretical frame, numerical simulations and experimental results on model fluids, Cement and Concrete Research 42(4) (2012) 633-641.

[46] J. Yammine, M. Chaouche, M. Guerinet, M. Moranville, N. Roussel, From ordinary rhelogy concrete to self compacting concrete: A transition between frictional and hydrodynamic interactions, Cement and Concrete Research 38(7) (2008) 890-896.

[47] N. Roussel, A. Lemaître, R.J. Flatt, P. Coussot, Steady state flow of cement suspensions: A micromechanical state of the art, Cement and Concrete Research 40(1) (2010) 77-84.

[48] T. Lecompte, A. Perrot, V. Picandet, H. Bellegou, S. Amziane, Cement-based mixes: Shearing properties and pore pressure, Cement and Concrete Research 42(1) (2012) 139-147.

[49] A. Perrot, Y. Mélinge, D. Rangeard, F. Micaelli, P. Estellé, C. Lanos, Use of ram extruder as a combined rheo-tribometer to study the behaviour of high yield stress fluids at low strain rate, Rheologica Acta 51(8) (2012) 743-754.

[50] Z. Toutou, N. Roussel, C. Lanos, The squeezing test: A tool to identify firm cement-based material's rheological behaviour and evaluate their extrusion ability, Cement and Concrete Research 35(10) (2005) 1891-1899.

[51] S.A.O. Nair, S. Panda, M. Santhanam, G. Sant, N. Neithalath, A critical examination of the influence of material characteristics and extruder geometry on 3D printing of cementitious binders, Cement and Concrete Composites 112 (2020) 103671.

[52] A. Perrot, C. Lanos, P. Estellé, Y. Melinge, Ram extrusion force for a frictional plastic material: Model prediction and application to cement paste, Rheologica Acta 45(4) (2006) 457-467.

[53] T. Van Pham, E. Mitsoulis, Viscoplastic flows in ducts, The Canadian Journal of Chemical Engineering 76(1) (1998) 120-125.

[54] A. Perrot, D. Rangeard, Y. Mélinge, Prediction of the ram extrusion force of cement-based materials, Applied Rheology 24(5) (2014) 34-40.

[55] R.A. Basterfield, C.J. Lawrence, M.J. Adams, On the interpretation of orifice extrusion data for viscoplastic materials, Chemical Engineering Science 60(10) (2005) 2599-2607.

[56] A. Perrot, C. Lanos, Y. Melinge, P. Estellé, Mortar physical properties evolution in extrusion flow, Rheologica Acta 46(8) (2007) 1065-1073.

[57] H. Khelifi, A. Perrot, T. Lecompte, D. Rangeard, G. Ausias, Prediction of extrusion load and liquid phase filtration during ram extrusion of high solid volume fraction pastes, Powder Technology 249 (2013) 258-268.

[58] F.A. Cardoso, V.M. John, R.G. Pileggi, Rheological behavior of mortars under different squeezing rates, Cement and Concrete Research 39(9) (2009) 748-753.

[59] T.T. Le, S.A. Austin, S. Lim, R.A. Buswell, R. Law, A.G. Gibb, T. Thorpe, Hardened properties of high-performance printing concrete, Cement and Concrete Research 42(3) (2012) 558-566.

[60] Y. Zhang, Y. Zhang, G. Liu, Y. Yang, M. Wu, B. Pang, Fresh properties of a novel 3D printing concrete ink, Construction and Building Materials 174 (2018) 263-271.

[61] Z. Ding, X. Wang, J. Sanjayan, P. Zou, Z.-K. Ding, A feasibility study on hpmc-improved sulphoaluminate cement for 3d printing, Materials 11(12) (2018) 2415.

[62] N. Khalil, G. Aouad, K. El Cheikh, S. Rémond, Use of calcium sulfoaluminate cements for setting control of 3D-printing mortars, Construction and Building Materials 157 (2017) 382-391.

[63] Z. Jianchao, T. Zhang, M. Faried, C. Wengang, 3D printing cement based ink, and it’s application within the construction industry, MATEC Web of Conferences, EDP Sciences, 2017, p. 02003.

[64] J. Ingaglio, J. Fox, C.J. Naito, P. Bocchini, Material characteristics of binder jet 3D printed hydrated csa cement with the addition of fine aggregates, Construction and Building Materials 206 (2019) 494-503.

[65] M. Chen, X. Guo, Y. Zheng, L. Li, Z. Yan, P. Zhao, L. Lu, X. Cheng, Effect of tartaric acid on the printable, rheological and mechanical properties of 3d printing sulphoaluminate cement paste, Materials 11(12) (2018) 2417.

[66] Y. Weng, M. Li, M.J. Tan, S. Qian, Design 3D printing cementitious materials via fuller thompson theory and marson-percy model, Construction and Building Materials 163 (2018) 600-610.

[67] G. Ma, L. Wang, Y. Ju, State-of-the-art of 3D printing technology of cementitious material—an emerging technique for construction, Science China Technological Sciences (2017) 1-21.

[68] V.N. Nerella, S. Hempel, V. Mechtcherine, Effects of layer-interface properties on mechanical performance of concrete elements produced by extrusion-based 3D-printing, Construction and Building Materials 205 (2019) 586-601.

[69] D.G. Soltan, V.C. Li, A self-reinforced cementitious composite for building-scale 3D printing, Cement and Concrete Composites 90 (2018) 1-13.

[70] Y.W. Tay, B. Panda, S.C. Paul, M.J. Tan, S.Z. Qian, K.F. Leong, C.K. Chua, Processing and properties of construction materials for 3d printing, Materials Science Forum, Trans Tech Publ, 2016, pp. 177-181.

[71] T.S. Rushing, G. Al-Chaar, B.A. Eick, J. Burroughs, J. Shannon, L. Barna, M. Case, Investigation of concrete mixtures for additive construction, Rapid Prototyping Journal 23(1) (2017) 74-80.

[72] P. Shakor, J. Sanjayan, A. Nazari, S. Nejadi, Modified 3D printed powder to cement-based material and mechanical properties of cement scaffold used in 3D printing, Construction and Building Materials 138 (2017) 398-409.

[73] M. Hambach, D. Volkmer, Properties of 3D-printed fiber-reinforced portland cement paste, Cement and Concrete Composites 79 (2017) 62-70.

[74] R. Lediga, D. Kruger, Optimizing concrete mix design for application in 3D printing technology for the construction industry, Solid State Phenomena 263 (2017).

[75] S. Lim, T. Le, J. Webster, R. Buswell, A. Austin, A. Gibb, T. Thorpe, Fabricating construction components using layered manufacturing technology, Global Innovation in Construction Conference, 2009, pp. 512-520.

[76] D. Marchon, S. Kawashima, H. Bessaies-Bey, S. Mantellato, S. Ng, Hydration and rheology control of concrete for digital fabrication: Potential admixtures and cement chemistry, Cement and Concrete Research (2018).

[77] B. Zareiyan, B. Khoshnevis, Effects of interlocking on interlayer adhesion and strength of structures in 3D printing of concrete, Automation in Construction 83 (2017) 212-221.

[78] O.A. Hisseine, N. Basic, A.F. Omran, A. Tagnit-Hamou, Feasibility of using cellulose filaments as a viscosity modifying agent in self-consolidating concrete, Cement and Concrete Composites 94 (2018) 327-340.

[79] B. Panda, N.A. Noor Mohamed, S.C. Paul, G. Bhagath Singh, M.J. Tan, B. Šavija, The effect of material fresh properties and process parameters on buildability and interlayer adhesion of 3D printed concrete, Materials 12(13) (2019) 2149.

[80] S. Ma, S. Kawashima, Rheological and water transport properties of cement pastes modified with diutan gum and attapulgite/palygorskite nanoclays for 3D concrete printing, RILEM International Conference on Concrete and Digital Fabrication, Springer, 2018, pp. 61-69.

[81] D. Asprone, F. Auricchio, C. Menna, V. Mercuri, 3D printing of reinforced concrete elements: Technology and design approach, Construction and Building Materials 165 (2018) 218-231.

[82] S.C. Paul, Y.W.D. Tay, B. Panda, M.J. Tan, Fresh and hardened properties of 3D printable cementitious materials for building and construction, Archives of Civil and Mechanical Engineering 18(1) (2018) 311-319.

[83] Z. Malaeb, H. Hachem, A. Tourbah, T. Maalouf, N. Zarwi, F. Hamzeh, 3D concrete printing: Machine and mix design, International Journal of Civil Engineering 6(6) (2015) 14-22.

[84] S. Al-Qutaifi, A. Nazari, A. Bagheri, Mechanical properties of layered geopolymer structures applicable in concrete 3D-printing, Construction and Building Materials 176 (2018) 690-699.

[85] K. El Cheikh, S. Rémond, N. Khalil, G. Aouad, Numerical and experimental studies of aggregate blocking in mortar extrusion, Construction and Building Materials 145 (2017) 452-463.

[86] Y. Zhang, Y. Zhang, W. She, L. Yang, G. Liu, Y. Yang, Rheological and harden properties of the high-thixotropy 3D printing concrete, Construction and Building Materials 201 (2019) 278-285.

[87] J.G. Sanjayan, B. Nematollahi, M. Xia, T. Marchment, Effect of surface moisture on inter-layer strength of 3D printed concrete, Construction and Building Materials 172 (2018) 468-475.

[88] A. Rahul, M. Santhanam, H. Meena, Z. Ghani, 3D printable concrete: Mixture design and test methods, Cement and Concrete Composites 97 (2019) 13-23.

[89] B. Zhu, J. Pan, B. Nematollahi, Z. Zhou, Y. Zhang, J. Sanjayan, Development of 3D printable engineered cementitious composites with ultra-high tensile ductility for digital construction, Materials & Design 181 (2019) 108088.

[90] S. Cho, J. Kruger, F. Bester, M. van den Heever, A. van Rooyen, G. van Zijl, A compendious rheo-mechanical test for printability assessment of 3D printable concrete, RILEM International Conference on Concrete and Digital Fabrication, Springer, 2020, pp. 196-205.

[91] E. Berodier, K. Scrivener, Understanding the filler effect on the nucleation and growth of C-S-H, Journal of the American Ceramic Society 97(12) (2014) 3764-3773.

[92] Y. Chen, C. Romero Rodriguez, Z. Li, B. Chen, O. Çopuroğlu, E. Schlangen, Effect of different grade levels of calcined clays on fresh and hardened properties of ternary-blended cementitious materials for 3D printing, Cement and Concrete Composites 114 (2020) 103708.

[93] C. Hu, F. de Larrard, The rheology of fresh high-performance concrete, Cement and Concrete Research 26(2) (1996) 283-294.

[94] T. Wangler, E. Lloret, L. Reiter, N. Hack, F. Gramazio, M. Kohler, M. Bernhard, B. Dillenburger, J. Buchli, N. Roussel, Digital concrete: Opportunities and challenges, RILEM Technical Letters 1 (2016) 67-75.

[95] M. Bellotto, Cement paste prior to setting: A rheological approach, Cement and Concrete Research 52 (2013) 161-168.

[96] R.J. Flatt, P. Bowen, Yodel: A yield stress model for suspensions, Journal of the American Ceramic Society 89(4) (2006) 1244-1256.

[97] J.-Y. Petit, K.H. Khayat, E. Wirquin, Coupled effect of time and temperature on variations of yield value of highly flowable mortar, Cement and Concrete Research 36(5) (2006) 832-841.

II. CHARACTERIZATION OF PRINT MATERIAL EXTRUDABILITY USING RHEOLOGY AND DESORPTIVITY

Kavya Vallurupalli, Nicolas Ali Libre, Kamal H. Khayat*

Department of Civil, Architectural and Environmental Engineering, Missouri University of Science and Technology, Rolla, Missouri, USA

*Corresponding author

ABSTRACT

Successful implementation of extrusion-based 3D printing (3DP) requires the development of print materials with an adapted rheology. In this study, filtration characteristics in addition to the rheological properties are investigated to characterize the extrudability of printing materials and establish the “printability window”, i.e., the acceptable range of material properties for a successful printing. The extrudability of mortar mixtures was measured as the maximum force needed for the ram extrusion of the material. The fluid filtration rate was assessed in terms of desorptivity (D_e) using a pressure filtration cell setup. The yield stress (τ_y), plastic viscosity (μ_p), and D_e were varied by changing the water-to-cement ratio (w/c), superplasticizer (SP) dosage, and welan gum (WG) content. The influence of the material properties on extrudability was examined. Regression analysis indicated that during extrusion-based 3DP, the τ_y and D_e have a more significant effect on extrudability compared to μ_p. The reduction in the w/c of mortar with a fixed mini-slump flow from 0.35 to 0.25 led to 80% decrease in D_e and improvement in extrudability. The influence on D_e varied depending on the SP dosage and overhead pressure applied during the filtration test. For a nozzle size of 9 mm, adequate shape-retaining ability of extruded material can be secured at mortar τ_y greater than 100 Pa. The incorporation of 0.1% WG increased μ_p and lowered D_e by up to 70% and 98%, respectively. Such reduction in D_e enabled extrusion of print materials with high τ_y (> 400 Pa). For the extrusion parameters considered, acceptable ranges of material properties for 3DP were identified as τ_y 100- 470 Pa, μ_p 10-60 Pa.s, and $D_e < 3x10^{-3}$ $s^{-0.5}$ at 120 kPa overhead pressure. The results of this study indicate that the assessment of rheological properties alone is not sufficient to characterize the extrudability of the print material and fluid filtration during extrusion should be adjusted for a successful 3DP.

Keywords**:** 3D Printing; Extrudability; Fluid filtration; Printability window; Rheology.

1. INTRODUCTION

Over the past decade, there has been a growing interest in 3D printing (3DP) of cement-based materials in concrete construction. The main advantage of 3DP over conventional construction is the elimination of formwork and the enabling of printing of topologically optimized structures. This has the potential to reduce material usage, lower construction costs, and enhance sustainability [1-3]. Two different 3DP techniques are mainly applied for cement-based materials (i.e., particle-bed binding and material extrusion [4, 5]). The current work focuses on extrusion-based 3DP using a ram extruder setup. The extrusion-based 3DP involves the extrusion of the print material through a nozzle into filaments that are deposited layer-by-layer at a controlled printing speed [6-8]. Figure 1a illustrates the extrusion process of 3DP using a ram extruder. The ram extrusion involves filling the print material in a barrel and application of force (F_E) on the ram to push the material into a nozzle located at the end of the barrel.

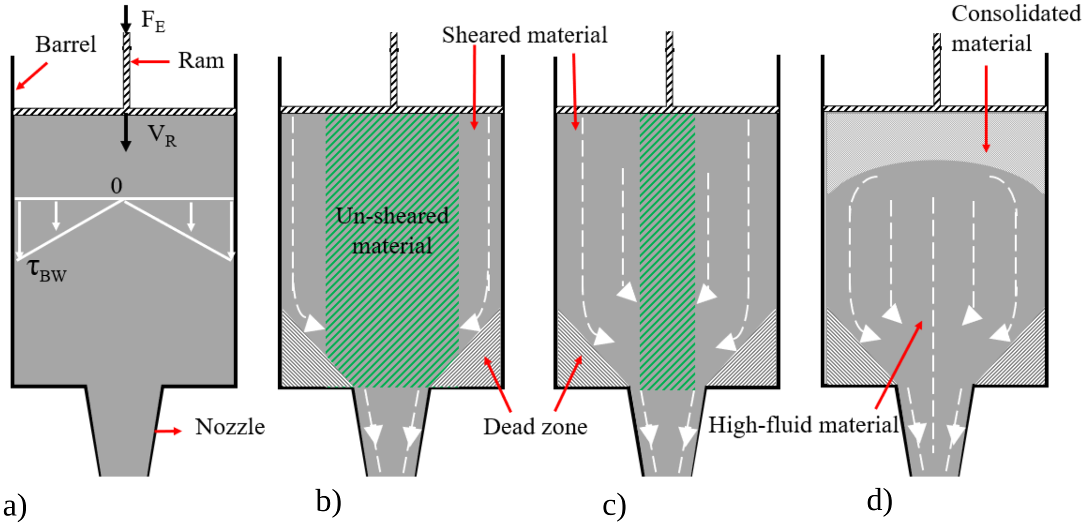

Figure 1. Ram extrusion process: a) ram extruder setup; b) plastic flow behavior; c) visco-plastic flow behavior; and d) frictional-plastic flow behavior (adapted from [9]).

During ram extrusion (Figure 1a), the application of F_E results in different material flow behaviors (i.e., plastic, visco-plastic, and frictional-plastic) depending on the material rheology and fluid filtration characteristics. For plastic and visco-plastic flow behaviors, the material stays homogenous. However, the extent of shearing in the material varies. In the case of plastic flow behavior, only the print material close to the barrel wall undergoes shearing. While the remaining material moves along the extruder unsheared as indicated in green in Figure 1b. For visco-plastic flow behavior in Figure 1c, most of the print material is sheared during the extrusion. Friction-plastic flow behavior occurs when the application of F_E results in migration of the fluid within the material toward the nozzle. This causes the formation of dry and consolidated material near the ram, as shown in Figure 1d, which can lead to blockage during extrusion.

The material flow behavior within the extruder has a significant effect on extrudability. The extrudability in this study is assessed in terms of maximum F_E (i.e., high extrudability implied lower value of F_E) [10-12]. The influence of material rheology (i.e., yield stress (τ_y) and plastic viscosity (μ_p)) and fluid filtration characteristics on flow behavior and extrudability are summarized in Table 1.

Table 1. Influence of print material properties on flow behavior and extrudability [9].

Flow behavior	**Print material property**		**Extrudability**[†]
	τ_y/μ_p[*]	**Fluid filtration**	
Plastic	High	Low	High
Visco-plastic	Low	Low	Medium
Frictional-plastic		High	Poor

[*] High and low values correspond to B_N of >100 and ≤100, respectively.
[†] High extrudability implies lower F_E needed for extrusion of print material

Perrot et al. [13] noted that during the extrusion of a homogenous material, the flow behavior is a function of τ_y, μ_p, extrusion speed (V_R), and barrel diameter (D_B). The influence of these parameters can be assessed using the Bingham number (B_N), as shown in Eq. 1 [9].

$$B_N = \frac{\tau_y D_B}{8\mu_p V_R} \qquad \text{Eq. 1}$$

The high and low values of τ_y/μ_p for plastic and visco-plastic flow behaviors in Table 1 correspond to B_N values of > 100 and ≤100, respectively. The fluid filtration needs to be significantly low to reduce the water migration in the cement paste and avoid the formation of dry and consolidated material when the printing material is subjected to a high pressure during the extrusion. The degree of fluid filtration is a function of the filtration characteristics of the print material, extruder dimensions, and ram speed [13].

The fluid filtration characteristics of the print material can be assessed in terms of desorptivity (D_e) [14, 15]. The D_e is the measurement of the rate of forced bleeding of the material under a given pressure gradient. Unlike B_N, no acceptable ranges of D_e are available in the literature to ensure material homogeneity during extrusion. Additionally, in most studies, the optimization of print materials is mainly done to meet the rheology requirements [16-18] with limited emphasis on D_e [15, 19]. Le et al. [8] noted for extruder with nozzle diameter of 9 mm, the print materials with τ_y values between 300 - 600 Pa are suitable for extrusion of shape-stable layers. On the other hand, the τ_y values between 1200 - 1400 Pa were considered suitable by Panda et al. [17] during the extrusion of geopolymer mortars using a nozzle with opening of size 15 x 30 mm. Such wide variation in the acceptable range of τ_y is partly due to the variation in the extrusion parameters selected [20], the rheometer geometry, and test protocols used for measuring τ_y [21].

The current study evaluates the importance of both rheology and D_e on printability which is currently missing in the literature. The mortar mixtures with different rheological and fluid filtration characteristics were prepared by changing the water-to-cement ratio (w/c), superplasticizer (SP) dosage, and welan gum (WG) content. The influence of these mixture proportioning parameters and material properties (i.e., τ_y, μ_p, and D_e) on the extrudability (determined by the maximum F_E) was examined. Based on the τ_y, μ_p, and D_e parameters and the maximum F_E values, a “printability window” was established. The printability window refers to the acceptable range of material properties within which the material can be extruded into shape-stable layers. The statistical significance of the effect of τ_y, μ_p, and D_e parameters on the extrudability was also evaluated using regression analysis. The printability window proposed in this paper can be used as a practical guideline for material properties during the selection and optimization of mixtures for extrusion-based 3DP.

2. MATERIALS AND EXPERIMENTAL PROCEDURES

2.1. MATERIALS AND MIXTURE PROPORTIONS

In this study, Type I/II Portland cement conforming to ASTM C 150 was used. The chemical composition of the cement is shown in Table 2. The specific gravity and Blaine fineness of the cement were 3.14 and 390 m^2/kg, respectively. The nominal maximum size of aggregate and relative content of the sand were 2 mm and 40%, by volume of mortar, respectively. These values were selected to minimize the risk of aggregate blockage in the extruder [22]. The specific gravity and absorption values of the sand were 2.58% and 2.24%, respectively. The particle size distribution of the cement and sand are shown in Figure 2. A polysaccharide-based WG powder with a specific gravity of 0.8 was used to modify the rheology and fluid filtration characteristics of mortar mixtures. A polycarboxylate-based SP with 23% solid mass content and 1.05 specific gravity was also used. The dosage rate of the SP was varied to maintain an initial mini-slump flow of 170 ± 10 mm for the mixtures made with WG. For other mixtures, the SP dosage was varied to secure different flowability values.

Eight mortar mixtures with different w/c (0.25 and 0.35), SP dosages (0%, 0.09%, 0.11%, 0.22%, and 0.43%, by mass cement), and WG contents (0%, 0.1%, 0.2%, and 0.3%, by mass of cement) were prepared. The mixture proportions and initial mini-slump flow values (i.e., flow values measured 20 min after water addition) of the print materials are shown in Table 3. The mortar mixtures were prepared using a 12-L capacity mixer.

The mixing procedure of the mortars involved: 1) dry mixing of sand and cement at 1 rps for 2 min; 2) gradual addition of water along with SP to the dry materials and mixing at 2 rps for 3 min; 3) resting the material for 1 min followed by final mixing at 2 rps for 3 min. In the case of mixtures with WG, the WG was pre-mixed with water+SP for 3 min using a blender and was added to the dry materials in step 2 of the mixing process. The slump flow, rheology, and extrusion measurements were started after 20 min from water addition.

2.2. RHEOLOGY

The τ_y and μ_p of mortar mixtures were measured using a coaxial cylinder rheometer with inner and outer radii of 50 and 60 mm, respectively. The rheometer cylinder was filled with the mortar sample in two layers, and each layer was rodded 25 times with a tamping rod. The rheology testing protocol involved pre-shearing of mortar at 0.5 rps for 25 s followed by a step-wise drop of the shear rate from 0.5 to 0.025 rps in 10 steps with each shear rate applied for 5 s. The average value of torque at each shear rate was recorded, and the τ_y and μ_p values were estimated using the Reiner-Riwlin equations for the Bingham model [23]. The rheological measurements were determined initially at 20 min after water addition and thereafter up to 220 min. Between each test, the sample was hand-mixed for 30 s and was covered to minimize water evaporation.

Table 2. Oxide composition of Type I/II cement.

Oxide	Mass (%)
CaO	68.3
SiO_2	19.0
Al_2O_3	3.9
Fe_2O_3	3.5
SO_3	2.4
MgO	1.7
Na_2O eq.	0.6

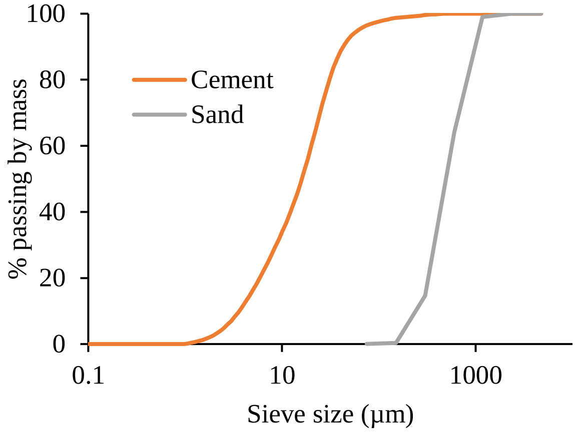

.

Figure 2. Particle size distributions for cement and sand.

Table 3. Mixture proportions and initial mini-slump flow of investigated mixtures.

Mixture*	Cement (kg/m^3)	Water (kg/m^3)	Sand (kg/m^3)	SP demand (kg/m^3)	WG (kg/m^3)	Initial mini-slump flow (±10 mm)
0.35W	899	315	1032	-	-	120
0.25W0.09SP	1049	266	1031	0.9	-	120
0.25W0.11SP	1049	266	1031	1.1	-	170
0.25W0.22SP	1048	266	1030	2.3	-	280
0.25W0.43SP	1045	266	1028	4.5	-	340
0.25W0.7SP0.1WG	1041	264	1024	7.2	1.0	170
0.25W1.3SP0.2WG	1034	263	1016	13.5	2.1	170
0.25W1.8SP0.3WG	1027	261	1010	18.8	3.1	170

*0.25W1.8SP0.3WG indicates a 0.25 w/c, SP dosage and WG content of 1.8% and 0.3%, by mass of cement, respectively

2.3. FLUID FILTRATION

The D_e of the mortar mixtures was assessed using a filtration cell test setup shown in Figure 3a. The test consisted of a rigid metallic cylinder fitted with a metal screen and filter paper of pore size 2 µm placed at the bottom against the draining surface. The cylinder was filled with approximately 750 gm (approximately 320 ml) of mortar sample in two layers with each layer rodded 25 times with a tamping rod. The cylinder assembly was placed in the test frame, and an overhead pressure was applied on the mortar using CO_2 gas. The overhead pressure was applied for 5 min, and the forced bleed water was collected using a 10 ml graduated cylinder. The mortar samples were tested at different ages starting from 20 min to up to 220 min (± 10 min) after water addition. At each age, the filtration test was conducted using a freshly mixed samples subjected to five different overhead pressures (i.e., 120, 180, 240, 300, and 360 kPa (± 10 kPa)).

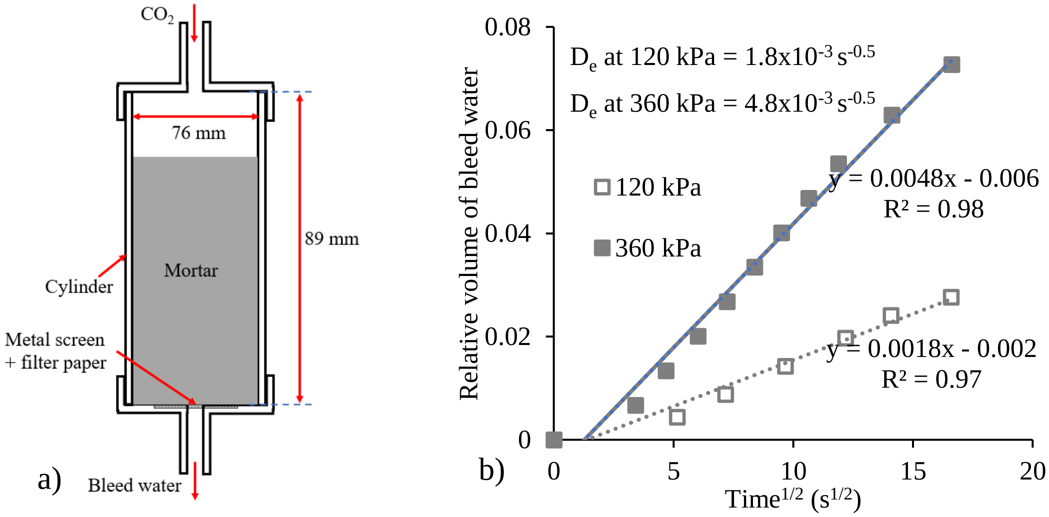

Figure 3. Filtration test: a) schematic of filtration cell test setup; and b) typical variations in the relative volume of forced bleed water as a function of time (up to 5 min) for two overhead pressures of 120 and 360 kPa.

Three pressure cells were available to conduct the pressure filtration tests simultaneously. The D_e at each overhead pressure was estimated by plotting the relative amount of filtrated water to the square root of time, as shown in Figure 3b. The relative amount of filtrated water corresponds to the volume of collected forced bleed water divided by the total water content in the mortar sample. A high value of D_e implies high fluid filtration rate that can lead to friction-plastic flow behavior during the extrusion of the mortar.

2.4. RAM EXTRUSION

The extrudability of a mortar sample is defined as the ability of the material to be extruded without any blockage [16, 24]. The extrudability of mortar mixtures was evaluated using a custom-designed displacement-controlled ram extrusion set up (in Figure 4a) with barrel diameter (D_B) of 39 mm and nozzle diameter (D_N) of 9 mm, as shown in Figure 4b [25]. The extruder was powered by a stepper motor calibrated to apply a maximum load of 135 N to avoid failure of the extruder. The mortar mixtures were extruded with a constant ram speed (V_R) of 2.5 mm/s. Before each test, the inner surface of the barrel and ram were lubricated using silicone oil to minimize the wall friction. Additionally, the extrusion test was carried out on an empty ram to determine the force needed for pushing an empty ram extruder. A mortar sample of 140 ml (approximately 330 gm) was added to the barrel which corresponded to the barrel length (L_B) of 120 mm (in Figure 4b). A drastic increase in F_E was reported by Perrot et al. [26, 27] when the ram approached the dead-zone length (L_{DZ}). To minimize the effect of dead-zone on F_E, only a portion of mortar within the extruder, 96 ml of mortar corresponding to extruder length (L_E) of 80 mm was extruded. One way to measure the extrudability is measuring the maximum F_E needed to extrude the material, as shown in Figure 4c [25]. A higher maximum F_E implies low extrudability, and the extrudability was assessed at different ages of mortar starting from 20 min after water addition. Additionally, the open time was determined as the age of the print material beyond which the material could not be extruded without blockage. The blockage of the print material implied that the force needed to extrude the material exceeds the load limit (135 N) of the extruder setup. In this study, the D_B and V_R were fixed at 39 mm and 2.5 mm/s, respectively, and the parameter B_N was primarily a function of τ_y and μ_p, as shown in Eq. 2.

$$B_N = \frac{\tau_{dy} D_B}{8\mu_p V_R} = \frac{\tau_{dy}(39\ \text{mm})}{8\mu_p(2.5\ \text{mm/s})} \qquad \text{Eq. 2}$$

3. RESULTS AND DISCUSSIONS

3.1. INFLUENCE OF W/C AND WG CONTENT ON SP DEMAND

The influence of w/c and WG content on material rheology and fluid filtration characteristics was examined by comparing the results of mortar mixtures with fixed initial mini-slump flow values. As indicated in Table 3, the mixture prepared with 0.35 w/c required no SP to achieve the target initial mini-slump flow of 120 mm. However, with the reduction of w/c to 0.25, 0.09% of SP was required for maintaining the mini-slump flow. The SP demand increased to 0.7%, 1.3%, and 1.8% for mixtures made with WG contents of 0.1%, 0.2%, and 0.3%, respectively, for mortars made with 0.25 w/c. A similar increase in SP demand was observed by [28, 29] with an increase in the WG content for grout and ultra-high performance mortar mixtures. Long-chain polymers of WG can adhere to the water molecules and fix some of the mixing water, and additional water can be entrapped between the adjacent polymer chains of WG [30, 31].

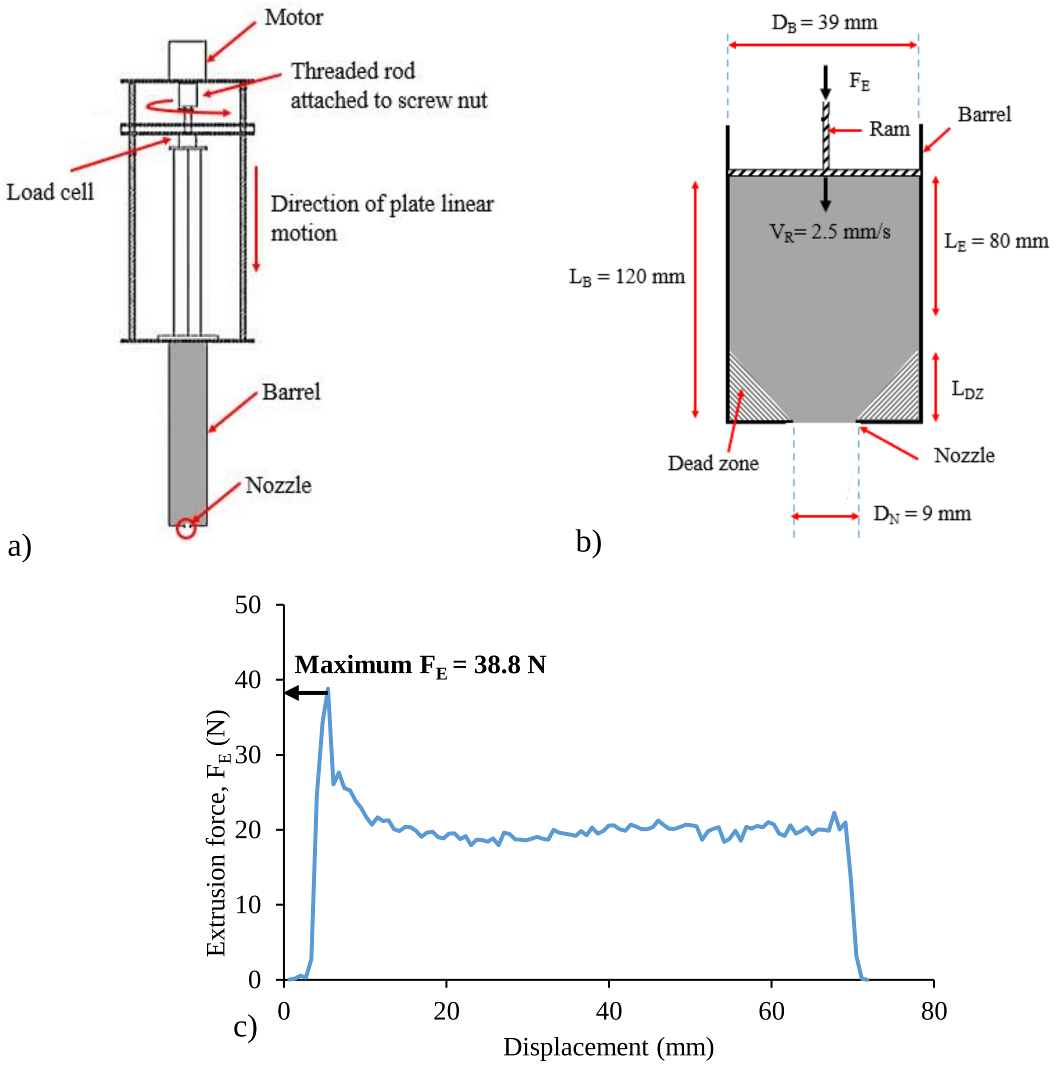

Figure 4. Extrusion test: a) schematic of ram extruder setup; b) close-up of barrel and nozzle; and c) typical load vs. displacement data from ram extrusion test.

3.2. INFLUENCE OF MIXTURE PROPORTIONING PARAMETERS ON MATERIAL PROPERTIES

3.2.1. Effect of w/c. The influence of w/c on rheology and D_e was evaluated by comparing these results obtained with the 0.35W and 0.25W0.09SP mixtures. The τ_y and μ_p values of these mixtures are shown in Figure 5. In terms of τ_y, no significant difference was observed for both mixtures at 20, 50, and 90 min of age. Conversely, a 400% to 650% increase in μ_p occurred with the decrease in w/c, despite the fixed mini-slump flow values. The high μ_p values for the 0.25W0.09SP mixture at different times were due to the lower amount of water content [32]. However, the lack of such effect on τ_y was due to the opposing effect of low w/c and SP addition [33]. The lowering of w/c from 0.35 to 0.25 also resulted in a four-fold increase in the rate of increase in μ_p with time. Such a significant increment is in agreement with previous studies [34, 35], and it was attributed to the increased rate of flocculation due to lower inter-particle distance between the cement particles of the lower w/c mixture.

The B_N values were calculated using Eq. 2 and ranged from 142 to 264 for the 0.35W mixture and 30 to 33 for the 0.25W0.09SP mixture. Such decrease in B_N from values greater than 100 to less than 100 with the decrease in w/c from 0.35 to 0.25 suggests a change in the material flow behavior from plastic to visco-plastic flow behavior. As per Table 1, such a change in flow behavior typically results in a decrease in extrudability (i.e., increase in the maximum F_E).

Figure 6 shows the variations in D_e with applied overhead pressure for 0.35W and 0.25W0.09SP mixtures after 20 and 90 min of water addition. These results indicate an increase in D_e with the increase in overhead pressure from 120 to 360 kPa. Additionally, approximately 80% lower D_e values were observed for the 0.25W0.09SP mixture compared to the 0.35W mixture. The low D_e of the former mixture can be attributed to the relatively lower amount of water available for filtration and the higher level of μ_p. The high D_e results for the latter mixture suggests the possibility of fluid filtration during extrusion resulting in frictional-plastic flow behavior and poor extrudability.

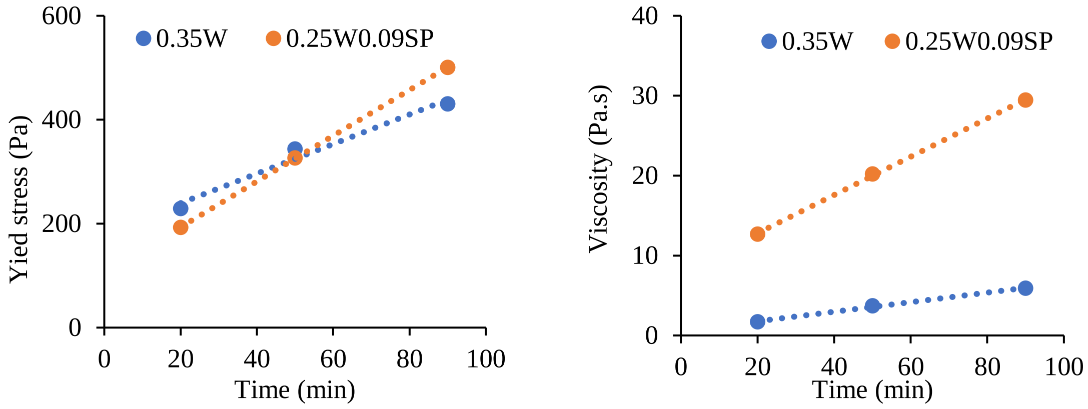

Figure 5. Influence of w/c on τ_y (left) and μ_p (right) at initial mini-slump flow of 120 mm.

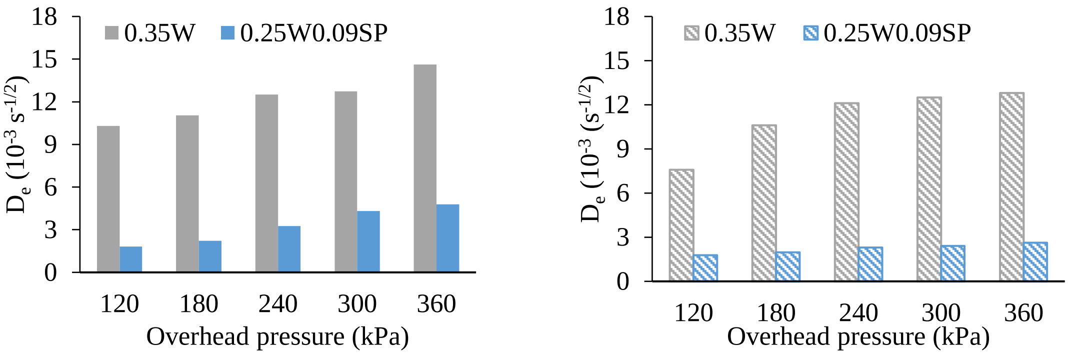

Figure 6. Influence of w/c dosage on D_e at 20 min (left) and 90 min (right) at initial mini-slump flow of 120 mm.

Based on the above results, the decrease in B_N to below 100 with the reduction of w/c from 0.35 to 0.25 suggests a lower level of extrudability. On the other hand, the decrease in D_e with the decrease in w/c suggests an improvement in extrudability. These contradicting effects of rheology and D_e on extrudability indicate that the assessment of rheological properties alone is not sufficient to characterize the extrudability of the print material during extrusion-based 3DP.

3.2.2. Effect of SP Dosage. The influence of SP dosage on material properties was evaluated by comparing the results of the 0.25W0.09SP, 0.25W0.11SP, 0.25W0.22SP, and 0.25W0.43SP mixtures that had different SP dosages and initial mini-slump flow values. The increase in SP dosage results in de-flocculation of cement particles and increase in the amount of free water [36]. The increase in SP dosage from 0.09% to 0.43% led to over 200% increase in mini-slump flow (Table 3) and over 90% drop in τ_y and μ_p 90%, as shown in Figure 7. The increase in SP dosage also reduced the rate of increase of τ_y and μ_p with time. These changes are due to the decrease in the rate of flocculation as a result of increased inter-particle distance between cement particles in the presence of SP [37-39].

The B_N values for the 0.25W0.09SP, 0.25W0.11SP, 0.25W0.22SP, and 0.25W0.43SP mixtures were in the ranges of 30 to 33, 14 to 34, 5 to 8, and 4 to 6, respectively. The relatively low values of B_N (< 100) suggest visco-plastic flow behavior during ram extrusion. Additionally, the 25% to 90% reduction in B_N with the increase in SP dosage from 0.09% to 0.43% suggests an increase in viscosity contribution to the extrusion force. The low B_N value reflects that higher volume of the material within the extruder is sheared during the extrusion process [40, 41].

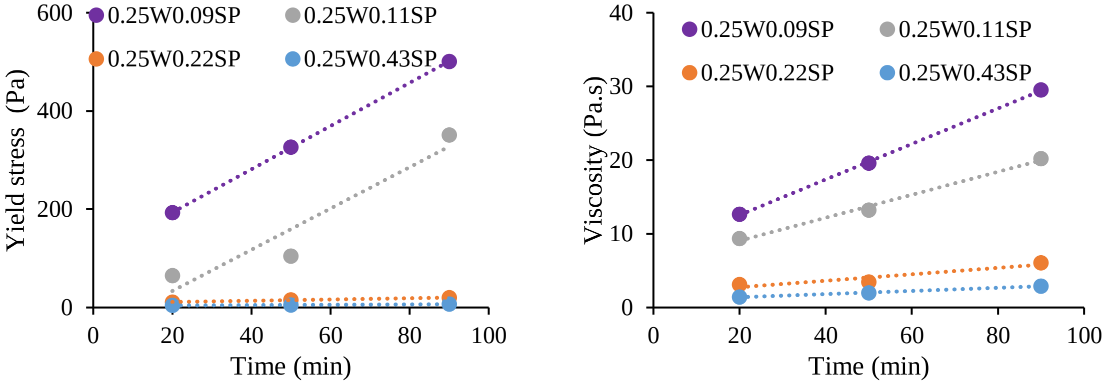

Figure 7. Influence of SP dosage on τ_y (left) and μ_p (right).

Figure 8 shows the variation in D_e with overhead pressure for mixtures with different SP dosages. The influence of SP dosage on D_e varied depending on the applied pressure. At low pressures (i.e., 120, 180, and 240 kPa), the increase in SP dosage from 0.09% to 0.11% increased the D_e by 70%. However, further increase in SP dosage to 0.22% and 0.43% had an opposite effect. Such contradicting effect of SP on D_e can due to the release of entrapped water between flocculated cement particles and consequent increase in free water available for filtration [15] and the dispersion of cement particles and consequent enhancement of particle packing and decrease of the material permeability [29]. At 0.22% and 0.43% SP dosages, the low permeability of mortar mixtures resulted in lower values of D_e [15, 29]. The lack of such decrease at high overhead pressures (i.e., 300 and 360 kPa) suggests that the D_e at high pressure values is less sensitive to permeability characteristics of material [42].

For the investigates mixtures with different SP dosages, the low B_N values indicate a visco-plastic behavior. Additionally, the decrease in τ_y and μ_p with the increase in SP dosage suggests lower F_E is needed to extrude the mixture with high SP (i.e., increased extrudability) [13, 20]. However, the influence of SP dosage on D_e varied depending on the amount of SP added and the overhead pressure applied. These D_e results suggest that the influence of SP on extrudability is not straightforward, and that increasing the SP dosage does not guarantee an improvement in the extrudability.

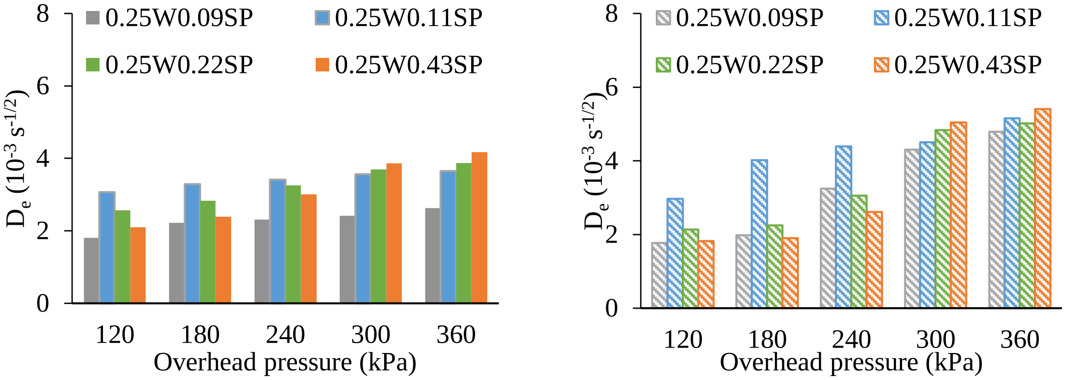

Figure 8. Influence of SP dosage on D_e at 20 min (left) and 90 min (right).

3.2.3. Effect of WG Content. The rheology and D_e results of mortar mixtures with WG contents of 0, 0.1%, 0.2%, and 0.3% are shown in Figure 9 and Figure 10, respectively. The increase in WG content necessitated increasing the SP demand and the rheology and D_e results presented were due to the combined action of WG and SP. In Figure 9, the rate of increase in τ_y with time dropped by 90% with the increase in WG content from 0 % to 0.1% and consequent increase in SP dosage from 0.11% to 0.7%, respectively. However, a significant increase (30% to 190%) in μ_p was observed with the addition of WG despite the increased SP demand. The addition of 0.1% and 0.2% WG increased the rate of increase in μ_p while no such increase occurred at 0.3% WG due to the high SP demand [29]. The values of B_N for the 0.25W0.11SP, 0.25W0.7SP0.1WG, 0.25W1.3SP0.2WG, and 0.25W1.8SP0.3WG mixtures were in the ranges of 14 to 34, 7 to 10, 6 to 8, and 5 to 6, respectively. The significantly lower B_N values for mixtures with

WG (i.e., lower than 100) indicate visco-plastic flow behavior. While the drastic increase in μ_p with the addition of WG suggests a higher F_E may be needed to shear the mortar during extrusion (i.e., decreased extrudability).

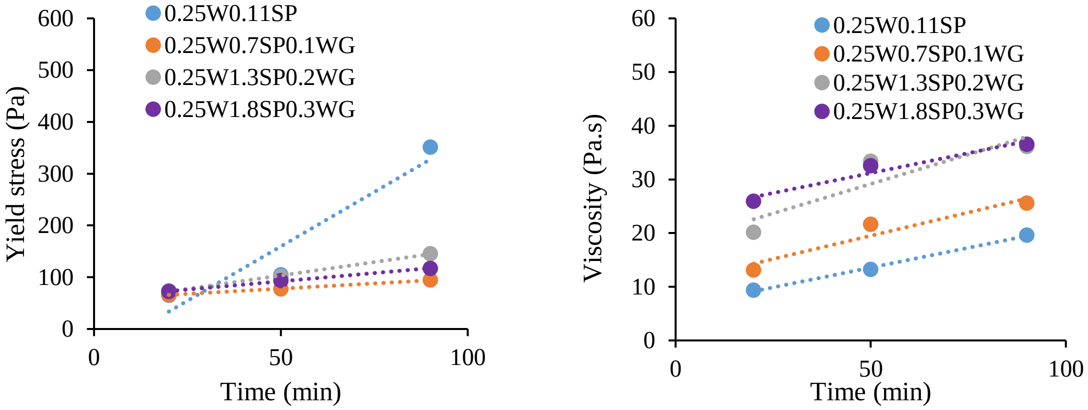

Figure 9. Influence of WG content on τ_y (left) and μ_p (right) at initial mini-slump flow of 170 mm.

The D_e results (in Figure 10) indicate a drastic reduction (94% to 98%) in fluid filtration with the addition of WG. These results are in agreement with the low fluid filtration and high water retention reported by [30, 43] for cement paste mixtures with WG. Such reduction can be partly attributed to the reduction in free water available for filtration [29], increase in the pore solution viscosity, which could reduce the rate of fluid filtration [43, 44]. Additionally, Desbrieres [45] and Brumaud et al. [46] observed that the long-chain polymers (such as WG) can aggregate and partly fill the pores in the mortar during fluid filtration, consequently reducing D_e. In the present study, the low D_e of WG mixtures can also be partly attributed to the decreased permeability of mortars with increased SP demand. The low D_e of WG mixtures indicates low migration of the fluid and homogenous shearing of the material during extrusion (i.e., visco-plastic (due to low B_N) as opposed to frictional plastic flow behavior).

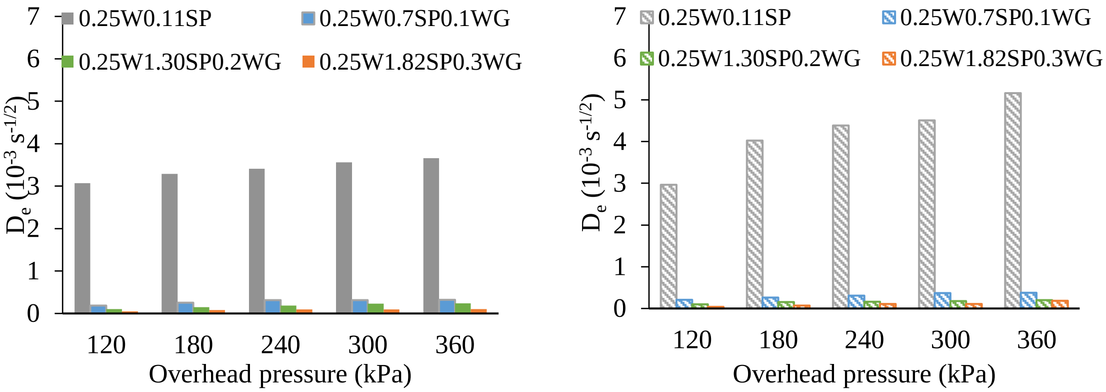

Figure 10. Influence of WG content on D_e at 20 (left) and 90 (right) min age (initial mini-slump flow of 170 mm).

Table 4 summarizes the observed influence of w/c, SP dosage, and WG content on material properties and extrudability. The increase in w/c at fixed mini-slump flow had a limited effect on τ_y but reduced μ_p and increased D_e. The drop in the μ_p lead to change in B_N values from lower than 100 to over 100 suggesting an improvement in extrudability. Whereas the increase in D_e with w/c, indicate a high rate of bleed water filtration and drop in the extrudability. The increase in the SP dosage had reduced both τ_y and μ_p (improvement in extrudability) and had a varied effect on D_e (improvement or reduction in extrudability). The use of WG at fixed mini-slump flow increased μ_p with a limited effect on τ_y (suggesting a drop in extrudability) and drastically reduced D_e (increase in extrudability). Such opposing effect of rheology and fluid filtration on extrudability highlights the importance of measuring both these properties to assess the suitability of print materials for extrusion-based 3DP.

Table 4. Influence of mixture parameters on material properties and extrudability.

Increase of parameter	**Rheology**			**Fluid filtration**	
	τ_y	**μ_p**	**Effect on extrudability**	**D_e**	**Effect on extrudability**
w/c	Fixed*	Decrease	Improve	Increase	Deteriorate
SP dosage	Decrease	Decrease	Improve	Increase/Decrease	Deteriorate / Improve
WG content	Fixed*	Increase	Deteriorate	Decrease	Improve

* For mixtures with different w/c and WG contents, τ_y and mini-slump flow values were fixed.

3.3. RELATIONSHIP BETWEEN MATERIAL PROPERTIES AND EXTRUDABILITY

During the ram extrusion, the print materials with low τ_y were able to flow out of the nozzle due to gravity without any need for the application of F_E. However, shape stability was not adequate. A minimum τ_y of 100 Pa was required to extrude shape-retaining filaments. As mentioned, the load capacity of the ram extruder was 135 N which corresponds to the pressure value of 113 kPa for D_B of 39 mm (in Figure 4b). This means for the print material, the maximum rate of fluid filtration during the ram extrusion is equivalent to the D_e values measured at overhead pressure of 120 kPa (± 10 kPa) during the fluid filtration test. Table 5 shows the material properties along with estimated B_N and maximum F_E results of the mixtures at ages where τ_y values were larger than 100 Pa.

For the 0.35W mixture, the print material could not be extruded at 20, 50, or 90 min. This was because the F_E needed exceeded the load capacity (135 N) of the extruder. On the other hand, the 0.25W0.09SP mixture was extrudable with a maximum F_E of 45 and 95 N at 20 and 50 min, respectively. These results indicate an improvement in the extrudability with the decrease in w/c from 0.35 to 0.25. Such improvement, despite the drop in B_N from over 100 to below 100, can be attributed to the lower D_e and consequent change in material flow behavior from frictional plastic to visco-plastic.

For mixtures with 0.25 w/c, the increase in SP dosage from 0.09% to 0.11%, reduced τ_y values. As a result, the 0.25W0.11SP mixture was too flowable and not suitable for extrusion at 20 min. However, at 50 and 90 min, the τ_y was over 100 Pa, and the material was extrudable. The rheological properties were identical for the 0.25W0.09SP mixture at 50 min and 0.25W0.11SP mixture at 90 min (i.e., τ_y = 330-340 Pa and μ_p = 20 Pa.s). However, the D_e was 67% higher for the 0.25W0.11SP mixture resulting in 11% increase in maximum F_E. For mixtures with higher SP dosages (i.e., 0.25W0.22SP and 0.25W0.43SP mixtures), the τ_y was lower than 100 Pa until 220 min of testing and so extrudability could not be assessed.

The mixtures with WG were too flowable at early ages, i.e., at 20 and 50 min, but were extrudable at later ages (up to 220 min of testing). Compared to the mixtures with no WG, mixtures containing WG were extrudable for a longer time indicating an increased open time with the combined use of WG and SP. The higher μ_p and consequently lower B_N values for mixtures with WG suggest that the print material undergoes visco-plastic flow during the extrusion. Additionally, for a given τ_y, the maximum F_E needed to extrude the material was lower for mixtures with WG due to the reduction in the D_e.

As shown in Figure 11, the enhanced extrudability (i.e., reduction in maximum F_E) was especially significant for mixtures with high values of τ_y. Furthermore, the addition of WG enabled extrusion of print material with high τ_y (i.e., greater than 400 Pa). The ability to extrude print materials with such high yield stress enables printing of shape-retaining layers of larger thickness. It also facilitates faster printing times by reducing the time gap required between the layers to ensure the shape-stability of the printed elements [47].

Table 5. Material properties and maximum extrusion of investigated mixtures.

Mixtures	**Time (min)**	**τ_y (Pa)**	**μ_p (Pa.s)**	**D_e at 120 kPa (10^{-3} $s^{-0.5}$)**	**B_N**	**Max F_E (N)**
0.35W	20	229	2	10.33	223	>135
	50	343	4	9.87	167	>135
	90	431	6	7.58	140	>135
0.25W0.09SP	20	193	13	1.81	29	45
	50	326	20	1.78	32	95
	90	501	29	1.77	34	>135
0.25W0.11SP	50	105	13	3.01	16	41
	90	351	20	2.97	34	105
0.25W0.7SP0.1WG	130	100	28	0.21	7	28
	180	118	32	0.20	7	34
	220	174	48	0.18	7	46
0.25W1.3SP0.2WG	90	145	36	0.12	8	30
	130	185	37	0.10	10	39
	180	340	39	0.09	17	45
	220	470	44	0.05	21	63
0.25W1.8SP0.3WG	90	117	37	0.06	6	31
	130	150	44	0.05	7	35
	180	196	47	0.04	8	41
	220	346	58	0.04	12	70

The material properties and extrudability results of the investigated mixtures were used for the development of the printability window shown in Figure 12. The printability window indicated as a blue box encompasses the range of material properties where the print material is extrudable into shape stable layers. The lower limits for τ_y and μ_p correspond to the minimum values needed to extrude shape stable layers and to limit fluid filtration during extrusion, respectively. While the upper limits for τ_y and μ_p correspond to the maximum shear the extruder can exert on the material beyond which the load capacity of the extruder is exceeded. The upper limit for D_e limits the fluid filtration and frictional plastic flow behavior during extrusion. It should be noted that the printability window for the mortar mixtures tested was: τ_y :100- 470 Pa; μ_p :13-58 Pa.s; and D_e at 120 kPa overhead pressure < $3x10^{-3}$ $s^{-0.5}$. These ranges are valid for the ram extrusion parameters of D_B=39 mm; D_N=9 mm; L_E=80 mm; V_R=2.5 mm/s used in this study (in Figure 4b) and can vary depending on the extrusion speed, dimensions and load capacity of the extruder used.

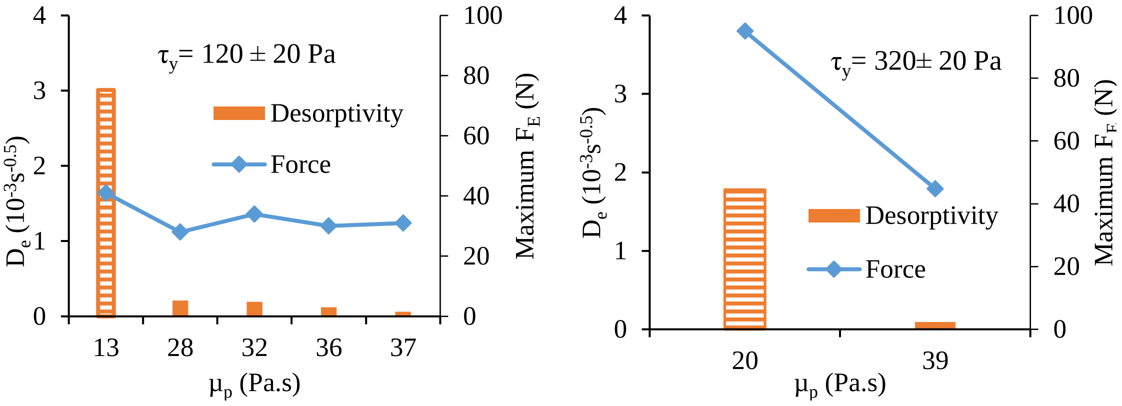

Figure 11. Relationship between material properties and extrudability of mortar with τ_y of 120 (left) and 320 Pa (right). Dashed bar indicates D_e of mixtures without WG.

3.4. STATISTICAL MODELING OF MATERIAL PROPERTIES AND EXTRUDABILITY

Multiple linear regression was used for modeling the maximum F_E as a function of τ_y, μ_p, and D_e. Considering the low number of 19 data points available (Table 5), the regression equation developed is used for explanatory modeling (i.e., for assessing the significance of the effect of τ_y, μ_p, and D_e on extrudability) and not for estimating the maximum F_E given the material properties.

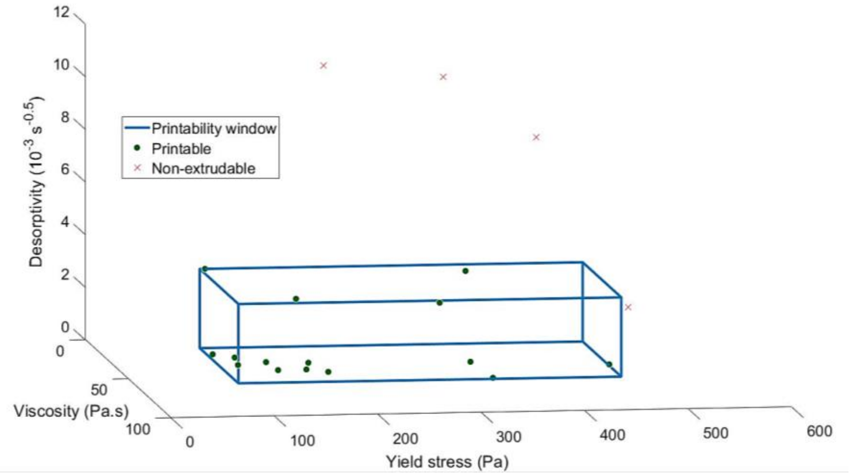

Figure 12. Printability window of mortar encompassing yield stress (100-470 Pa), plastic viscosity (10-60 Pa.s) and desorptivity (< 3x10^{-3} $s^{-0.5}$).

Table 6. Multiple regression analysis of extrudability results.

Property	**Maximum $F_E = f(\tau_y, \mu_p, \text{and } D_e)$**		**Maximum $F_E = f(\tau_y \text{ and } D_e)$**	
	Estimate	**p-value**	**Estimate**	**p-value**
τ_y (Pa)	0.13	0.0013	0.14	0.0002
μ_p (Pa.s)	0.48	0.3127*	--	--
D_e (10^{-3} $s^{-0.5}$)	15.39	0.0155	10.55	0.0029
Adjusted R^2	0.76		0.76	

* p-value>0.05 implies that the influence of a specific parameter is insignificant

The multiple regression model for the maximum F_E was initially fit using all the three measured material properties (i.e., τ_y, μ_p, and D_e). The adjusted R^2 values, estimates, along with the p-values of partial tests for τ_y, μ_p, and D_e are shown in Table 6. The p-values are lower than 0.05 for τ_y and D_e indicating that these properties have a significant effect on the maximum F_E. Conversely, the high p-value for μ_p indicates that it has no significant effect on the maximum F_E, given the values of τ_y and D_e. Therefore, a second regression model was fit using τ_y and D_e, and these results are also reported in Table 6. The p-values lower than 0.05 indicate that τ_y and D_e have a significant effect on extrudability. Additionally, the positive values of the estimates for both properties indicate that an increase in τ_y and D_e leads to higher F_E or lower level of extrudability.

4. CONCLUSIONS

In this study, the rheology and fluid filtration characteristics of mortar mixtures were varied by changing the w/c, SP dosage, and WG content. The influence of these properties on extrudability was evaluated. The fluid filtration was measured in terms of D_e, while the extrudability was assessed as the maximum F_E needed during ram extrusion. The rheology and fluid filtration properties of the material exhibited an opposing influence on extrudability indicating the importance of assessing these properties to characterize the extrusion-based 3DP. A printability window was proposed for the extrusion of mortar based on the rheology and fluid filtration characteristics. Additionally, regression analysis was carried out to evaluate the significance of the effect of material properties on extrudability. Based on the finding of this investigation, the following conclusions can be made:

1. For the ram extruder dimensions that was employed in this investigation with nozzle size of 9 mm and extrusion speed of 2.5 mm/s, the suitable ranges of material properties for successful extrusion-based 3DP consist of τ_y of 100- 470 Pa, μ_p of 10-60 Pa.s, and $D_e < 3\text{x}10^{-3}$ $s^{-0.5}$ at an overhead pressure of 120 kPa.
2. For the investigated rheological parameters and fluid filtration characteristics, the influence of μ_p on the extrudability is insignificant compared to that of τ_y and D_e.

The extrudability can be improved by reducing τ_y and D_e. However, a lower limit of 100 Pa for τ_y is needed to ensure shape stability of extrudable layers.

3. The decrease in w/c from 0.35 to 0.25 required increasing SP dosage from 0 to 0.09%, by mass of cement, to maintain an initial mini-slump flow of 120 mm. The decrease in w/c lead to 400% to 650% increase in μ_p at various time intervals and reduced the D_e by 80%. It also improved extrudability due to the change in the material flow behavior during extrusion from frictional plastic (at 0.35 w/c and no SP) to visco-plastic (at 0.25 w/c and 0.09% SP).
4. The increase in SP dosage from 0.09% to 0.43% increased the initial mini-slump flow by 200% and reduced τ_y and μ_p by over 90%. The influence of SP dosage on D_e varied depending on the overhead pressure in the forced bleeding cell and the SP dosage. The increase in SP from 0.09% to 0.11% resulted in improvement in extrudability due to the reduction in the material rheological properties. Mixtures with higher SP dosages (i.e., 0.22% and 0.43%) were not suitable for extrusion owing to the low τ_y and poor shape stability.
5. At fixed initial mini-slump flow of 170 mm, the addition of WG at 0.1%, 0.2%, and 0.3%, by mass of cement, significantly increased μ_p by up to 180%, while reducing the rate of increase in τ_y with time. The use of WG also drastically reduced the D_e by up to two orders of magnitude. The use of WG improved the extrudability due to low fluid filtration and the open time given the high SP demand. The use of WG also enabled the extrusion of print material with high τ_y (> 400 Pa) at lower F_E.

6. Overall, the use of WG enabled the development of print materials that are most suitable for extrusion-based 3DP (i.e., higher τ_y needed for shape stability, lower D_e needed to homogeneous extrusion, and increased open time if needed).

REFERENCES

[1] N. Hack, W.V. Lauer, Mesh-Mould: Robotically Fabricated Spatial Meshes as Reinforced Concrete Formwork, Architectural Design 84(3) (2014) 44-53.

[2] J. Zhang, J. Wang, S. Dong, X. Yu, B. Han, A Review of The Current Progress and Application of 3D Printed Concrete, Composites Part A: Applied Science and Manufacturing 125 (2019) 105533.

[3] J. Jagoda, B. Diggs-McGee, M. Kreiger, S. Schuldt, The Viability and Simplicity of 3D-Printed Construction: A Military Case Study, Infrastructures 5(4) (2020) 35.

[4] R.A. Buswell, W.R.L. da Silva, F.P. Bos, H.R. Schipper, D. Lowke, N. Hack, H. Kloft, V. Mechtcherine, T. Wangler, N. Roussel, A process classification framework for defining and describing Digital Fabrication with Concrete, Cement and Concrete Research 134 (2020) 106068.

[5] A. Bhardwaj, S.Z. Jones, N. Kalantar, Z. Pei, J. Vickers, T. Wangler, P. Zavattieri, N. Zou, Additive manufacturing processes for infrastructure construction: a review, International Manufacturing Science and Engineering Conference, American Society of Mechanical Engineers, 2019, p. V001T01A005.

[6] B. Khoshnevis, Automated Construction by Contour Crafting—Related Robotics and Information Technologies, Automation in Construction 13(1) (2004) 5-19.

[7] B. Khoshnevis, D. Hwang, K.-T. Yao, Z. Yeh, Mega-Scale Fabrication By Contour Crafting, International Journal of Industrial and Systems Engineering 1(3) (2006) 301-320.

[8] T.T. Le, S.A. Austin, S. Lim, R.A. Buswell, A.G. Gibb, T. Thorpe, Mix Design and Fresh Properties for High-Performance Printing Concrete, Materials and Structures 45(8) (2012) 1221-1232.

[9] K. Vallurupalli, N. Farzadnia, K.H. Khayat, Effect of flow behavior and process-induced variations on shape stability of 3D printed elements – A review, Cement and Concrete Composites 118 (2021) 103952.

[10] K.G. Kuder, S.P. Shah, Rheology of Extruded Cement-Based Materials, ACI Materials Journal 104(3) (2007) 283.

[11] X. Zhou, Z. Li, Characterization of Rheology of Fresh Fiber Reinforced Cementitious Composites Through Ram Extrusion, Materials and Structures 38(1) (2005) 17-24.

[12] R. Srinivasan, D. DeFord, S.P. Shah, The Use of Extrusion Rheometry in the Development of Extruded Fiber-Reinforced Cement Composites, Concrete Science and Engineering 1(1) (1999) 26-36.

[13] A. Perrot, D. Rangeard, Y. Mélinge, Prediction of the ram extrusion force of cement-based materials, Applied Rheology 24(5) (2014) 34-40.

[14] C. Ince, M.A. Carter, M.A. Wilson, N.C. Collier, A. El-Turki, R.J. Ball, G.C. Allen, Factors affecting the water retaining characteristics of lime and cement mortars in the freshly-mixed state, Materials and Structures 44(2) (2011) 509-516.

[15] A.V. Rahul, A. Sharma, M. Santhanam, A desorptivity-based approach for the assessment of phase separation during extrusion of cementitious materials, Cement and Concrete Composites 108 (2020) 103546.

[16] H. Alghamdi, S.A.O. Nair, N. Neithalath, Insights into Material Design, Extrusion Rheology, and Properties of 3D-Printable Alkali-Activated Fly Ash-Based Binders, Materials & Design 167 (2019) 107634.

[17] B. Panda, M.J. Tan, Experimental Study on Mix Proportion and Fresh Properties of Fly ash Based Geopolymer for 3D Concrete Printing, Ceramics International 44(9) (2018) 10258-10265.

[18] D.P. Bentz, S.Z. Jones, I.R. Bentz, M.A. Peltz, Towards the Formulation of Robust and Sustainable Cementitious Binders for 3-D Additive Construction By Extrusion, Construction and Building Materials 175 (2018) 215-224.

[19] H. Khelifi, A. Perrot, T. Lecompte, D. Rangeard, G. Ausias, Prediction of extrusion load and liquid phase filtration during ram extrusion of high solid volume fraction pastes, Powder Technology 249 (2013) 258-268.

[20] S.A.O. Nair, S. Panda, M. Santhanam, G. Sant, N. Neithalath, A critical examination of the influence of material characteristics and extruder geometry on 3D printing of cementitious binders, Cement and Concrete Composites 112 (2020) 103671.

[21] C.F. Ferraris, L.E. Brower, P. Banfill, D. Beaupré, F. Chapdelaine, F. de Larrard, P. Domone, Comparison of Concrete Rheometers: International Test at LCPC (Nantes, France) in October, 2000, US Department of Commerce, National Institute of Standards and Technology2001.

[22] K. El Cheikh, S. Rémond, N. Khalil, G. Aouad, Numerical and Experimental Studies of Aggregate Blocking in Mortar Extrusion, Construction and Building Materials 145 (2017) 452-463.

[23] D. Feys, J.E. Wallevik, A. Yahia, K.H. Khayat, O.H. Wallevik, Extension of the Reiner–Riwlin equation to determine modified Bingham parameters measured in coaxial cylinders rheometers, Materials and structures 46(1-2) (2013) 289-311.

[24] V. Nerella, M. Näther, A. Iqbal, M. Butler, V. Mechtcherine, Inline Quantification of Extrudability of Cementitious Materials for Digital Construction, Cement and Concrete Composites 95 (2019) 260-270.

[25] J.T. Kuchem, Development of Test Methods for Characterizing Extrudability of Cement-Based Materials for Use in 3D Printing Concrete, Missouri University of Science and Technology, 2019.

[26] A. Perrot, C. Lanos, Y. Melinge, P. Estellé, Mortar Physical Properties Evolution in Extrusion Flow, Rheologica Acta 46(8) (2007) 1065-1073.

[27] A. Perrot, D. Rangeard, V.N. Nerella, V. Mechtcherine, Extrusion of Cement-Based Materials-An Overview, RILEM Technical Letters 3 (2018) 91-97.

[28] L. Teng, J. Zhu, K.H. Khayat, J. Liu, Effect of welan gum and nanoclay on thixotropy of UHPC, Cement and Concrete Research 138 (2020) 106238.

[29] K. Khayat, A. Yahia, Effect of welan gum-high-range water reducer combinations on rheology of cement grout, Materials Journal 94(5) (1997) 365-372.

[30] F. Wang, D. Wang, Q. Wang, J. Yu, J. Shi, Impact of Welan Gum on Cement Paste Containing PCE Superplasticizers with Different Charge Densities, ChemistrySelect 4(5) (2019) 1722-1726.

[31] E. Üzer, J. Plank, Impact of welan gum stabilizer on the dispersing performance of polycarboxylate superplasticizers, Cement and Concrete Research 82 (2016) 100-106.

[32] O.H. Wallevik, J.E. Wallevik, Rheology as a tool in concrete science: The use of rheographs and workability boxes, Cement and concrete research 41(12) (2011) 1279-1288.

[33] Y.W.D. Tay, Y. Qian, M.J. Tan, Printability region for 3D concrete printing using slump and slump flow test, Composites Part B: Engineering 174 (2019) 106968.

[34] D.P. Bentz, M.A. Peltz, J. Winpigler, Early-age properties of cement-based materials. II: Influence of water-to-cement ratio, Journal of materials in civil engineering 21(9) (2009) 512-517.

[35] N.A. Libre, R. Khoshnazar, M. Shekarchi, Relationship between fluidity and stability of self-consolidating mortar incorporating chemical and mineral admixtures, Construction and Building Materials 24(7) (2010) 1262-1271.

[36] E. Sakai, T. Kasuga, T. Sugiyama, K. Asaga, M. Daimon, Influence of superplasticizers on the hydration of cement and the pore structure of hardened cement, Cement and concrete research 36(11) (2006) 2049-2053.

[37] A. Yahia, S. Mantellato, R. Flatt, Concrete rheology: a basis for understanding chemical admixtures, Science and Technology of Concrete Admixtures, Elsevier2016, pp. 97-127.

[38] D. Marchon, R. Flatt, Impact of chemical admixtures on cement hydration, Science and technology of concrete admixtures, Elsevier2016, pp. 279-304.

[39] G.H. Kirby, J.A. Lewis, Comb polymer architecture effects on the rheological property evolution of concentrated cement suspensions, Journal of the American Ceramic Society 87(9) (2004) 1643-1652.

[40] R.A. Basterfield, C.J. Lawrence, M.J. Adams, On the interpretation of orifice extrusion data for viscoplastic materials, Chemical Engineering Science 60(10) (2005) 2599-2607.

[41] A. Perrot, Y. Mélinge, D. Rangeard, F. Micaelli, P. Estellé, C. Lanos, Use of ram extruder as a combined rheo-tribometer to study the behaviour of high yield stress fluids at low strain rate, Rheologica Acta 51(8) (2012) 743-754.

[42] Y. Vanhove, K.H. Khayat, Forced Bleeding Test to Assess Stability of Flowable Concrete, ACI Materials Journal 113(6).

[43] K.H. Khayat, M. Saric-Coric, Effect of Welan Gum SuperplasticizerCombinations on Properties of Cement Grouts, ACI Symposium Publication 195.

[44] K.H. Khayat, Z. Guizani, Use of Viscosity-Modifying Admixture to Enhance Stability of Fluid Concrete, ACI Materials Journal 94(4).

[45] J. Desbrieres, Cement cake properties in static filtration. On the role of fluid loss control additives on the cake porosity, Cement and concrete research 23(6) (1993) 1431-1442.

[46] C. Brumaud, H. Bessaies-Bey, C. Mohler, R. Baumann, M. Schmitz, M. Radler, N. Roussel, Cellulose ethers and water retention, Cement and Concrete Research 53 (2013) 176-184.

[47] N. Roussel, Rheological Requirements for Printable Concretes, Cement and Concrete Research (2018).

III. EFFECT OF SHRINKAGE MITIGATING MATERIALS ON PRINTABILITY AND SHRINKAGE RESISTANCE OF 3D PRINTABLE MORTAR

Kavya Vallurupalli and Kamal H. Khayat*

Department of Civil, Architectural and Environmental Engineering, Missouri University of Science and Technology, Rolla, Missouri, USA

ABSTRACT

The 3D printed layers in the fresh state are exposed to the environment due to the lack of formwork. The typically low water-to-binder ratio of print material also results in a low amount of bleed water and consequently higher evaporation of pore water and shrinkage at an early age. Such high susceptibility of printed layers to drying can have a detrimental effect on the interlayer adhesion and induce shrinkage cracking that can adversely affect the performance of printed elements. For the conventional casting process, shrinkage resistance of concrete can be improved by using expansive agents (EA), shrinkage reducing admixtures (SRA), and internal curing agents (lightweight sand (LWS) and superabsorbent polymers (SAP)). However, the suitability of these shrinkage mitigating materials for 3D printing depends on their influence on material printability (extrudability and shape stability). In this study, the effect of CaO-based EA, SRA, LWS, and SAP, as well as the influence of water retaining effect of welan gum (WG) on printability, plastic shrinkage (measured in terms of mass loss in plastic state), autogenous shrinkage, drying shrinkage, and compressive strength of print material are evaluated.

Keywords**:** Compressive strength, Printability, Shrinkage mitigating materials, Shrinkage resistance.

1. INTRODUCTION

3D printing (3DP) of cement-based materials involves extrusion of print material layer-by-layer onto a working surface, thus building elements without formwork. Unlike the traditional design approach for construction, 3DP offers several advantages including higher productivity, reduced labor cost, architectural freedom, topology optimization, more efficient use of resources leading to greater sustainability, and improved automation and safety during construction [1-4]. Due to these advantages, there has been a growing interest in recent years to utilize 3D printing (3DP) of cement-based materials process in concrete construction [5-7]. Efforts to date have focused on formulation of cement-based materials to meet the rheological requirements for printability [8-12] with little emphasis on the drying and shrinkage-related challenges linked to the nature 3DP process. The printable cement-based materials are often formulated to have low water-to-binder ratio (w/b) (< 0.4) to meet the rheology, water retentivity [13] and shape stability requirements during extrusion and layering stages of 3DP process [14, 15]. Additionally, relatively smaller aggregates (typically maximum aggregate size (MAS) < 4.8 mm) and lower aggregate contents (typically <50% by total volume) are used to avoid blockage at the nozzle entry during extrusion [10, 16-19]. The relatively low w/b and high binder content of print material can increase the risk of early-age shrinkage cracking [20]. The lack of coarse aggregate, the high surface-to-volume ratio of the printed layers, and the absence of formwork also increase the susceptibility of the printed element to drying [21]. Drying of printed layers in plastic state can hinder hydration, ultimately impairing the strength of the printed elements [22]. The drying of layers during printing can result in poor adhesion between the layers leading to high porosity at the interface [23, 24]. The differential shrinkage deformation in the layers can result in residual stresses in the printed elements resulting in poor interlayer bond and cracking [11]. The increased porosity at the interface as a result of drying and shrinkage cracking can increase the possibility of ingress of various deleterious substances into printed elements consequently shortening the design life of the structure. Therefore, it is crucial to evaluate the shrinkage behavior of 3D printable materials.

In the 3DP literature, limited studies investigated the shrinkage behavior of the printable materials. Le et al. [25] studied the drying shrinkage of 3D printable fiber-reinforced mortars and investigated the influence of external environmental conditions (relative humidity (RH) varied between 100%-60%). The decrease in RH resulted in increase in the shrinkage strain by 400% at 100 days. However, the shrinkage samples were not printed, but conventionally-cast. Zhang et al. [26] evaluated the change in dimensions of a printed element in the hardened state by measuring the change in length of saw-cut printed prisms measuring 100x100x400 mm^3 exposed to a constant temperature of 20 ± 2 ^{0}C and RH of 50% ± 5%. Identical shrinkage strains of 800 microns were reported at 56 days for the printed mortar samples with sand-to-cement ratios of 1 and 1.2. In both these studies the shrinkage samples were moist cured under standard condition for the first 24 hours before exposure to the drying environmental conditions. However, during the 3DP process, the printed layers are immediately exposed to the environment due to the lack formwork and so the contribution of the shrinkage in the plastic state can be significant to the total shrinkage strain and hardened properties of the print material. Ketel et al. [27] evaluated the shrinkage of printed 25 mm cubes of a clay-based mixture with water contents between 51% and 56% by volume. The shrinkage was measured by scanning the surface using a 3D laser scanner. The dimensions of the printed element in the scanned image were measured shortly after printing to 7 days to evaluate the dimensional stability of the printed elements over time. At 7 days, a 35% to 55% reduction in volume was observed for cubes with water contents of 51% and 56%, respectively. The higher reduction in volume at higher water content was attributed to the presence of more evaporable water, and lower effective stiffness of the element to resist the stresses that develop during drying. Federowicz et al. [28] also evaluated shrinkage deformation of printed layers of dimensions 1350x35x15 mm^3 using laser measurement sensors from immediately after printing to up to 7 days. The unsealed and foil-sealed test specimens were kept in an environmental chamber at 20℃ and 50% RH. The unsealed specimens showed 385% higher 7-d total shrinkage strain (autogenous and drying) compared to the foil-sealed specimens. Federowicz et al. [28] also evaluated the effectiveness of shrinkage reducing admixture (SRA) at controlling the shrinkage of unsealed printed elements and observed around 23% reduction in the total shrinkage when using SRA at dosage of 4% by mass of cement. Despite the limited work done on assessment of shrinkage of 3D printed elements, the above results suggest that the water transport behavior, water retention capacity, and exposure conditions play a significant role on shrinkage resistance and the use of shrinkage mitigating materials such as SRA be beneficial for 3DP process where the option of external moist curing can limit the printing of subsequent layers during continuous printing [28]. In addition to SRA, other shrinkage mitigating materials such as expansive agents (EA) and internal curing agents (lightweight sand (LWS) and superabsorbent polymers (SAP)) are often used to improve the shrinkage resistance of conventionally cast concrete. The influence of these shrinkage mitigating materials on the printability (extrudability and shape stability) as well as the shrinkage and mechanical performance of print material need to be evaluated before adapting the use of the shrinkage mitigating materials for extrusion-based 3DP.

This article presents the results of tests and analyses related to the influence of incorporating CaO-based EA, SRA, LWS, and SAP on printability, plastic shrinkage (measured in terms of mass loss in plastic state), autogenous shrinkage, drying shrinkage, and compressive strength of printable mortar mixtures. In addition to the shrinkage mitigating materials, the influence of welan gum (WG) on printability, shrinkage performance and compressive strength of the mortar mixtures was investigated. The use of WG can improve the water retention capacity of the mortar mixtures which typically enables printing of cement-based materials with high τ_y [13]. The improvement in the water retentivity can alter the amount of water available for evaporation during drying of the printed layers in the plastic and consequently can have an effect on the mass loss and shrinkage of print material in the plastic state [29].

2. MATERIALS AND EXPERIMENTAL PROCEDURES

2.1. MATERIALS AND MIXTURE PROPORTIONS

To investigate the effect of shrinkage mitigating materials and WG on the printability and performance of the print material, seven different mortar mixtures were prepared. The mortar mixtures were prepared using Type I/II Portland cement conforming to ASTM C 150. The sand with nominal maximum aggregate size of 2 mm was used and its content was set at 40% by volume of mortar. The size and content of the sand were selected to minimize the risk of aggregate blockage in the extruder [19]. The specific gravity and absorption values of the sand were 2.58% and 2.24%, respectively. The water to powder ratio of mortar mixtures was set at 0.32 for all mixtures. A polycarboxylate-based SP with 23% solid mass content and 1.05 specific gravity was used to maintain an initial mini-slump values of 25±13 mm (measured immediately after mixing). This initial mini slump value was selected to ensure shape stability of printed mortar filaments when extruded using 9 mm nozzle [13].

The shrinkage mitigating materials and WG were incorporated at the following dosages: EA – 0 and 5% by weight of powder (cement and EA); LWS – 0, 12%, and 25% by volume of fine aggregate; SRA – 0 and 2% by mass of cement; SAP – 0 and 0.3% by mass of cement; and WG – 0 and 0.6% by mass of cement. The chemical composition and physical properties of cement and EA are shown in Table 1. For mixtures containing LWS, pre-saturated LWS (soaked for 72 h) with maximum aggregate size of 2 mm was used. The specific gravity, absorption, and desorption (at 94% RH) values of LWS were 1.65, 32.8%, and 70.3%, respectively. Liquid-based SRA with specific gravity of 1.01

and solid content of 30% by mass was also used for shrinkage mitigation. Angular covalently cross-linked acrylic-co-acrylamide sodium polymer (poly-AA-co-AM) of mean particle sizes 850 μm and 35 μm of were used as larger SAP (SAPL) and smaller SAP (SAPS), respectively. The particle size distributions of the SAPL and SAPS were measured using a laser particle size analyzer under a solvent of ethyl alcohol (purity > 99.7%) and these results are shown in Figure 1. A polysaccharide-based soluble WG powder with a specific gravity of 0.8 was also used to modify the water retentivity of mortar mixtures.

The mixture proportions of the investigated mortar mixtures are shown in Table 2. The mortar mixtures were prepared using a 12-L capacity mixer. The mixing procedure of the mortars involved: 1) dry mixing of sand and cement at 1 rps for 2 min; 2) gradual addition of water along with SP to the dry materials and mixing at 2 rps for 3 min; 3) resting the material for 1 min followed by final mixing at 2 rps for 3 min. For mixtures with shrinkage mitigating materials, EA and pre-soaked LWS were added along with the cement and sand in Step 1, SRA was added along with the mix water in Step 2, while SAPs were added in dry condition in Step 1. In the case of mixtures with WG, the WG was pre-mixed with water+SP for 3 min using a blender and was added to the dry materials in step 2 of the mixing process.

2.2. EXPERIMENTAL PROCEDURE

2.2.1. SAP Absorption (Tea Bag Method). The rate of absorption of filtered pore solution by SAPL and SAPS was assessed in filtrated pore solution using the tea bag method [30-33]. The filtrated pore solution was prepared from paste mixture made with water to cement ratio of 6.

During the absorption test, the container with the pore solution was covered using an elastic stretch film to avoid carbonation and evaporation. Dry SAP sample of approximately 0.2 gm was added to an empty tea bag and was placed in 500 ml pore solution. The sample was immersed in the pore solution for 10s, 20s, 30s, 1 min, 5 min, 10 min, 30 min, 60 min, 2h, 4h, and 8 h. After each time, the tea bag was removed from the pore solution and was gently wiped on a dry cloth for approximately 10 s to remove the surplus and weakly bound liquid and weighed. The absorption capacity of the SAPs at each time were assessed using Eq. 6.

$$\mathrm{AC} = \frac{\mathrm{m_3 - m_2 - m_1 - m_0}}{\mathrm{m_2}} \qquad \text{Eq. 6}$$

where m_0 mass of water absorbed by a tea bag (empty), m_1 is the mass of the dry tea bag, m_2 is the mass of the dry SAPs, and m_3 is the mass of the teabag with SAP after a specific immersion time. For each SAP, the absorption was measured for ten samples and the average absorption values at each immersion time were reported.

Table 1. Chemical composition and physical properties of powder constituents.

Binder constituents	Cement	EA
SiO_2, %	19.0	12.6
Al_2O_3, %	3.9	5.7
Fe_2O_3, %	3.5	1.9
CaO, %	68.3	82.6
MgO, %	1.7	0.1
SO_3, %	2.4	-
Na_2O eq., %	0.6	0.9
$CaCO_3$, %	3.3	-
Blaine surface area, m^2/kg	390	-
Specific gravity	3.14	3.12
LOI, %	1.5	-

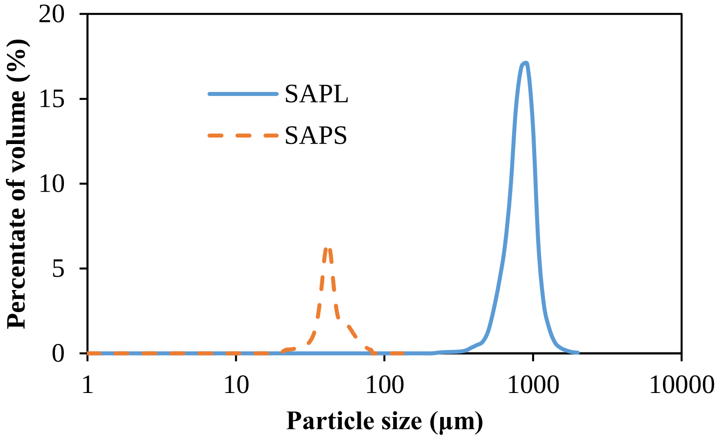

Figure 1. Particle size distributions of SAPs.

Table 2. Mixture proportions of investigated mixtures.

Mixture[*]	**Cement (kg/m^3)**	**Water (kg/m^3)**	**Sand (kg/m^3)**	**SP demand (kg/m^3)**	**Additive (kg/m^3)**
REF	941	301	1032	-	-
5EA12LWS	894	301	901	-	47 (EA) and 83 (LWS)
5EA25LWS	894	301	774	-	47 (EA) and 165 (LWS)
0.3SAPL0.17SP	941	301	1032	1.6	2.8 (SAPL)
0.3SAPS0.22SP	941	301	1032	2.1	3 (SAPS)
2SRA	941	301	1032	-	19 (SRA)
0.6WG0.45SP	941	301	1032	4.2	5.6 (WG)

[*] 0.3SAPL0.17SP indicates SAPL content and SP dosage of 0.3% and 0.17%, by mass of cement, respectively.

2.2.2. Rheology. The rheological properties of the mortar mixtures were measured using a coaxial rheometer with inner radius of 50 mm and outer radius of 60 mm. The rheological measurements were made on mortar samples 30 min after water addition. The test sample was pre-sheared at 0.7 rps for 25 s and stepwise drop in the shear rate from 0.7 to 0.025 rps was carried out in 10 steps with each shear rate applied for 5 s. The average value of torque at each shear rate was recorded, and the yield stress (τ_y) and plastic viscosity (μ_p) values were estimated using the Reiner-Riwlin equations for the Bingham model [34]. The τ_y and μ_p values were used to estimate the Bingham number (B_N) using Eq. 7 [8]. The V_R and D_B refer to the extrusion speed and extruder barrel diameter, respectively.

$$B_N = \frac{\tau_y D_B}{8\mu_p V_R} \quad \text{Eq. 7}$$

2.2.3. Fluid Filtration. The fluid filtration test was used to assess the rate of forced bleeding of the material under a given pressure gradient and it was measured in terms of desorptivity (D_e) [13, 35]. Approximately 30 min after water addition, 750 gm of mortar sample was placed in a filtration test cylinder fitted with a metal screen and filter paper of pore size 2 µm. The overhead pressure of 120 kPa (± 10 kPa) was applied on the test sample for 5 min using CO_2 gas. The bleed water filtered out of the sample due to the pressure application was collected using a 10 ml graduated cylinder. The D_e was estimated by plotting the relative amount of filtrated water to the square root of time. Two samples were tested for each mortar mixture and the average values of D_e are reported.

2.2.4. Ram Extrusion. The extrudability of mortar mixtures was evaluated using a ram extruder setup with a load limit of 135 N, D_B of 39 mm, and nozzle diameter of 9 mm. Approximately 30 min after water addition, 330 gm of mortar sample was placed in the extruder and the V_R was set at 2.5 mm/s. The maximum force (max F_E) needed to extrude the test sample was measured and was used as an indicator for extrudability.

2.2.5. Plastic Shrinkage (Mass Loss). The shrinkage of mortar mixtures in plastic state when exposed to evaporation rate of 1.6 $kg/m^2 \cdot h$ was assessed by measuring the mass loss of the test samples. The evaporation rate was achieved by adjusting the fan speed while maintaining the temperature and RH at 40 ± 3 °C and 20% ± 5 %, respectively. Immediately after mixing, the mortar samples were prepared by filling the lubricated cylindrical molds with diameter of 63 mm and height of 25 mm. The filling of the mold was done in two layers and rodding each layer 25 times with a tamping rod. The mold was carefully lifted vertically, and the sample was exposed to the drying environment. The mass loss of the test samples was measured every hour in the first 12 h and after every 24 h for the next 6 days. For each mixture, the mass loss was measured for two samples and the average values are reported.

2.2.6. Autogenous Shrinkage. The autogenous shrinkage of mortar mixtures was assessed as per ASTM C1698 using corrugated tube molds. The shrinkage measurement started from the final setting time using a Vicat test. For each mixture, three tubes were tested, and the average strain values are reported.

2.2.7. Drying Shrinkage. The prismatic samples of 25x25x300 mm were cast to evaluate drying shrinkage. The samples were cured under a wet burlap until the final setting time and were exposed to evaporation rate of 1.6 $kg/m^2 \cdot h$. Length changes were measured for over 56 d since the day of casting. After demolding, the length and mass of the sample was measured, and this was used as the initial length and mass for the estimating the shrinkage strain and mass loss, respectively. The measurements were taken for three samples for each mixture, and the average strain and mass loss values are reported.

2.2.8. Compressive Strength. For each mixture, 50 mm mortar cubes were cast, and the samples were either subjected to drying environment (evaporation rate of 1.6 $kg/m^2 \cdot h$) or to the lime-saturated curing until the day of testing i.e., 1 or 7 d. For lime-saturated cured samples, the samples after casting were covered with burlap, demolded after the final setting time, and were then transferred to the curing tanks. For each mixture, curing conditions, and curing duration, three cubes were tested, and the average compressive strength values are reported.

2.2.9. Hydration Kinetics. The hydration kinetics of the mortar mixtures was monitored using an isothermal calorimeter. Approximately 70 gm of sample was placed in the calorimeter and the test temperature was maintained at a constant temperature of 20 ± 0.1 °C. The samples were placed in the calorimeter immediately after mixing, and the data were collected up to 48 hours.

3. RESULTS AND DISCUSSIONS

3.1. INFLUENCE OF SHRINKAGE MITIGATING MATERIALS AND WG ON PRINTABILITY

The rheological properties, B_N (estimated using Eq. 7), D_e, and max F_E of the investigated mixtures measured 40 ± 5 min after water addition are shown in Table 3. With the incorporation of 5% EA and 12% or 25% LWS, no SP was required to maintain the initial slump value of 25 ± 13 mm. The use of 5% EA and increase in LWS content from 0% to 12% and 25% reduced the τ_y by 13% and 23% and consequently lowered B_N from 92 to 61 and 80, respectively. The use of 5% EA and 12% LWS increased D_e from $4.2x10^{-3}$ $s^{-0.5}$ to 5.1 $x10^{-3}$ $s^{-0.5}$ and showed no significant effect on the maximum F_E. However, the increase of LWS content to 25% increased the D_e to 6.1 $x10^{-3}$ $s^{-0.5}$ and this may have led to significant fluid filtration during the extrusion process and blockage in the extruder i.e., the extrusion force exceeded the load cell limit of 135 N. Due to the poor printability of the mortar mixture with 5% EA and 25% LWS, only mortar mixture containing 12% LWS was used for further investigation.

Table 3. Material properties and maximum extrusion of investigated mixtures.

Mixture	τ_y (Pa)	μ_p (Pa.s)	B_N	D_e (10^{-3} $s^{-0.5}$)	Maximum F_E (N)
REF	463	10	92	4.2	30
5EA12LWS	403	13	61	5.1	31
5EA25LWS	357	9	80	6.1	>135
0.3SAPL0.17SP	339	73	9	0.9	87
0.3SAPS0.22SP	189	3	113	0.8	76
2SRA	400	19	42	4.5	30
0.6WG0.45SP	422	137	6	0.5	84

The absorption kinetic of SAPL and SAPS in filtered pore solution is shown in Figure 2. Rapid intake of filtered pore solution was observed for smaller and larger SAP particles during the first 10 and 100 min, respectively, followed by desorption. SAPL had slower rate of water absorption and slightly higher total absorption compared to SAPS. At a given time, different rates of absorption and desorption for different sized of SAP could results in difference in the amount of freely available water in the mortar mixtures containing SAPS and SAPL. Such difference in the free water can result in different workability and rheological properties [31, 36] leading to difference in printability of the mortar mixtures.

The relatively higher water absorption of SAPS resulted in higher SP demand of 0.22% for mortar mixture containing SAPS compared to SAPL mixture which required 0.17% SP to ensure initial mini slump of 25+13 mm. However, the earlier desorption of water by SAPS lead to an increase in the material flowability at later time. This resulted in 44% and 96% lower values of τ_y and μ_p for SAPS mortar mixture compared to SAPL when measured 40 min after water addition. Furthermore, a drastic drop in the D_e values from $4.2x10^{-3}$ to $0.9x10^{-3}$ and $0.8x10^{-3}$ $s^{-0.5}$ was observed with the use of SAPL and SAPS, respectively. This can be attributed to the high gel strength of cross-linked SAP used in the current study. The gel strength refers to the ability to retain the absorbed water and gel shape under the application of pressure [37, 38]. The low values of D_e for SAP-based mortar mixtures suggest low fluid filtration during extrusion. Additionally, B_N value greater than 100 for SAPS mortar mixture suggest plastic flow behavior during extrusion. The plastic flow behavior implies low contribution of viscosity to the extrusion force. Such behavior can be beneficial for 3DP as low extrusion force will be needed during printing [8]. However, the absorption-desorption kinetics need to be finetuned to ensure that the shape stability of the printed layers is maintained.

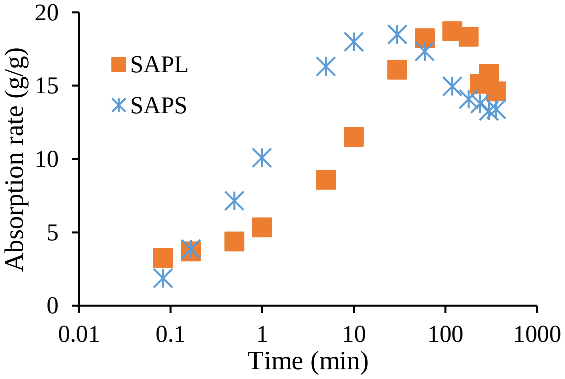

Figure 2. Absorption kinetics of SAPL and SAPS in filtered pore solution.

The addition of 2% SRA required no addition of SP to maintain initial slump and showed no significant on the De and extrudability of mortar mixtures. However, the addition of SRA reduced the τ_y and increased the μ_p by 13% and 90%, respectively. The increment in μ_p can be attributed to the increase in viscosity of the pore solution with the addition of SRA. Bentz [39] observed up to 55% increase in viscosity with the addition 10% SRA to distilled water.

On the other hand, the use of 0.6% WG necessitated adding 0.45% SP to maintain the initial mini slump of 25+13 mm. The combined addition of WG and SP showed no significant effect on τ_y but resulted in significant increase in μ_p from 10 Pa.s to 137 Pa.s and decrease in D_e from 4.2 x10^{-3} to 0.5 x10^{-3}. Such increase in the μ_p and D_e can be attributed to reduction in free water available for filtration and increase in the pore solution viscosity. The decreased D_e can also be due to aggregating of long-chain polymers of WG that fill the pores in the mortar during fluid filtration and the decreased permeability of mortar due to increased dispersion of cement particles in the presence of SP. The increase in μ_p with use of WG also resulted in change in the B_N from 92 to 6. These changes in the B_N suggest increased contribution of μ_p to the extrusion force i.e., higher μ_p of WG mixture contributed to increased max F_E from 30 N (for REF mixture) to 84 N.

3.2. MASS LOSS IN PLASTIC STATE

The mass loss results of the mortar mixtures during the first 1.2 h and 24 h are shown in Figure 3a and Figure 3b, respectively. Lura et al. [40] noted that during the initial period of drying (< 1 h) the solid particles settle due to gravity, the bleed water gets transported to the specimen surface, and the evaporation occurs mainly from the bleed water. In Figure 3a, the rate of mass loss is identical for all mortar mixtures independent of the additive except for mixture with SAPS. The high mass loss for SAPS mixture can be attributed to the higher amount of free water available due desorption of SAPS [36] as well as the 0.22% SP dosage [41] used to maintain the initial slump. The increase in the amount of free water available implies more water is available for bleeding and evaporation. Furthermore, the loss of water due to evaporation can increase the ionic concentration of pore solution which can further accelerate desorption rate of SAP making more water available for evaporation [42, 43].

For mortar mixture with SRA, a deviation in the evaporation rate i.e., reduction to lower rate can be observed at around 0.8 h. Such deviation occurs once the bleed water is consumed by evaporation and the rate at which bleed water forms can no longer compensate for the water lost due to evaporation. This results in the formation of menisci, and this exerted capillary tensile stresses in the pore system. These tensile stress causes the shrinkage of the test sample and consequently brings the pore solution to the surface. In other words, higher the tensile stress exerted, more amount of fluid is drawn to the surface for evaporation. The capillary tensile stress exerted is proportional to the surface tension of the pore solution [44, 45]. For mortar mixture with SRA, the use of SRA reduces the surface tension of pore solution [40, 46], and this results in the reduction in the capillary pressure exerted consequently lowering the amount of pore solution drawn to the surface for evaporation. Furthermore, Bentz et al. [46, 47] hypothesized that the initial drying of pore solution leads to increased concentration of SRA near the specimen surface which then prevents the pulling of pore solution with higher surface tension from deeper part of the sample to the surface. This explains the deviation from faster rate of mass loss at 0.8 h (in Figure 3a) and 25% lower mass loss for SRA mixture sample at 24 h (in Figure 3b).

In Figure 3b, a 25% reduction in mass loss was observed after 24 h for mortar mixture containing 0.3% SAPL. The use of 0.6%WG was also effective at reducing 24 h mass loss by 17%. This improvement with the use of SAPL and WG could also be attributed to decreased amount of free water. The absorption of pore water by SAPL and relatively slow desorption during the hardening process of mortar mixture reduces the free water available for evaporation [36].The long-chain polymers of WG can reduce the free water available by adhering to the water molecules and entrapped them between the adjacent polymer chains of WG [29, 48]. The improved water retention capacity of SAPL and WG [29] under the application of pressure is also evident from the low D_e values ($<1x10^{-3}$ $s^{-0.5}$) observed during fluid filtration test when an overhead pressure of 120 kPa was applied. The lack of such improvement for SAPS mixture despite the low D_e can be attributed to faster desorption rate of SAPS and extended dormant period (in Figure 6) with the use 0.22% SP. During the dormant period, the mortar sample possesses poor tensile strength is highly vulnerable to the capillary tensile stress and concrete is highly vulnerable to tensile stresses which results increased bleeding of water and evaporation rate [49]. The use of 5%EA+12%LWS showed no significant improvement in terms of mass loss.

3.3. AUTOGENOUS SHRINKAGE

The autogenous shrinkage results of the investigated mixtures are shown in Figure 4. The use of EA and LWS resulted in significant expansion of 100 µstrain and no shrinkage strain was observed during the 28-d of testing. This could be due to the combined effect of expansion caused by hydration of EA [50] and continuous and uniform internal moist curing provided by the LWS that could mitigate self-desiccation [20, 51]. Furthermore, the high porosity of LWS means that the chemical shrinkage takes place in the larger pores of LWS before the shrinkage occurs in the fine pores in paste and can reduce the capillary tensile stress exerted on the pore system [20] The lack of shrinkage and expansion strain of was also observed for SAPL-based mixture due to the internal moist curing provided by SAPL. The lack such improvement for SAPS-based mixture could be due to the agglomeration of SAPS and its poor distribution leading to ineffective internal moist curing [52]. The reduced surface tension with the addition of 2% SRA also resulted in slight improvement in the shrinkage strain. However, the improvement in autogenous shrinkage was limited compared to that of mass loss in plastic state (in Figure 3) as well as the drying shrinkage (in Figure 5). Such limited effect on autogenous shrinkage could be due to the absorption of the SRA in the pore solution by the hydration products [46]. Whereas for plastic and drying shrinkage, the samples are exposed drying environment after final setting, which could hinder the hydration product formation and thereby reduce the absorption of SRA by the hydration products. The high shrinkage for WG mixtures can be partly attributed to the SP dosage used to meet the initial slump requirement [53, 54].

3.4. DRYING SHRINKAGE

The drying shrinkage strain results of the investigated mixtures are shown in Figure 5. The 28-d shrinkage strain was lowest for mixture with SRA (31% lower than REF) followed by the mixture containing EA and LWS (21% lower than REF). While the use of SAPL was effective at mitigating autogenous shrinkage, the drying shrinkage strain was similar to that of REF and SAPS mixtures, indicating no significant effect of SAP addition on drying shrinkage.

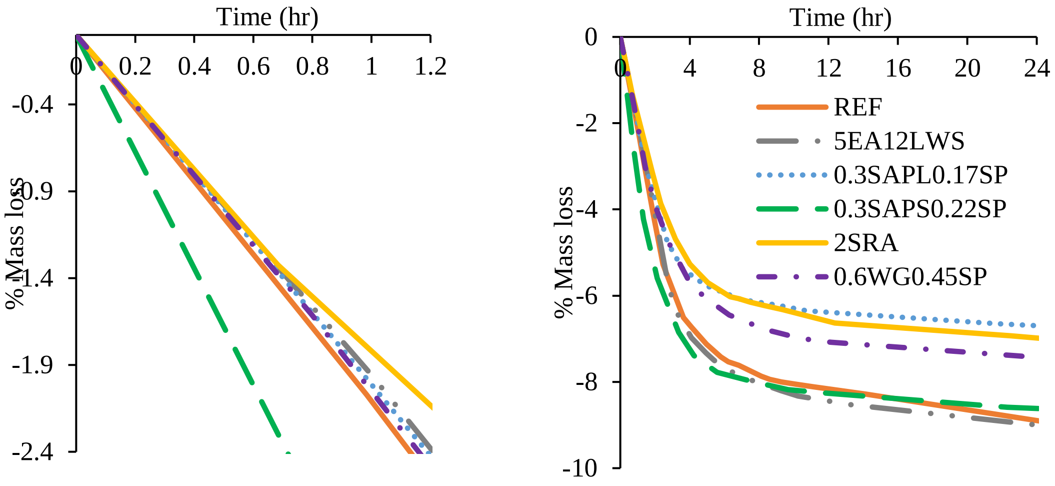

Figure 3. Mass loss in plastic state during first 1.2 h (left) and 24 h (right) when exposed to evaporation rate of 1.6 kg/m^2·h.

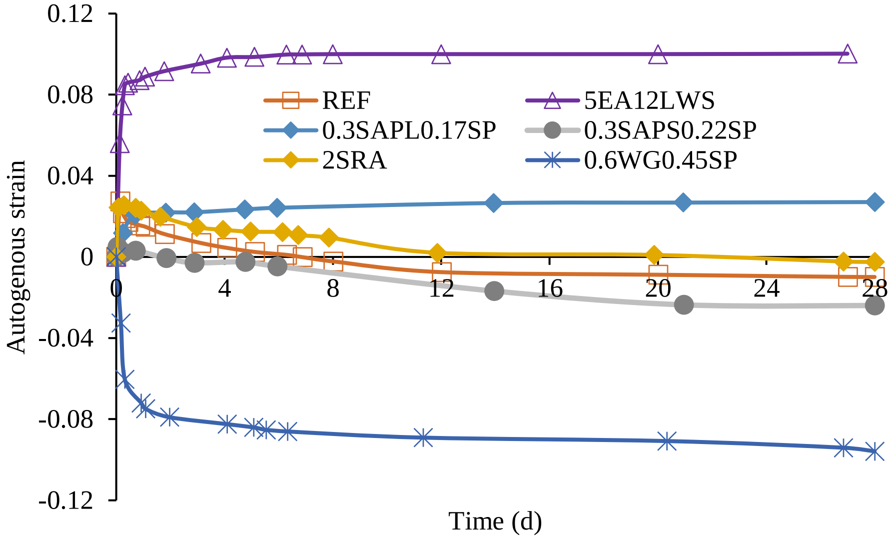

Figure 4. Autogenous shrinkage results of investigated mortar mixtures.

These results suggest that the effectiveness of SAP to lower shrinkage is reduced when the external curing is limited. A similar observation was made by [43] for mortar mixtures with SAP are exposed to different curing temperatures of 10 °C to 40 °C and RH conditions of 40% to 80%. The addition of 0.6% WG combined with 0.45% SP resulted in 28% higher strain at 28 d compared to REF mixture. The relatively high strain for SAP-based and WG-based mixtures can be partly attributed to the SP used. Qian et al. noted that the increased shrinkage strain with the use of SP is due to the decrease in the pore size distribution with the use of SP [55]. Furthermore, higher entrapped air can be expected during the casting of specimens for WG- based mixture due to the high viscosity. This can contribute to increased porosity of the samples and consequently higher shrinkage [56].

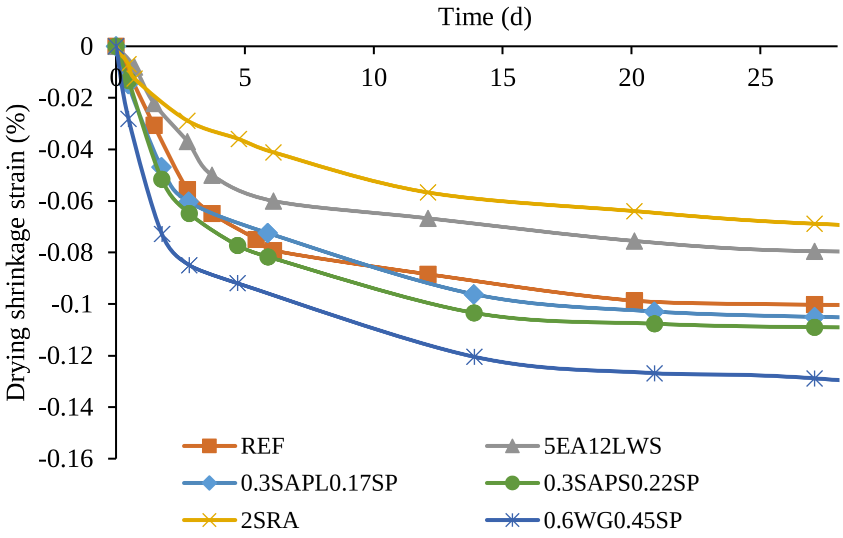

Figure 5. Effect of shrinkage mitigating materials and WG on drying shrinkage when sample are exposed to evaporation rate of 1.6 kg/m^2·h.

3.5. COMPRESSIVE STRENGTH

The 1- and 7-d compressive strength results of the mixtures with shrinkage mitigating materials and WG relative to the REF mixture subjected to drying and lime-saturated moist curing are presented in Figure 6. The mixture with EA and LWS, their combined use resulted in a slight improvement (up to 5%) in the compressive strength at 1 and 7 d for samples exposed to drying since casting. These results can be attributed to the counterbalanced effect of the increased porosity of mortars due to LWS and internal moist curing provided by LWS during the drying of mortar samples [57, 58]. However, for 1 and 7 d lime cured samples, an 8% to 12% drop in compressive strength was observed. The internal curing provided by LWS is less effective for moisture cured samples and the observed reduction can be attributed to the increased porosity. For SAP-based mixtures, while the internal curing provided by 0.3% SAPL was effective at mitigating shrinkage, a 16% and 18% reduction in the compressive strength at 1- and 7-d, respectively. Such reduction in the compressive strength with SAPL addition could be due to the counterbalanced effect of the increased porosity of mortars due to desorption of SAPL [59] and reduced internal cracking of mortar due to internal moist curing provided by SAPL during the drying of mortar samples [60]. The reduction in the compressive strength was significantly reduced when the mortar samples are subjected to moist curing.

With the addition of 2% SRA, a significant reduction in compressive strength was observed. This can be attributed the fact that the use of SRA reduced the cement hydration, especially at early-age (as evident from the heat of hydration in Figure 7). This can be attributed the fact that the SRA can adsorb onto the cement particles to inhibit the dissolution of cement particles and the nucleation sites of hydration products [61, 62]. For samples subjected to lime-saturated curing, 59% and 33% reduction in the strength was observed with the use of SRA for 1- and 7-d samples, respectively. The % reduction is reduced when the samples are exposed to drying environments i.e., 44% and 23% reduction in the strength was observed with the use of SRA for 1- and 7-d samples, respectively. For mixtures with WG, when the samples are subjected to drying environments, 33% and 32% reduction in the strength was observed for 1- and 7-d samples, respectively. The extent of reduction is reduced when the samples are cured in lime-saturated water i.e., 5% and 16% reduction in the strength was observed with the use of WG for 1- and 7-d samples, respectively.

3.6. EARLY-AGE HYDRATION

The rate of heat flow and total heat flow results of the mixtures are shown in Figure 7. The results indicate that the use of EA and LWS reduced the dormant period by 37% and this can be attributed to the hydration of EA [63]. For mixtures with SAPL, SAPS, and WG, the incorporation of SP to maintain the initial slump resulted in the increased dormant period and delay in the hydration peak. This can be attributed to increase in the activation energy needed for nucleation and growth of hydrates in the presence of SP [64]. Whereas for SRA-based mixture, the increased dormant period and delay in the hydration peak can attributed the fact that the SRA can adsorb onto the cement particles to inhibit the dissolution of cement particles and the nucleation sites of hydration products [61, 62]. The use of SRA also resulted in the 20% reduction in 48-h total heat flow. The increase in the peak heat flow and a slight improvement in the 48-h total heat flow was observed for mixtures with SP compared to REF and this can be attributed to the increased dispersion cement particles in the presence of SP [64, 65].

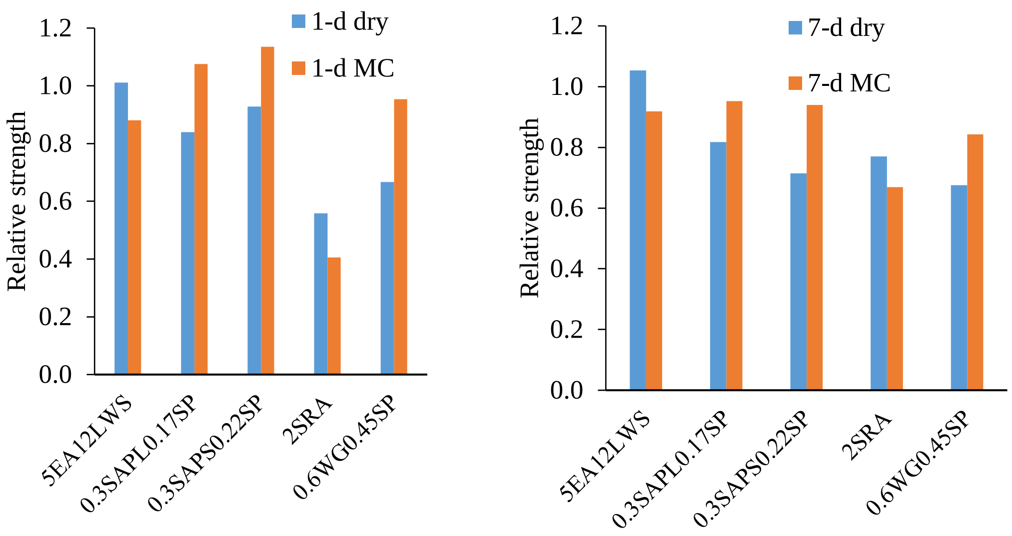

Figure 6. 1-d (left) and 7-d (right) compressive strength results of mortar mixtures relative to the strength of REF mixture subjected to identical curing conditions.

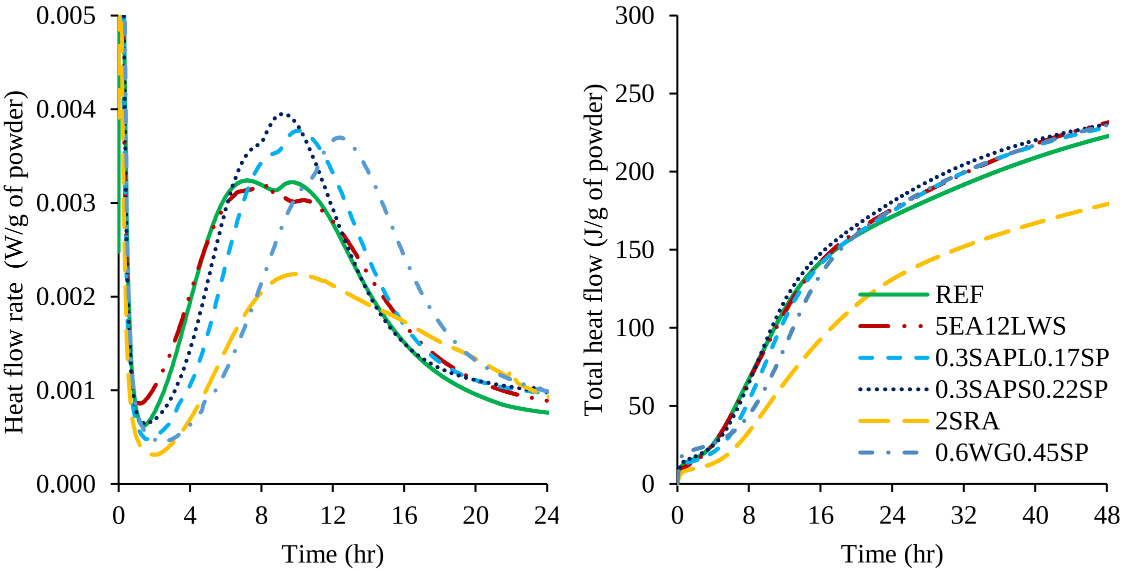

Figure 7. Rate of heat (left) and total heat flow (right) results of investigated mixtures.

4. CONCLUSIONS

In this study, the effect of CaO-based EA, SRA, pre-saturated LWS, and SAP on printability, plastic shrinkage, autogenous shrinkage, drying shrinkage, and compressive strength of print material are evaluated. SAPs of particles sized 850 µm (SAPL) and 35µm (SAPS) are used and their influence on the absorption-desorption kinetics and its influence on the material properties is examined. The printability of the mixtures was evaluated using a ram extrusion setup as well as by assessing the rheological properties and desorptivity. The plastic and drying shrinkage of the samples was evaluated by subjecting them to the drying i.e., evaporation rate of 1.6 kg/m^2·h. The plastic shrinkage was assessed in terms of the mass loss of the test samples when exposed drying. The influence of the curing condition (lime-saturated moist curing vs. drying) and time on the compressive strength of the mixtures was also evaluated. The drying condition was selected to accelerate the drying process and to simulate the conditions during 3DP process, where the printed elements are exposed to the environment in the plastic state and the conventional moist curing is limited. Based on the above results, the following conclusions are warranted:

1. The use of 25% pre-saturated LWS along 5% EA led to significant fluid filtration during the ram extrusion and consequently causing the blockage with the extruder. The reduction of LWS content to 12% improved the extrudability significantly and reduced the D_e from 6.1 to 5.1x10^{-3} s$^{-0.5}$. The use of 5% EA + 12% LWS had no significant effect on mass loss of mortar samples in plastic state, but showed autogenous expansion and lowered drying shrinkage strain by

21% measured after 28 d. The improvement in autogenous and drying shrinkage was due to the combined action of expansive stress caused by the hydration EA and uniform internal moist curing provided by LWS. The use of LWS was also effective at maintaining the compressive strength of mortar mixtures when exposed to drying.

2. Relatively faster absorption within the first 10 min followed by desorption was observed for SAPS particles compared to SAPL. This resulted in difference in the amount of freely available water for the two SAP-based mixtures and lower values of τ_y by 44%and μ_p by 96% for SAPS mixture compared to SAPL when measured 40 min after water addition. The changes in the absorption-desorption kinetics resulted in plastic and visco-plastic flow behaviors during extrusion for SAPS and SAPL-based mixtures, respectively. The fast desorption of SAPS led to increased rate of mass loss of plastic samples during the first 1 h. The internal moist curing provided by SAPL resulted in 25% reduction in 24-h mass loss of samples in plastic state and 370% reduction in the 28-d autogenous shrinkage. No beneficial effect of SAPL was observed on 28-d drying shrinkage, 1- and 7-compressive strength due to the exposed drying conditions. The use of SAPL and SAPS is effective at reducing the D_e and consequently enabling printing shape stable elements. However, the absorption-desorption kinetics needs to be tailored to ensure improvement in the plastic shrinkage resistance.
3. The internal curing provided by 0.3% SAPL was effective at mitigating plastic and autogenous shrinkage while the internal curing provided by 12% LWS was effective at reducing the autogenous and drying shrinkage while improving

compressive strength. The synergetic effect of these internal curing agents on improving the plastic, autogenous, and drying shrinkage needs to be further explored.

4. The addition of 2% SRA had no significant effect on the printability and improved the 24-hr mass loss resistance, and 28-d drying shrinkage strain by 21% and 31%, respectively, and showed less effectiveness at improving the autogenous shrinkage. The use of SRA also had a detrimental effect on compressive strength, hydration kinetics, and total degree of hydration. These results suggest that combining the use of SRA with EA+LWS can result in development of shrinkage-resistant 3d printable mortar mixtures with acceptable compressive strength performance.
5. The use of 0.6% WG reduced the D_e from $4.2x10^{-3}$ to $0.5\ x10^{-3}\ s^{-0.5}$ and lowered the B_N from 92 to 6. The improved water retention contributed to 17% reduction in the mass loss of the plastic shrinkage samples. The use of WG increased 28-d drying shrinkage strain by 28% and delayed the hydration kinetics owing to the high SP demand.

REFERENCES

[1] H. Kloft, H.-W. Krauss, N. Hack, E. Herrmann, S. Neudecker, P.A. Varady, D. Lowke, Influence of Process Parameters on the Interlayer Bond Strength of Concrete Elements Additive Manufactured by Shotcrete 3d Printing (Sc3dp), Cement and Concrete Research 134 (2020) 106078.

[2] I. Agustí-Juan, F. Müller, N. Hack, T. Wangler, G. Habert, Potential Benefits of Digital Fabrication for Complex Structures: Environmental Assessment of a Robotically Fabricated Concrete Wall, Journal of Cleaner Production 154 (2017) 330-340.

[3] J. Zhang, J. Wang, S. Dong, X. Yu, B. Han, A Review of the Current Progress and Application of 3d Printed Concrete, Composites Part A: Applied Science and Manufacturing 125 (2019) 105533.

[4] M. Moini, J. Olek, J.P. Youngblood, B. Magee, P.D. Zavattieri, Additive Manufacturing and Performance of Architectured Cement-Based Materials, Advanced Materials 30(43) (2018) 1802123.

[5] M.S. Khan, F. Sanchez, H. Zhou, 3-D Printing of Concrete: Beyond Horizons, Cement and Concrete Research 133 (2020) 106070.

[6] D.D. Camacho, P. Clayton, W.J. O'Brien, C. Seepersad, M. Juenger, R. Ferron, S. Salamone, Applications of Additive Manufacturing in the Construction Industry–a Forward-Looking Review, Automation in construction 89 (2018) 110-119.

[7] R.A. Buswell, W.R. Leal de Silva, S.Z. Jones, J. Dirrenberger, 3d Printing Using Concrete Extrusion: A Roadmap for Research, Cement and Concrete Research 112 (2018) 37-49.

[8] K. Vallurupalli, N. Farzadnia, K.H. Khayat, Effect of Flow Behavior and Process-Induced Variations on Shape Stability of 3d Printed Elements – a Review, Cement and Concrete Composites 118 (2021) 103952.

[9] T.T. Le, S.A. Austin, S. Lim, R.A. Buswell, A.G. Gibb, T. Thorpe, Mix Design and Fresh Properties for High-Performance Printing Concrete, Materials and structures 45(8) (2012) 1221-1232.

[10] S.C. Paul, Y.W.D. Tay, B. Panda, M.J. Tan, Fresh and Hardened Properties of 3d Printable Cementitious Materials for Building and Construction, Archives of Civil and Mechanical Engineering 18(1) (2018) 311-319.

[11] M.K. Mohan, A. Rahul, K. Van Tittelboom, G. De Schutter, Extrusion-Based Concrete 3d Printing from a Material Perspective: A State-of-the-Art Review, Cement and Concrete Composites (2020) 103855.

[12] D.G. Soltan, V.C. Li, A Self-Reinforced Cementitious Composite for Building-Scale 3d Printing, Cement and Concrete Composites 90 (2018) 1-13.

[13] K. Vallurupalli, N.A. Libre, K. Khayat, Characterization of Print Material Extrudability Using Rheology and Desorptivity, ACI materials journal (2022 (Submitted)).

[14] G. Ma, L. Wang, Y. Ju, State-of-the-Art of 3d Printing Technology of Cementitious Material—an Emerging Technique for Construction, Science China Technological Sciences (2017) 1-21.

[15] V.N. Nerella, S. Hempel, V. Mechtcherine, Effects of Layer-Interface Properties on Mechanical Performance of Concrete Elements Produced by Extrusion-Based 3d-Printing, Construction and Building Materials 205 (2019) 586-601.

[16] D. Asprone, F. Auricchio, C. Menna, V. Mercuri, 3d Printing of Reinforced Concrete Elements: Technology and Design Approach, Construction and Building Materials 165 (2018) 218-231.

[17] Z. Malaeb, H. Hachem, A. Tourbah, T. Maalouf, N. Zarwi, F. Hamzeh, 3d Concrete Printing: Machine and Mix Design, International Journal of Civil Engineering 6(6) (2015) 14-22.

[18] S. Al-Qutaifi, A. Nazari, A. Bagheri, Mechanical Properties of Layered Geopolymer Structures Applicable in Concrete 3d-Printing, Construction and Building Materials 176 (2018) 690-699.

[19] K. El Cheikh, S. Rémond, N. Khalil, G. Aouad, Numerical and Experimental Studies of Aggregate Blocking in Mortar Extrusion, Construction and Building Materials 145 (2017) 452-463.

[20] D.P. Bentz, O.M. Jensen, Mitigation Strategies for Autogenous Shrinkage Cracking, Cement and Concrete Composites 26(6) (2004) 677-685.

[21] P. Aıtcin, The Durability Characteristics of High Performance Concrete: A Review, Cement and Concrete Composites 25(4-5) (2003) 409-420.

[22] S. Ma, S. Kawashima, Rheological and Water Transport Properties of Cement Pastes Modified with Diutan Gum and Attapulgite/Palygorskite Nanoclays for 3d Concrete Printing, RILEM International Conference on Concrete and Digital Fabrication, Springer, 2018, pp. 61-69.

[23] J.G. Sanjayan, B. Nematollahi, M. Xia, T. Marchment, Effect of Surface Moisture on Inter-Layer Strength of 3d Printed Concrete, Construction and Building Materials 172 (2018) 468-475.

[24] J. Van Der Putten, G. De Schutter, K. Van Tittelboom, The Effect of Print Parameters on the (Micro) Structure of 3d Printed Cementitious Materials, RILEM International Conference on Concrete and Digital Fabrication, Springer, 2018, pp. 234-244.

[25] T.T. Le, S.A. Austin, S. Lim, R.A. Buswell, R. Law, A.G. Gibb, T. Thorpe, Hardened Properties of High-Performance Printing Concrete, Cement and Concrete Research 42(3) (2012) 558-566.

[26] Y. Zhang, Y. Zhang, W. She, L. Yang, G. Liu, Y. Yang, Rheological and Harden Properties of the High-Thixotropy 3d Printing Concrete, Construction and Building Materials 201 (2019) 278-285.

[27] S. Ketel, G. Falzone, B. Wang, N. Washburn, G. Sant, A Printability Index for Linking Slurry Rheology to the Geometrical Attributes of 3d-Printed Components, Cement and Concrete Composites (2018).

[28] K. Federowicz, M. Kaszyńska, A. Zieliński, M. Hoffmann, Effect of Curing Methods on Shrinkage Development in 3d-Printed Concrete, Materials 13(11) (2020) 2590.

[29] F. Wang, D. Wang, Q. Wang, J. Yu, J. Shi, Impact of Welan Gum on Cement Paste Containing Pce Superplasticizers with Different Charge Densities, ChemistrySelect 4(5) (2019) 1722-1726.

[30] V. Mechtcherine, D. Snoeck, C. Schröfl, N. De Belie, A.J. Klemm, K. Ichimiya, J. Moon, M. Wyrzykowski, P. Lura, N. Toropovs, Testing Superabsorbent Polymer (Sap) Sorption Properties Prior to Implementation in Concrete: Results of a Rilem Round-Robin Test, Materials and structures 51(1) (2018) 1-16.

[31] V. Mechtcherine, E. Secrieru, C. Schröfl, Effect of Superabsorbent Polymers (Saps) on Rheological Properties of Fresh Cement-Based Mortars — Development of Yield Stress and Plastic Viscosity over Time, Cement and Concrete Research 67 (2015) 52-65.

[32] D. Snoeck, C. Schröfl, V. Mechtcherine, Recommendation of Rilem Tc 260-Rsc: Testing Sorption by Superabsorbent Polymers (Sap) Prior to Implementation in Cement-Based Materials, Materials and structures 51(5) (2018) 1-7.

[33] X. Ma, Q. Yuan, J. Liu, C. Shi, Effect of Water Absorption of Sap on the Rheological Properties of Cement-Based Materials with Ultra-Low W/B Ratio, Construction and Building Materials 195 (2019) 66-74.

[34] D. Feys, J.E. Wallevik, A. Yahia, K.H. Khayat, O.H. Wallevik, Extension of the Reiner–Riwlin Equation to Determine Modified Bingham Parameters Measured in Coaxial Cylinders Rheometers, Materials and structures 46(1-2) (2013) 289-311.

[35] A.V. Rahul, A. Sharma, M. Santhanam, A Desorptivity-Based Approach for the Assessment of Phase Separation During Extrusion of Cementitious Materials, Cement and Concrete Composites 108 (2020) 103546.

[36] V. Mechtcherine, M. Wyrzykowski, C. Schröfl, D. Snoeck, P. Lura, N. De Belie, A. Mignon, S. Van Vlierberghe, A.J. Klemm, F.C. Almeida, Application of Super Absorbent Polymers (Sap) in Concrete Construction—Update of Rilem State-of-the-Art Report, Materials and structures 54(2) (2021) 1-20.

[37] Y.R. Kwon, S.H. Lim, H.C. Kim, J.S. Kim, Y.W. Chang, J. Choi, D.H. Kim, Superabsorbent Polymer with Improved Permeability and Absorption Rate Using Hollow Glass Microspheres, Journal of Polymer Science 59(5) (2021) 462-470.

[38] M.J.A.D. Zohourian Mehr, K. Kabiri, Superabsorbant Polymer Materials: A Review, Iranian Polymer Journal 17(6) (2008) -.

[39] D.P. Bentz, Influence of Shrinkage-Reducing Admixtures on Early-Age Properties of Cement Pastes, Journal of Advanced Concrete Technology 4(3) (2006) 423-429.

[40] P. Lura, B. Pease, G.B. Mazzotta, F. Rajabipour, J. Weiss, Influence of Shrinkage-Reducing Admixtures on Development of Plastic Shrinkage Cracks, ACI materials journal 104(2) (2007) 187-194.

[41] E. Sakai, T. Kasuga, T. Sugiyama, K. Asaga, M. Daimon, Influence of Superplasticizers on the Hydration of Cement and the Pore Structure of Hardened Cement, Cement and Concrete Research 36(11) (2006) 2049-2053.

[42] O.M. Jensen, P.F. Hansen, Water-Entrained Cement-Based Materials: I. Principles and Theoretical Background, Cement and Concrete Research 31(4) (2001) 647-654.

[43] A. Soliman, M. Nehdi, Effect of Drying Conditions on Autogenous Shrinkage in Ultra-High Performance Concrete at Early-Age, Materials and structures 44(5) (2011) 879-899.

[44] M.D. Cohen, J. Olek, W.L. Dolch, Mechanism of Plastic Shrinkage Cracking in Portland Cement and Portland Cement-Silica Fume Paste and Mortar, Cement and Concrete Research 20(1) (1990) 103-119.

[45] F.H. Wittmann, On the Action of Capillary Pressure in Fresh Concrete, Cement and Concrete Research 6(1) (1976) 49-56.

[46] D.P. Bentz, M.R. Geiker, K.K. Hansen, Shrinkage-Reducing Admixtures and Early-Age Desiccation in Cement Pastes and Mortars, Cement and Concrete Research 31(7) (2001) 1075-1085.

[47] D.P. Bentz, Curing with Shrinkage-Reducing Admixtures, Concrete International 27(10) (2005) 55-60.

[48] E. Üzer, J. Plank, Impact of Welan Gum Stabilizer on the Dispersing Performance of Polycarboxylate Superplasticizers, Cement and Concrete Research 82 (2016) 100-106.

[49] F. Sayahi, M. Emborg, H. Hedlund, A. Cwirzen, Plastic Shrinkage Cracking of Self-Compacting Concrete: Influence of Capillary Pressure and Dormant Period, Nordic Concrete Research 60(1) (2019) 67-88.

[50] H. Zhao, H. Liu, Y. Wan, R. Maria Ghantous, J. Li, Y. Liu, Y. Ni, J. Guan, Mechanical Properties and Autogenous Deformation Behavior of Early-Age Concrete Containing Pre-Wetted Ceramsite and Cao-Based Expansive Agent, Construction and Building Materials 267 (2021) 120992.

[51] S. Weber, H.W. Reinhardt, A New Generation of High Performance Concrete: Concrete with Autogenous Curing, Advanced Cement Based Materials 6(2) (1997) 59-68.

[52] P. Lura, F. Durand, O.M. Jensen, Autogenous Strain of Cement Pastes with Superabsorbent Polymers, International RILEM conference on volume changes of hardening concrete: testing and mitigation, RILEM Publications SARL Paris, France, 2006, pp. 57-65.

[53] E. Holt, Contribution of Mixture Design to Chemical and Autogenous Shrinkage of Concrete at Early Ages, Cement and Concrete Research 35(3) (2005) 464-472.

[54] L. Wu, N. Farzadnia, C. Shi, Z. Zhang, H. Wang, Autogenous Shrinkage of High Performance Concrete: A Review, Construction and Building Materials 149 (2017) 62-75.

[55] X. Qian, C. Yu, L. Zhang, K. Qian, M. Fang, J. Lai, Influence of Superplasticizer Type and Dosage on Early-Age Drying Shrinkage of Cement Paste with Consideration of Pore Size Distribution and Water Loss, Journal of Wuhan University of Technology-Mater. Sci. Ed. 35(4) (2020) 758-767.

[56] P.K. Mehta, P.J. Monteiro, Concrete Microstructure, Properties and Materials, 2017.

[57] Y. Zhao, B. Xu, J. Chang, Addition of Pre-Wetted Lightweight Aggregate and Steel/Polypropylene Fibers in High-Performance Concrete to Mitigate Autogenous Shrinkage, Structural Concrete 21(3) (2020) 1134-1143.

[58] M. Li, J. Liu, Q. Tian, Y. Wang, W. Xu, Efficacy of Internal Curing Combined with Expansive Agent in Mitigating Shrinkage Deformation of Concrete under Variable Temperature Condition, Construction and Building Materials 145 (2017) 354-360.

[59] L. Dudziak, V. Mechtcherine, Reducing the Cracking Potential of Ultra-High Performance Concrete by Using Super Absorbent Polymers (Sap), Proceedings of the International Conference on Advanced Concrete Materials (ACM'09), 2009, pp. 11-19.

[60] J. Justs, M. Wyrzykowski, F. Winnefeld, D. Bajare, P. Lura, Influence of Superabsorbent Polymers on Hydration of Cement Pastes with Low Water-to-Binder Ratio, Journal of Thermal Analysis and Calorimetry 115(1) (2014) 425-432.

[61] S. Zuo, Q. Yuan, T. Huang, M. Zhang, Q. Wu, Rheological Behaviour of Low-Heat Portland Cement Paste with Mgo-Based Expansive Agent and Shrinkage Reducing Admixture, Construction and Building Materials 304 (2021) 124583.

[62] J. Cheung, A. Jeknavorian, L. Roberts, D. Silva, Impact of Admixtures on the Hydration Kinetics of Portland Cement, Cement and Concrete Research 41(12) (2011) 1289-1309.

[63] T. Hua, J. Tang, J. Zhu, H. Tang, J. Liu, Evolution of the Early Compressive Strength of Cement-Slag Pastes with Cao-Based Expansive Agent, Materials and structures 55(2) (2022) 63.

[64] F. Ridi, L. Dei, E. Fratini, S.-H. Chen, P. Baglioni, Hydration Kinetics of Tri-Calcium Silicate in the Presence of Superplasticizers, The Journal of Physical Chemistry B 107(4) (2003) 1056-1061.

[65] K. Vallurupalli, W. Meng, J. Liu, K.H. Khayat, Effect of Graphene Oxide on Rheology, Hydration and Strength Development of Cement Paste, Construction and Building Materials 265 (2020) 120311.

IV. EFFECT OF SHRINKAGE MITIGATING MATERIALS ON CHLORIDE-INDUCED CORROSION RESISTANCE OF FIBER-REINFORCED CONCRETE

Kavya Vallurupalli[a], Nima Farzadnia[b], Kamal H. Khayat[a,]*

[a] Department of Civil, Architectural and Environmental Engineering, Missouri University of Science and Technology, Rolla, Missouri, USA

[b] Department of Civil and Environmental Engineering, University of Tennessee, Knoxville, Tennessee, USA

*Corresponding author

ABSTRACT

This paper investigates the effect of steel and synthetic fibers, expansive agent (EA), lightweight sand (LWS) on rebar corrosion, transport properties, and mechanical properties. Moist curing of 1 and 7 d followed by air drying for 90 d before exposure to chlorides was used. This was adopted to assess impact of limited moist curing and subsequent shrinkage on performance. Test results indicated that initial macro-cell current (I_{in}), time to crack initiation (T_{onset}), and time for cracks to propagate to the surface (T_{spike}) increased with the conductivity, modulus of rupture and transport properties, and flexural toughness, respectively. Using steel fibers, EA, and LWS reduced drying shrinkage, increased toughness but had detrimental effect on transport properties leading to higher I_{in} and lower T_{onset}. Synthetic fibers were less effective at improving shrinkage resistance, toughness, and delaying T_{spike}; however, such fibers had no detrimental effect on transport properties, I_{in} and T_{onset}.

Keywords**:** Corrosion; Cracking; Fiber-reinforced concrete; Shrinkage mitigation; Transport properties.

1. INTRODUCTION

The concrete can undergo shrinkage due to the external drying environment or due to self-desiccation. Under restrained conditions, the shrinkage can result in the cracking of concrete. The formation of cracks can provide a pathway for the ingress of detrimental agents such as chlorides, consequently accelerating the rebar corrosion process and decreasing the durability of the concrete structure [1-3]. As a result, the reduction of shrinkage and its associated cracking plays an important role in the design of concrete infrastructures. This has led to the development of various shrinkage mitigating materials [4-7] such as expansive agent (EA) and lightweight sand (LWS). The EA provides an early-age expansion to compensate for the subsequent shrinkage of concrete [8-10]. For LWS, the shrinkage mitigating mechanism is mainly by providing internal curing, thereby compensating for the water lost during drying or due to hydration [11-16]. Additionally, fibers are used to reduce the cracking potential of concrete due to shrinkage [17-21]. However, the influence of these materials on the long-term performance of concrete, such as chloride-induced corrosion, has not been investigated in the literature.

The underlying mechanism of shrinkage mitigation in concrete varies depending on the type of shrinkage mitigating material used. In the case of EAs, CaO-based, CSA-based, and MgO-based are commonly used for shrinkage mitigation in concrete [22, 23].

This paper studies the effect of CaO-based EA (referred to as EA from hereinafter), which produces CH platelet crystals during hydration [22]. The oversaturation of CH crystals results in crystallization pressure, leading to a significant expansion in concrete at the early ages. This expansion compensates for the subsequent contraction in concrete due to shrinkage [24, 25]. The expansion reaction necessitates access to water, and the amount of water available for hydration of EA (mixing water and water provided through curing) can significantly affect the degree of expansion [26-28].

The pre-saturated LWS provides extra moisture for the hydration of cementitious materials and reduces shrinkage at early ages. Pre- saturated LWS also ensures saturation of the capillary pores during the drying of hardened concrete, thereby reducing the drying shrinkage and its associated cracking [29-31]. Additionally, for concrete mixtures with EA, pre- saturated LWS can provide the amount of water needed for hydration of EA [6, 7]. Valipour and Khayat [6] observed a 14% and 44% reduction in 91-d shrinkage for 7-d moist cured concrete with the addition of 60% LWS (by mass of sand) and 8% EA (by mass of binder), respectively. However, the combined use of 60% LWS and 8% EA resulted in a further reduction in shrinkage by 56%.

In the case of fiber-reinforced concrete (FRC), the fibers can offer internal restraint to shrinkage. Additionally, the transfer of shrinkage stress from matrix to fibers and the crack bridging effect of fibers restrict the formation and growth of the cracks [32, 33]. The effectiveness of fibers depends on their type, modulus of elasticity, geometry, aspect ratio, and content [33, 34]. An improvement in the shrinkage resistance was reported by [4, 20, 35], with the combined use of fibers and EA. Corinaldesi et al. [20] noted an absence of expansion (during moist curing) and low shrinkage (during drying) for concrete consisting of both EA and steel fibers (by volume of concrete) at dosages of 3% and 1%, respectively. The lack of expansion was attributed to the swelling action of EA being counteracted by the restraining action of steel fibers. He et al. [36] reported that the restraining action of fibers on the expansion resulted in improved adhesion between the fibers and the surrounding matrix, leading to increased resistance to shrinkage, delay in occurrence, and growth of cracks in concrete. For concrete slabs exposed to drying within 24 h after casting, Pan et al. [4] also observed a significant decrease in the number of cracks from 4 to 0 with the addition of 0.6% polypropylene fibers to concrete with 8% EA. Cao et al. [35] noted a reduction in shrinkage cracking area from 1390 to 395 mm^2 for concrete slabs using both LWS and polypropylene fibers at dosages of 20% and 0.5%, respectively. A further decrease in the cracking area (by 26%) was observed with the addition of 8% EA to concrete with LWS and fibers. Such decrease was attributed to the combined action of the following mechanisms: a) increased degree of hydration of cementitious materials as well as hydration of EA with the presence of LWS; b) the saturation of capillary pores during the drying process by LWS; and c) the additional restraint and delay in the initiation and growth of shrinkage cracking provided by fibers.

Based on the above-reviewed literature, the individual and combined use of shrinkage mitigating materials and fibers improve shrinkage resistance and its associated cracking. This means that concrete with EA, LWS, and fibers would be less susceptible to shrinkage cracking, which would mean a reduction in the ingress of detrimental agents such as chlorides that could cause corrosion of embedded rebars. However, various researchers have noted a negative influence of the EA, LWS, and fibers on the transport properties of concrete, independent of their effect on the shrinkage and its associated cracking. For example, Shi et al. [1, 37] observed that the use of 7.5% CSA-based EA can ensure the shrinkage compensation (by 47%) but can lead to an increase in the rate of rebar corrosion upon exposure to chlorides and an increase in the transport properties of concrete mixtures such as air permeability (by 8%), capillary absorption (by 130%), and chloride diffusion (by 13%). Such an increase in the concrete transport properties can be attributed to the excessive expansion of EA that can damage the concrete microstructure [38]. Fan et al. [39] noted an increase in the corrosion current density of rebar embedded in concrete with LWS and steel fibers . The increase in current density was attributed to increased concrete porosity with LWS and higher concrete conductivity with steel fibers. Toutanji [40] observed up to 130% increase in the chloride permeability for concrete with the increase polypropylene fibers dosage from 0.1% to 0.5%. This was attributed to the decrease in concrete workability with the increase in fibers dosage and consequent increase in entrapped air during sample preparation. These results suggest that while EA, LWS, and fibers can improve the shrinkage resistance of concrete, their beneficial effect on the transport properties and long-term performance is not guaranteed.

The current study aims to investigate the effect of shrinkage mitigating materials (EA and LWS), fiber type (steel and synthetic), and cover depth (25, 38, and 50 mm) on chloride-induced rebar corrosion and its associated cracking of concrete. Reinforced concrete samples were subjected to limited moist curing of 1 or 7 d followed by air drying for 90 d before exposure to NaCl solution. Such curing conditions were adopted to assess the impact of limited moist curing conditions and drying shrinkage on the rebar corrosion resistance and cracking time of concrete cover due to rebar corrosion. An electrical connection was made between the rebars (anode) and a stainless-steel mesh (cathode), and the current between the cathode and the anode was monitored for 230 d. The corrosion indicators (i.e., initial current, time corresponding to onset of increase in current due to crack initiation, and time corresponding to sudden spike in current due to concrete surface cracking) were used to compare the corrosion resistance of various samples. In addition to corrosion testing, drying shrinkage, transport properties (i.e., water absorption and bulk resistivity), and mechanical properties (i.e., compressive strength and flexural properties) of concrete samples subjected to the same curing conditions were evaluated. The relationships between the measured corrosion indicators and key concrete properties, such as the transport and mechanical properties was investigated.

2. MATERIALS AND EXPERIMENTAL PROCEDURES

2.1. MATERIALS AND MIXTURE PROPORTIONS

To investigate the effect of shrinkage mitigating materials, fibers, and moist curing duration on the chloride-induced corrosion, six different concrete mixtures were prepared with 0 and 5% of EA, by weight of powder (binder and EA), 0 and 25% of LWS, by volume of fine aggregate, and 0 and 0.5% of fibers, by volume of concrete. The binder material included a Type I/II ordinary portland cement, Class C fly ash, and slag cement with binder replacement values of 45%, 35%, and 20%, by mass. This binder composition was selected to minimize shrinkage of FRC for bridge construction [41]. The dosage of CaO-based EA was determined based on an investigation carried out on concrete equivalent mortars by Mehdipour [5]. The chemical composition and physical properties of binder constituents and EA are shown in Table 1.

Two limestone-based coarse aggregates (CA) with maximum nominal aggregate size (MSA) of 12.5 and 25 mm and a river sand as fine aggregate with MSA 4.75 mm were used. This proportion was selected to optimize the particle packing density of the aggregate based on studies conducted by the authors [42]. A LWS with MSA of 6.3 mm and pre-saturated for 72 h was used. The particle size distribution and key physical properties of the aggregates are shown in Figure 1 and Table 2, respectively.

Micro and macro steel fibers and a synthetic finer composed by a blend of polypropylene and polyethylene fibers were used. The dimensions and physical properties of the fibers are shown in Table 3. A polycarboxylate-based high range water reducing admixture (HRWRA) with 23% solid mass content and 1.05 specific gravity was used to maintain the initial slump within the range of 150 ± 20 mm.

The proportions of the concrete mixtures are shown in Table 4. The REF mixture refers to the concrete made without any fiber, EA, and LWS. The STST+EA+LWS mixture refers to the concrete made with 0.5% steel fibers (80% macro and 20% micro steel fibers), 5% EA, and 25% LWS. The water-to-powder ratio (w/p) and powder content were fixed at 0.40 and 350 kg/m^3, respectively. The EA is considered as part of the powder material. In the FRC mixtures, the aggregate contents were adjusted according to the methodology proposed by Khayat et al. [43] to maintain constant mortar thickness over the coarse aggregate and fiber.

Table 1. Chemical composition and physical properties of powder constituents.

Binder constituents	**Cement**	**Fly ash**	**Slag**	**EA**
SiO_2, %	19.0	40.4	36.2	12.6
Al_2O_3, %	3.9	19.8	7.7	5.7
Fe_2O_3, %	3.5	6.3	0.7	1.9
CaO, %	68.3	24.4	44.2	82.6
MgO, %	1.7	3.5	7.6	0.1
SO_3, %	2.4	1.0	1.7	-
Na_2O eq., %	0.6	1.3	0.52	0.9
$CaCO_3$, %	3.3	-	-	-
Blaine surface area, m^2/kg	390	490	530	-
Specific gravity	3.14	2.71	2.86	3.12
LOI, %	1.5	-	-	-

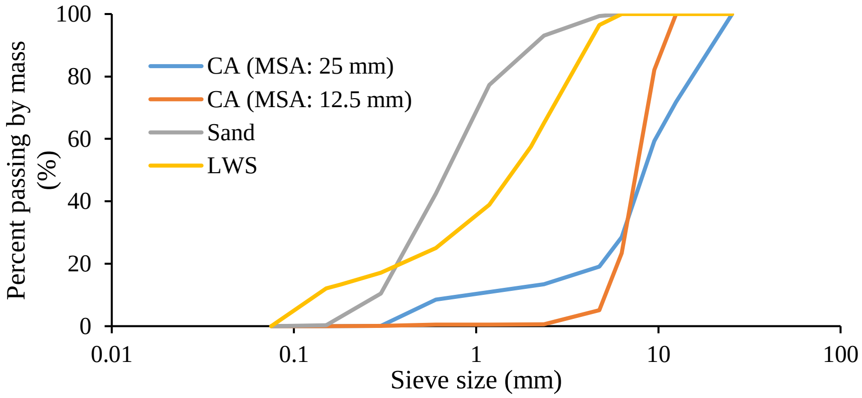

Figure 1. Particle size distribution of aggregates.

Table 2. Physical properties of aggregates.

Aggregate type	**Specific gravity**	**Absorption (%)**	**Desorption at 94% relative humidity (%)**
LWS	1.65	23.45	70.3
Sand	2.58	2.24	--
CA (12.5 mm)	2.48	1.16	--
CA (25 mm)	2.69	1.44	--

Table 3. Physical properties of fibers.

Fiber type	**Specific gravity**	**Length (mm)**	**Diameter (mm)**	**Aspect ratio**	**Tensile strength (MPa)**	**MOE[*] (GPa)**
Micro steel	7.85	13	0.2	65	1100-1300	220
Macro steel	7.85	30	0.56	54	1100-1300	220
Synthetic	0.92	51	0.7	74	600-650	9.5

[*] MOE refers to modulus of elasticity.

2.2. SPECIMEN PREPRATION

A 150-liter drum mixer was used and the mixing process involved: 1) homogenization of sand and pre-saturated LWS for 1 min; 2) addition of CA and fibers along with half of the mixing water and mixing for 1 min; 3) addition of power and half of the remaining mixing water and mixing for 1.5 min; 4) gradual addition of the remaining water along with the HRWRA during mixing for 3 min; and 5) resting the material for 2 min followed by a final mixing period of 2 min.

Table 4. Mixture proportions of investigated mixtures.

Mixtures (Kg/m^3)	**REF**[a]	**STST**[a]	**STST+EA**[a,b]	**STST+LWS**[b]	**STST+EA+LWS**[a,b]	**SYN+EA**[a]
Cement	162	162	154	161	153	154
Fly ash	126	126	120	125	119	120
Slag	72	72	68	71	68	68
EA	-	-	18	-	18	18
Water (w/p = 0.4)	144	144	144	143	143	144
River sand	765	771	771	590	590	773
LWS	-	-	-	126	126	-
CA (12.5 mm)	478	470	470	466	466	470
CA (25 mm)	668	657	658	652	652	656
Macro steel fibers	-	31	31	31	31	-
Micro steel fibers	-	8	8	8	8	-
Synthetic fibers	-	-	-	-	-	5
HRWRA	0.04	0.09	0.07	0.03	0.06	0.07

[a] Indicates mixtures subjected to 7-d moist curing.
[b] Indicates mixtures subjected to 1-d moist curing.

For each mixture, samples were cast for measuring the rebar corrosion, drying shrinkage, transport (water absorption and bulk resistivity), and mechanical properties of concrete. Prismatic samples measuring 90x200x635 mm were used for corrosion testing, as shown in Figure 2. The samples were prepared with embedded rebars with cover depths of 25 38, and 50 mm. Prior to casting, rebars measuring 250 mm in length and 12.7 mm in diameter were wire brushed to remove any rust layer. The extreme ends of the rebars that protrude outside the concrete specimens as well as some of the rebar embedded in the concrete samples were coated with epoxy to minimize localized corrosion at the edges. The uncoated region of the rebar exposed to corrosion was limited to 125 mm in length as indicated in Figure 2. Additionally, the rebars were drilled, tapped, and attached to a stainless-steel screw and nut for connecting to the electrical wires during the corrosion test.

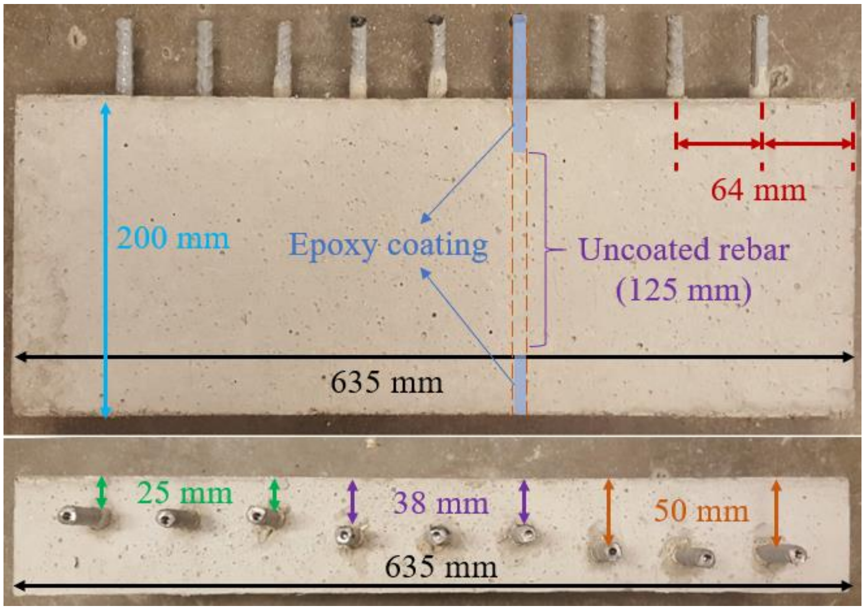

Figure 2. Dimensions of corrosion test sample.

Prismatic concrete samples measuring 75x75x400 mm were cast to assess drying shrinkage and flexural performance, and 100x200 mm cylinders were prepared for measuring compressive strength and transport properties. The curing process for the test samples involved: 1) initial curing by covering the freshly-cast samples with wet burlap and plastic sheet for 24 ± 1 h; and 2) initial curing with wet burlap followed by storage in lime-saturated water for 6 d. These curing conditions are referred to as 1-d and 7-d moist curing, respectively. Length change measurements of shrinkage specimens was started immediately after demolding with the samples corresponding to 7-d moist curing stored in lime-saturated water at 23 ± 2^0C and those of 1-d of moist curing maintained at 23 ± 2^0C and 50% ± 4% relative humidity. At the end of moist curing, the samples were allowed to air-dry until the age of testing. This was 90 d for mechanical and transport properties and corrosion testing. These curing conditions (i.e., limited moist curing followed by 90-d air drying) were selected to ensure considerable drying shrinkage occurs in the test samples, and to evaluate the impact of shrinkage mitigating provided by fibers, EA, and LWS on the rebar corrosion, mechanical and transport properties of investigated concrete samples.

2.3. EXPERIMENTAL PROCEDURE

2.3.1. Corrosion Test Setup and Analysis.

2.3.1.1. Experimental procedure. The corrosion test setup included four prismatic samples assembled to form a salt tank, as shown in Figure 3. The samples were subjected to 90 d of air drying (at 23 ± 2^0C and 50% ± 4% relative humidity) before corrosion testing. The base of the assembled tanks was filled with ultra-high performance concrete (UHPC), and the joints were sealed with silicone to prevent water leakage. The UHPC base and the outer surfaces of the tank were coated with a waterproofing agent to minimize the influence of the environment on corrosion test results. A stainless-steel mesh with a 23 mm opening and 2 mm wire diameter was placed in the salt tank to serve as cathode during the corrosion test. The mesh was weaved with a tinned copper wire to maintain uniform charge distribution across the mesh. The electrical connections were established between the embedded rebars (anode) and steel mesh (cathode) for each prismatic sample using 18-gauge electrical wire and panels with a 5V power supply and 1 Ω shunt resistors. The tanks were saturated with water for 7 d before adding 5% NaCl (by weight). The tanks were then covered to minimize water evaporation, and the water level was frequently checked to ensure constant salinity. The voltage across each of the 1 Ω resistors (i.e., current change) was monitored starting at 5 d after water saturation (i.e., 2 d before NaCl addition) up to the age of 230 d.

2.3.1.2. Rebar corrosion analysis procedure. The chloride-induced macro-cell corrosion process for the individual rebars in the corrosion test setup is illustrated in Figure 4a. The process involves ingress of detrimental Cl^- through the concrete cover and consequent breakdown of the passive layer.

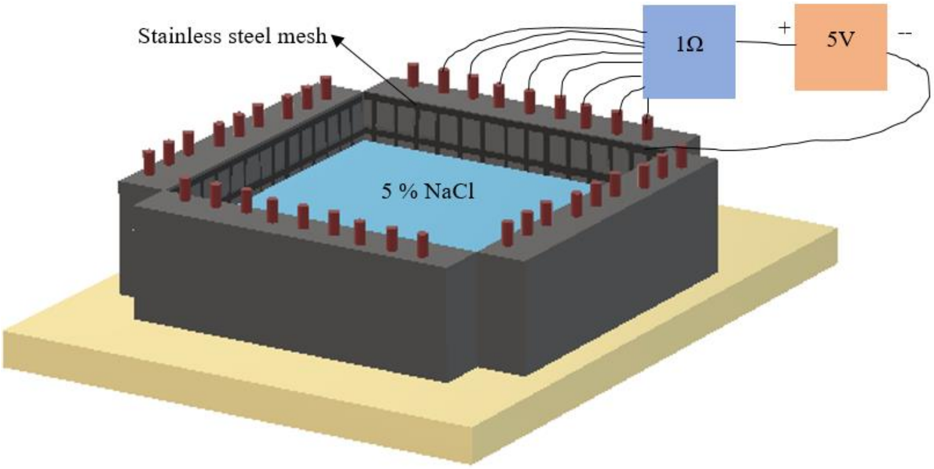

Figure 3. Schematic of corrosion test setup.

The breakdown of the passive layer occurs once the Cl^- concentration at the rebar-concrete interface reaches a critical value. The time needed for the Cl^- to penetrate through concrete and reach the critical concentration at the interface represents the corrosion initiation stage [44].

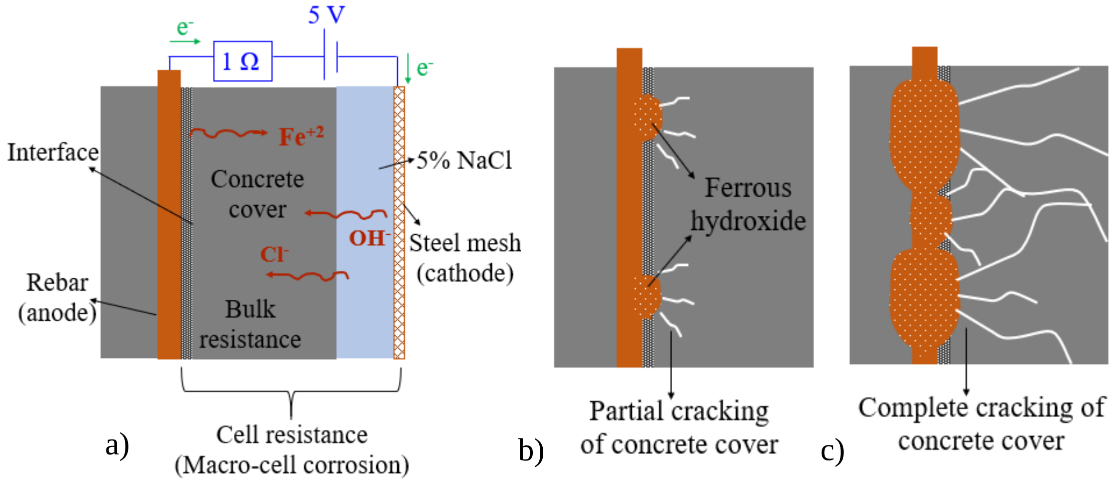

Figure 4. Schematic of a) macro-cell corrosion process, b) partial cracking of concrete cover which results in onset of increase in current, and c) concrete cover cracking which results in a spike in current.

The breakdown of the passive layer results in the dissolution of iron (Fe^{+2}) at the anode (rebar) and flow of electrons released from the anode through the electrical connection to the cathode (stainless steel mesh), as shown in Figure 4a. This results in oxygen reduction (formation of OH^-) at the cathode [45]. The Fe^{+2} and OH^- react to form the ferrous hydroxide, which further hydrates to form expansive corrosion products. These products exert expansive stresses on concrete, which results in crack initiation at the rebar interface, as shown in Figure 4b, when the expansive stress exceeds the tensile strength of the surrounding concrete [46, 47]. The cracking at the interface increases the transport rate of Cl^-, Fe^{+2}, and OH^- ions, thus increasing the rate of corrosion product formation [48]. The expansive pressure generated by the products results in crack propagation and ultimately cracking concrete surface [49], as shown in Figure 4c. The time from the de-passivation of the rebar to the cracking of the concrete cover represents the corrosion propagation stage.

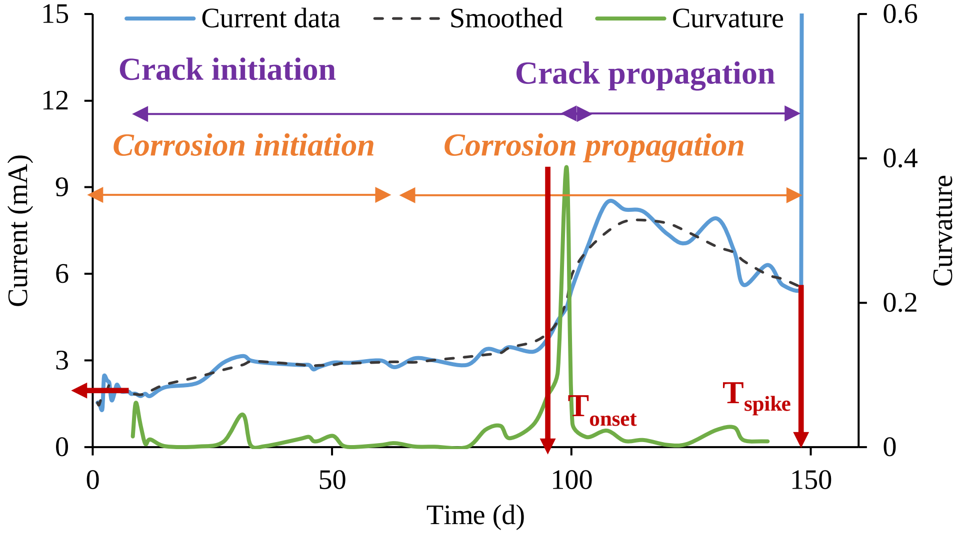

Figure 5. Typical macro-cell current data along with the smoothed and curvature values. Estimated corrosion indicators are shown in red.

The typical current variation results of the rebar obtained from the corrosion test are shown in Figure 5. In this study, the current variation of the rebar is divided into two phases (i.e., crack initiation and propagation phases). The crack initiation phase encompasses the corrosion initiation stage and part of the corrosion propagation stage, as indicated in Figure 5. The results in Figure 5 show an initial increase of current between 0-5 d (due to salt addition) followed by a region with constant current over time. This constant region represents the crack initiation phase, and it includes the corrosion initiation stage and expansive corrosion products formation during the corrosion propagation stage. The partial cracking at the interface at the end of the crack initiation phase is reflected by the onset of the increasing trend in the current (e.g., 100 d in Figure

5). This shift in current is due to the increase in concrete transport properties as a result of expansive stresses exerted by the corrosion products on the concrete [50]. Extension of cracking to the surface of concrete is shown by the drastic increase (i.e., spike) in the current (e.g., 150 d in Figure 5). This duration from the onset of increase in current to the spike in current indicates the crack propagation phase, which results in cracking of the rebar cover [51].

Based on this understanding, the rebar corrosion behavior was assessed using three indicators: 1) initial current after salt addition (I_{in}), which indicates the cell resistance; i.e., macro-cell corrosion resistance between the rebar (anode) and stainless steel mesh (cathode), as shown in Figure 4a; 2) time corresponding to the onset of the increase in current (T_{onset}) due to partial cracking at the interface, as shown in Figure 4b; and 3) time corresponding to the sudden spike in current (T_{spike}) due to cracking of the concrete cover, as shown in Figure 4c. As shown in Figure 5, the T_{spike} is well-defined point in the current-time plots, while the T_{onset} is not easily observed. As a result, the T_{onset} was identified as the time corresponding to the point of maximum curvature located within the increasing region of the current-time plot [52, 53], as shown in Figure 5. To reduce the effect of small fluctuations in current (i.e., noise in the data) on curvature calculation, current data were smoothened out using the Adjacent-averaging method. The curvature was estimated for smoothened-out data within the increasing region of the current-time plot.

2.3.2. Concrete Properties.

2.3.2.1. Drying shrinkage. The prismatic samples of 75x75x400 mm that were cast to evaluate drying shrinkage were maintained at 23 ± 2^0C and 50% ± 4% relative humidity as per ASTM C 157. Length changes were measured for over 120 d since casting of the samples. After demolding, the length of the sample was measured, and this was used as the initial length for the estimating the shrinkage strain. The measurements were taken for three samples for each mixture, and the average strain values were reported.

2.3.2.2. Transport properties. The 100x50 mm cylinders were saw-cut from the center of the 100x200 mm cylinders for water absorption measurement after 90 d of air drying. The samples were then conditioned at controlled temperature and relative humidity values as specified in ASTM C1585. The side surfaces and one face of each cylinder were sealed with epoxy to minimize exposure to the external environment. The mass of the samples was recorded, and they were placed in a container exposing the unsealed surface to water. The change in the mass of the sample due to water absorption was measured over time, starting from 1 min to 8 d. The difference in mass and cross-sectional area of test samples was used to estimate the initial sorptivity and secondary sorptivity. The initial sorptivity was calculated based on the mass of water intake during the first 6 h. In contrast, the secondary sorptivity was calculated based on the mass of water taken from 1 d up to 8 d. For each mixture, three samples were tested, and the average values were reported.

The bulk resistivity of the mixtures was measured on 100x200 mm cylinders using the plate electrodes. The ends of the cylinders were trimmed to have leveled surface for bulk resistivity measurement. The samples were stored in the simulated pore solution for 7 d at 22 ^{0}C before testing, as per ASTM C1876. Three successive measurements of the bulk resistivity were taken, and the average values were reported.

2.3.2.3. Mechanical properties. The compressive strength of the 100x200 mm cylinders after 90 d of air drying were measured in accordance with ASTM C 39. The flexural properties of mixtures were tested by subjecting the 75x75x400 mm beams to a four-point loading test after 90 d of air drying in accordance with ASTM C 1609. Three samples were tested for each mixture, and the average results of compressive strength, flexural strength and toughness were reported.

3. RESULTS AND DISCUSSIONS

3.1. REBAR CORROSION

The corrosion behavior was monitored for 72 rebars embedded in eight different concrete mixtures at three cover depths. The corrosion of rebars was assessed using the changes of current values from three sets of rebars embedded at different cover depths. Typical variations of the current with time are shown in Figure 6a and Figure 6b for three sets of rebars embedded in the REF-7D mixture at cover depths of 25 and 38 mm, respectively. The results indicate that the initial current was similar for the three rebar sets that have the same cover. However, significant variation in current values was noted with the progress of corrosion, hence reflecting a distinct corrosion behavior for each rebar. Hansson et al. [54] noted that the high variation in the current is expected due to the inhomogeneous microstructure of concrete, different ingression rate of Cl^-, and formation of the passive film on the rebar. The variability of the results of the variation in current with test time makes it difficult to compare the corrosion behavior of rebars embedded in concrete mixtures with different properties and cover depths. Therefore, for a given concrete mixture and cover depth, the rebar with the earliest spike in current (i.e., lower T_{spike}) was considered to be representative of the corrosion behavior for the set of rebar duplicates. For example, in Figure 6a, the spike in current occurred for rebar 3 at 150 d. As a result, it is considered to show the representative corrosion behavior of rebar groups embedded in the REF-7D mixture at 25 mm cover depth. It should be noted the occurrence of a spike in rebar current (i.e., T_{spike}) was supported by the visual appearance of cracks and rust at the concrete surface of test samples.

If no spike is detected during the exposure period, the rebar that had the earliest onset of increase in current (i.e., lower T_{onset}) was considered to show the representative corrosion behavior. For example, in Figure 6b, during 230 d of testing, no spike was observed for the three tested rebars. However, the onset of increase in current occurred for rebar 3 at around 100 d. As a result, this result is considered to be representative of the corrosion behavior of rebars embedded in the REF-7D mixture at 38 mm cover depth. Using this representative rebar approach, the corrosion indicators (i.e., I_{in}, T_{onset}, and T_{spike}) for the investigated reinforced concrete mixtures with rebars covers of 25, 38, and 50 mm, were estimated.

Figure 7 shows the current results and the corrosion indicators of selected concrete mixtures at 25 mm cover depth. For mixtures subjected to 7 d moist curing in Figure 7(a-c), the current was constant for a certain time before an increasing trend and consequent peak in current. Whereas for samples subjected to 1-d moist curing (in Figure 7d), the increase in current occurred immediately after salt addition. However, after T_{onset}, a decreasing trend in the current occurred until T_{spike}. Such decrease in current was due to the delayed hydration of 1-d samples upon exposure to NaCl solution. The delayed hydration could decrease conductivity and transport properties of concrete over time.

3.1.1. Initial Current (I_{in}). The estimated values of corrosion indicators obtained from the representative rebar approach for all concrete mixtures at different cover depths are shown in Table 5. The results show that the increase of cover depth reduced I_{in} for all mixtures, indicating an increase in cell resistivity (i.e., the macro-cell corrosion resistance between the rebar and stainless-steel mesh). As for moist curing time, approximately 75% to 500% higher values of I_{in} were recorded as the moist curing reduced from 7- to 1-d at any given cover depth. These results are attributed to the lower degree of hydration of 1-d moist cured concrete samples.

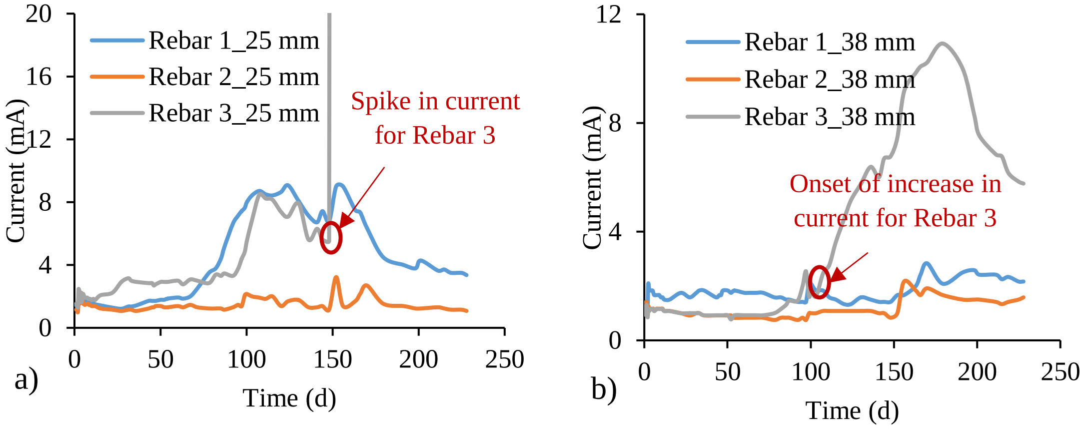

Figure 6. Current variation with time for individual rebars of REF-7D mixture at cover depths of a) 25 mm and b) 38 mm.

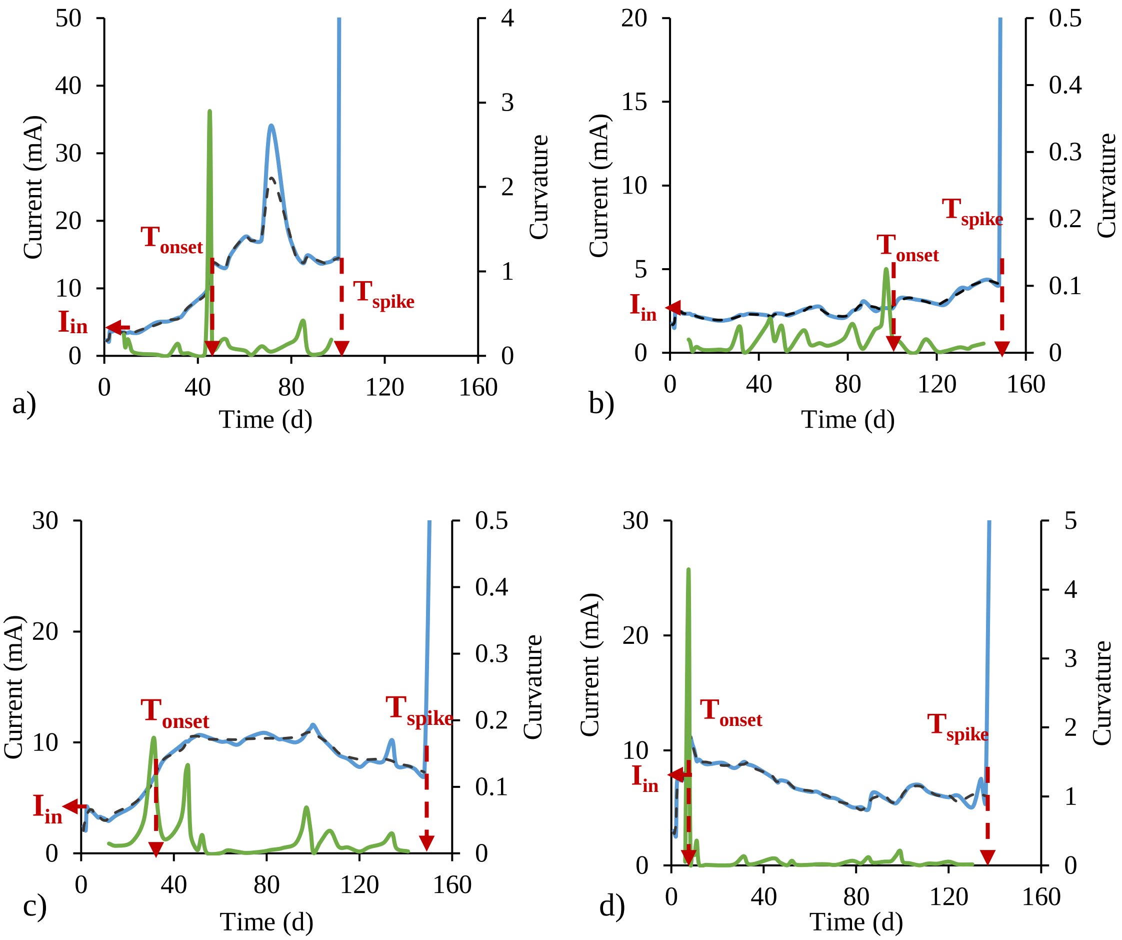

Figure 7. Current data (blue) at 25 mm cover along with smoothed (black), curvature (green), and corrosion indicators (red) for selected concrete mixtures: a) STST+EA-7D, b) SYN+EA-7D, c) STST+EA+LWS-7D, and d) STST+EA+LWS-1D.

The relative current values (i.e., ratio of I_{in} of concrete at specific cover to I_{in} of reference mixture at that specific cover) are calculated and shown in Figure 8a. For 7-d moist cured samples at 25 mm cover depth, the I_{in} was 24%, 41%, 106%, and 150% higher for the STST-7D, SYN+EA-7D, STST+EA-7D, and STST+EA+LWS-7D mixtures compared to the REF-7D mixture, respectively. These relative current values indicate that the incorporation of fibers, EA, and LWS decreased the cell resistivity of 7-d samples. The decreased cell resistivity for steel-FRC can be partly attributed to the conductivity of steel fibers [39]. For 1-d moist cured steel-FRC samples at 25 mm cover, the I_{in} was highest for mixture with EA and this can be due to the lack of sufficient water available for the hydration of EA [27]. However, with the combined use of EA and LWS, the internal curing provided LWS resulted in 45% reduction in I_{in}. For all mixtures, the influence of the mixture constituents (i.e., fibers, EA, and LWS) on I_{in} was less significant with the increase in cover depth from 25 to 38 and 50 mm. This could be explained by the dominant effect of drying on the transport properties of concrete at the surface consequently reducing corrosion resistance for rebars at lower cover depth i.e., 25 mm.

Table 5. Corrosion indicators of investigated mixtures.

Mixture	**Initial current, I_{in} (mA)**			**Onset of increase in current, T_{onset} (d) [1]**			**Time of spike in current, T_{spike} (d) [2]**		
	25 mm	**38 mm**	**50 mm**	**25 mm**	**38 mm**	**50 mm**	**25 mm**	**38 mm**	**50 mm**
REF-7D	1.7	1.3	0.9	99	99		148		
STST-7D	2.1	1.3	1.0	46	46		107		
STST+EA-7D	3.5	1.4	1.0	46	85		100		
STST+EA+LWS-7D	4.2	2.0	1.1	31	46	198	124	148	215
SYN+EA-7D	2.4	1.4	1.0	97	99		144		
STST+LWS-1D	12.8	6.2	4.7	8	10	52	50	120	
STST+EA-1D	13.3	8.3	4.5	8	11		46	71	
STST+EA+LWS-1D	7.3	4.7	3.4	8	8	45	136		

[1] Cells in grey indicate absence of an increase in current due to partial cracking at interface, and curvature values are significantly low (< 0.1) during 230 d of testing.

[2] Cells in grey indicate absence of a sudden spike in current due to cracking of concrete cover during 230 d of testing.

3.1.2. Onset of Increase in Current (T_{onset}). For a given cover of 25 mm in Table 5, the 7-d moist cured concrete mixtures had T_{onset} in the ranges of 31-99 d while all the 1-d moist cured concrete mixtures had T_{onset} at 8 d. The significantly lower values of T_{onset} for 1-d moist cured samples agree with the larger I_{in} noted for these samples. The high I_{in} for 1-d moist cured samples indicates a faster transport of ions through the concrete, which would lead to earlier formation of expansive corrosion products and consequent crack initiation at the interface.

In terms of mixture constituents, for a given moist curing duration (7 d) and the cover depth (25 mm), the T_{onset} happened earliest for the steel-FRC with the hybrid system of EA+LWS at 31d and was most delayed for REF-7D mixture at 99 d. This agreed with the 150% higher I_{in} observed for STST+EA+LWS-7D compared to REF-7D mixtures. Additionally, the use of synthetic fibers and EA had shown no significant effect on the T_{onset}. The increase in concrete cover to 38 mm delayed the T_{onset} for all mixtures. With increase in cover depth to 50 mm, no T_{onset} was observed for 7-d moist cured concrete mixtures during the 230 d of testing except for STST+EA+LWS-7D mixture, which had T_{onset} at 198 d

3.1.3. Time of Spike in Current (T_{spike}). All the concrete mixtures showed a spike in current during 230 d of testing for rebars at 25 mm cover, and the T_{spike} values were in the ranges of 100-148 d for 7-d and 46-136 d for 1-d moist cured samples. The duration between T_{onset} and T_{spike} can be used to estimate the time taken for expansive stress exerted by corrosion products to exceed the residual strength of the partially cracked concrete [55]. Additionally, this spread between T_{onset} and T_{spike} reflects the resistance of the concrete to failure due to corrosion. Figure 8b shows the results of spread between the T_{onset} and T_{spike} for 1- and 7-d samples with rebars at 25 mm cover.

Unlike the T_{onset}, the inclusion of a hybrid system of EA and LWS showed a beneficial influence on the resistance of the concrete to failure due to corrosion cracking. For a given curing condition (i.e., 7 d moist curing) and cover depth (25 mm), the spread between T_{onset} and T_{spike} was highest for the STST+EA+LWS-7D mixture (93 d). This could be due to the improvement in the bridging effect of steel fibers with the hybrid use of EA and LWS [56]. Such enhancement is due to improved adhesion between the matrix and steel fibers [20, 57, 58] as a result of an increased degree of hydration of the EA in the presence of LWS [6]. The same effect was observed for mixtures prepared with EA and LWS subjected to 1 d of moist curing. A significant delay in T_{spike} was observed for the STST+EA+LWS-1D mixture (128 d) despite the low T_{onset} of 8 d. This delay in T_{spike} can partly be attributed to the enhanced crack bridging of steel fibers in the presence of EA and LWS. On the other hand, such delay can also be due to the hydration of concrete during the continued exposure of 1-d moist cured samples to NaCl solution during corrosion testing. The delayed hydration is evident from the decreasing trend in current with time between T_{onset} and T_{spike} in Figure 7d.

The fiber type also plays an important role on the resistance of samples to corrosion cracking. The results indicated that the spread between T_{onset} and T_{spike} was slightly higher for the STST+EA-7D mixture (54 d) compared to the SYN+EA-7D mixture (42 d). The latter value could be due to the relatively longer synthetic fibers that do not provide an effective crack bridging compared to the steel fibers (micro and macro) used that can restrict cracking at different scales.

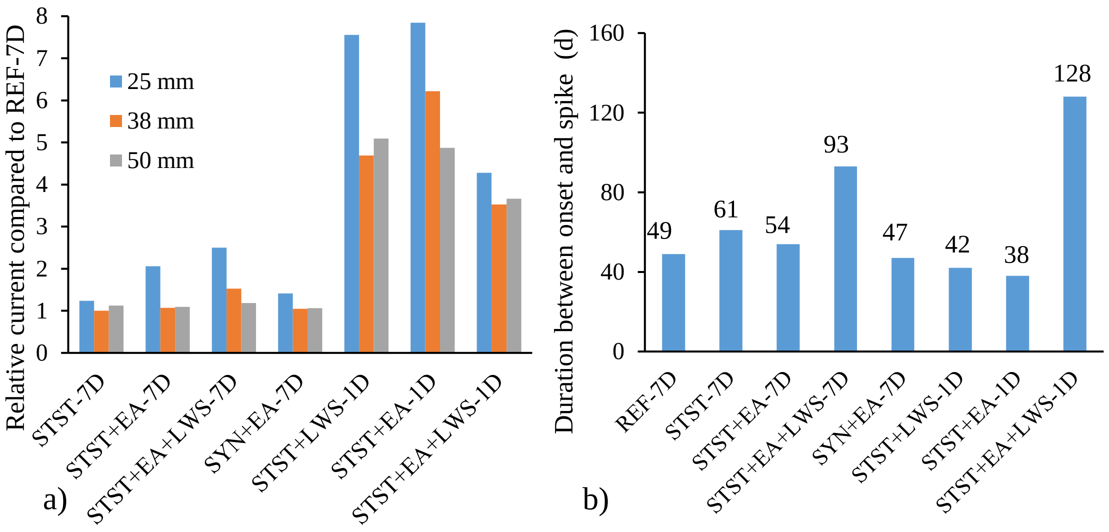

Figure 8. a) Variation of relative initial current (ratio of I_{in} for concrete at specific cover depth to I_{in} for REF-7D at same cover depth) and b) duration between onset of increase and sudden spike in current for concrete with rebar cover of 25 mm.

3.2. CONCRETE PROPERTIES

3.2.1. Drying Shrinkage. The shrinkage strain (or length change) results for 7-d and 1-d moist cured samples are shown in Figure 9a and Figure 9b, respectively. Initial expansion was observed for all mixtures (in Figure 9a) during moist curing, and the strain results were approximately 260 micron for the SYN+EA-7D mixture followed by 170 micron for the STST+EA-7D and STST+EA+LWS-7D mixtures, and 120 micron for mixture without any EA (i.e., REF-7D and STST-7D mixtures). The high expansion of the SYN+EA-7D mixture is due to the hydration of EA, which results in the formation of CH platelets that cause expansion [22]. Lower expansion of the mixtures made with steel fibers and EA was due to the ability of the fibers to restrict initial expansion caused by the hydration of EA [20, 36]. Despite the lower early expansion, the shrinkage at 90-d was 41% lower for the steel-FRC mixtures compared to the synthetic-FRC mixtures prepared with 5% EA. This is due to the ability of steel fibers to improve the dimensional stability of the concrete owing to high MOE of steel fibers (220 GPa) compared to synthetic fibers with MOE of 9.5 GPa [21]. Also, the ability of micro and macro steel fibers to mitigate cracking at different scales [21] and the higher ability of hooked end macro steel fibers to restrict the relative slippage between the matrix and fibers during shrinkage [59, 60] can further contribute to reducing shrinkage.

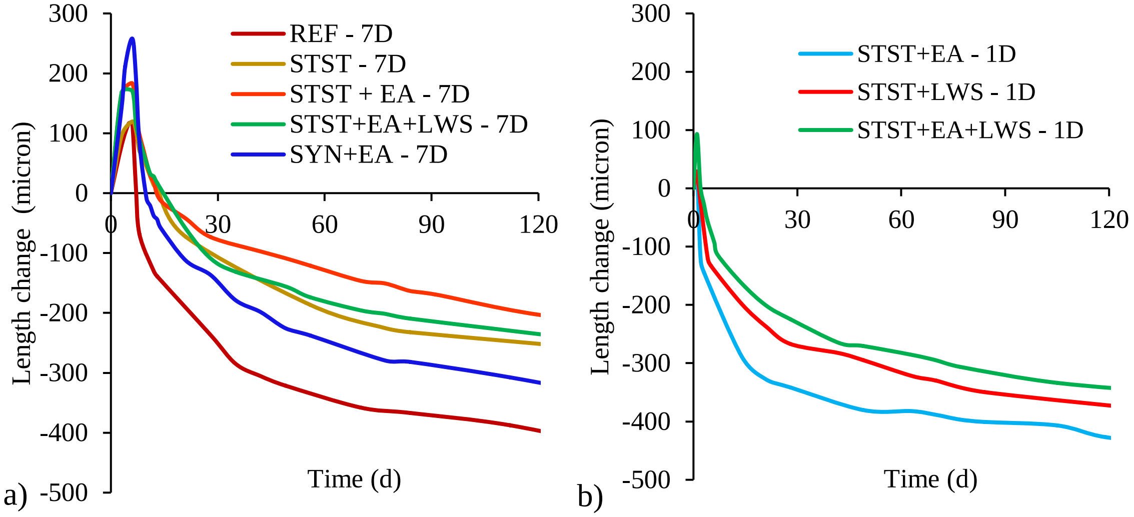

Figure 9. Strain variation with time for a) 7-d moist cured and b) 1-d moist cured samples.

In Figure 9a, the addition of 25% LWS showed no significant effect on early age expansion and slight increase in the 90-day shrinkage compared to steel-FRC containing only EA. In contrast, the combination of EA and LWS had a more significant effect on early age expansion (increase by 230%) and 90-d drying shrinkage (decrease by 20%) for 1-d moist cured steel-FRC compared to the mixtures containing only EA or LWS, as shown in Figure 9b. This was due to the ability of pre-saturated LWS to sustain the hydration of EA [61], and such effect was more accentuated when moist curing was limited to 1 d. These results indicate that the steel fibers effectively improved the concrete specimens' dimensional stability, leading to lower expansion and shrinkage. For 7-d moist curing, the use of EA along with steel fibers was effective at mitigating shrinkage. However, for 1 d of moist curing, the hybrid system containing EA, LWS, and steel fibers had the lowest shrinkage.

3.2.2. Transport Properties.

3.2.2.1. Water absorption. Figure 10a and Figure 10b show the variation of absorbed water over a test period of 8 d for mixtures subjected 7- and 1-d of moist curing, respectively. The tests were carried out after 90 d of air drying. For all mixtures, the absorption rate was faster in the first 6 h, and gradually slowed down over 8 d. The faster absorption rate in the first 6 h is called the initial sorptivity and is a function of the concrete porosity, specifically the porosity of concrete close to the surface exposed to water [62, 63]. The slower rate from 1 to 8 d is referred to as secondary sorptivity, and it is governed by pore size, pore connectivity, and concentration gradient of the bulk concrete [63, 64]. The values of initial and secondary sorptivity are shown in Figure 11a and Figure 11b, respectively.

The total amount of water absorbed after 8 d of testing for the 7-d (Figure 10a) and 1-d (Figure 10b) moist cured samples ranged between 1.2 and 1.8 kg/m^2 and 1.8 and 2.1 kg/m^2, respectively. The higher values for the latter samples indicate higher porosity and pore connectivity, which results in faster ingress of detrimental agents during corrosion, consequently increasing I_{in} and reducing T_{onset}. The high initial sorptivity values of 0.62 to 0.68 mm/hr$^{0.5}$ for 1-d moist cured samples (Figure 11a) also agree with high I_{in} and low T_{onset} values for these mixtures.

Among 7-d moist cured samples, water absorption, initial and secondary sorptivity values were lowest for REF-7D and SYN+EA-7D mixtures and highest for STST+EA+LWS-7D mixture. These results are in agreement with the high I_{in} (up to 150%) and low T_{onset} (up to 70%) results for STST+EA+LWS-7D mixture compared to REF-7D and SYN+EA-7D mixtures with rebars at 25 mm cover. The high values of water absorption, initial and secondary sorptivity for steel-FRC with LWS can be attributed to the high porosity of LWS used. As for the secondary sorptivity values in Figure 11b, the sorptivity values of 7-d moist cured steel-FRC were 50% to 100% higher than that of the REF-7D and SYN+EA-7D mixtures. These high values for steel-FRC indicate high pore connectivity and explain the 50% lower T_{onset} results observed STST-7D and STST+EA-7D mixtures compared to REF-7D and SYN+EA-7D mixtures.

Based on the rebar corrosion, drying shrinkage and water absorption results of the 7-d moist cured samples, the use of steel fibers and EA has a positive effect on reducing shrinkage but increases the transport properties of concrete (i.e., water absorption, initial and secondary sorptivity). Such increase in transport properties results in reduced corrosion resistance of rebars at 25 mm cover. Additionally, for 1-d moist cured samples, the hybrid system containing EA, LWS, and steel fibers is effective at shrinkage mitigation but significantly increases the transport properties of concrete leading to reduced corrosion resistance.

3.2.2.2. Bulk resistivity. The bulk resistivity is highly dependent on the pore structure, degree of saturation, and the conductivity of constituents [65]. The bulk resistivity results of the samples after 90 d of drying are shown in Figure 12a. The bulk resistivity of the 7-d moist cured samples ranged between 14 and 38 kΩ.cm and were approximately 11 kΩ.cm for the 1-d cured samples. These results agree with the higher water absorption noted for latter samples in Figure 10b. Among the 7-d moist cured samples, the steel-FRC had 46%-63% lower bulk resistivity than the REF-7D and SYN+EA-7D mixtures. This could be partly due to the conductivity of steel fibers to the applied AC voltage during the bulk resistivity test [65] as well as the high pore connectivity of steel-FRC mixtures as evident from water absorption and sorptivity results. Figure 12b shows a good relationship between the concrete conductivity (inverse of bulk resistivity) and total water absorption results for the steel-FRC. An increasing trend in conductivity is observed with increase in absorption. Such correlation is due to the influence of concrete porosity and pore connectivity on concrete conductivity and water absorption. The higher porosity and pore connectivity of concrete resulted in higher water absorption and saturation of the pore system with simulated pore solution, consequently leading to high conductivity.

3.2.3. Mechanical Properties.

3.2.3.1. Compressive strength. Figure 13a shows the compressive strength results of the investigated mixtures. The strength values for 7 and 1 d moist cured samples were in the range of 40-47 MPa and 21-25 MPa, respectively. For the mixtures subjected to 7-d moist curing, compared to the REF-7D mixture, slightly lower compressive strength was obtained for the STST-7D (9%), STST+EA-7D (11%), STST+EA+LWS-7D (15%), and SYN+EA-7D (6%) mixtures. This reduction is consistent with the increase in water absorption observed for the FRC compared to the

REF-7D mixture (Figure 10a). Among the 1-d moist cured samples, the STST+LWS-1D mixture had up to 18% higher compressive strength than the STST+EA-1D and STST+EA+LWS-1D mixtures. This can be due to the increased degree of cement hydration in the presence of LWS.

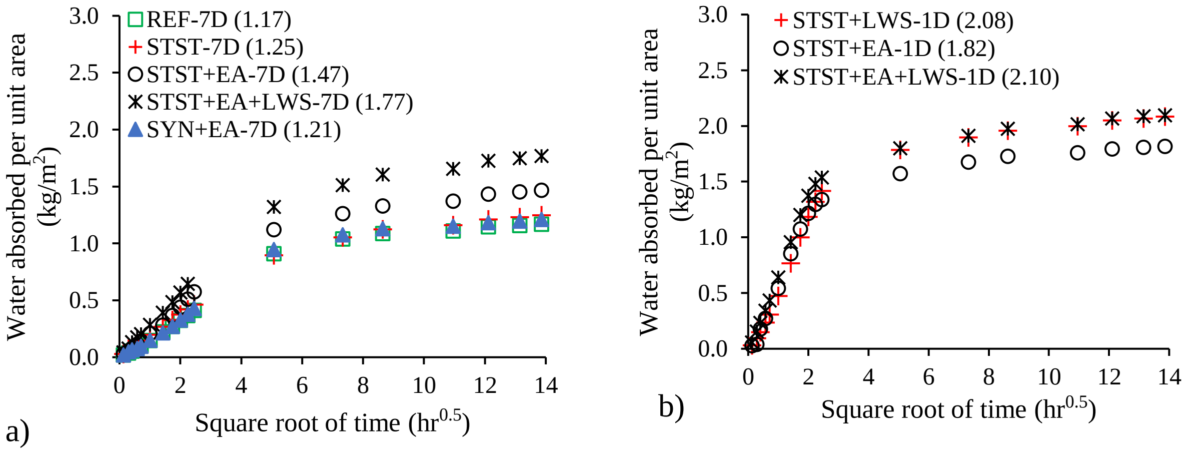

Figure 10. Water absorption as function time for a) 7-d and b) 1-d moist cured concrete mixtures. Total absorption values are indicated in parenthesis.

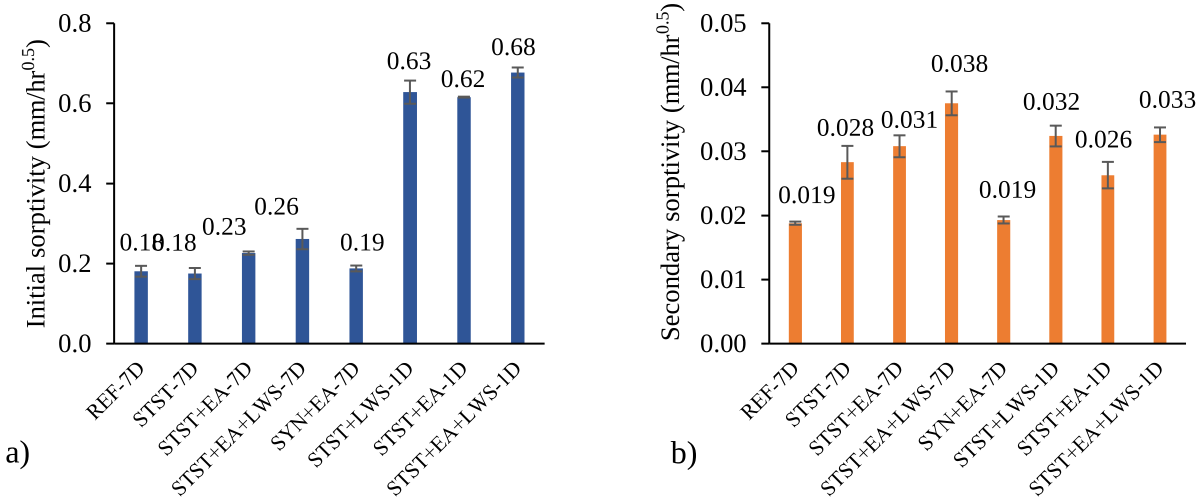

Figure 11. Sorptivity results of investigated mixtures: a) initial sorptivity and b) secondary sorptivity.

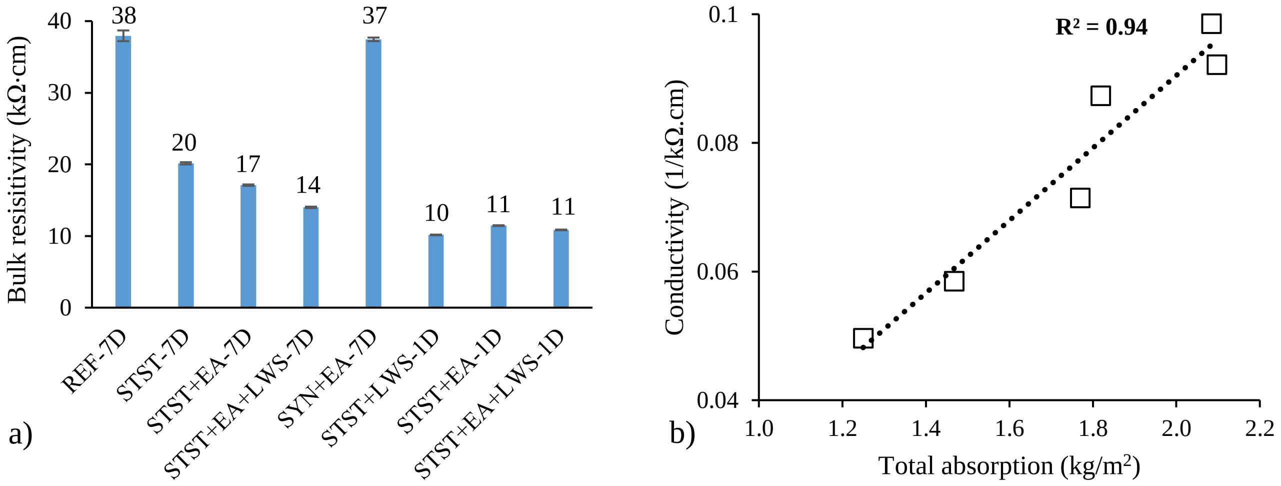

Figure 12. a) Bulk resistivity results of investigate mixtures, and b) relationship between conductivity (1/resistivity) and water absorption of steel-FRC.

3.2.3.2. Flexural properties. The MOR and flexural toughness of the investigated samples are shown in Figure 13b. The MOR values ranged between 4.9 and 5.4 MPa for the 7-d moist curing and 3.4 and 3.7 MPa for the 1-d moist curing. A more significant difference was observed in the toughness results. Compared to REF-7D mixture, the addition of fibers (steel or synthetic) resulted in considerable improvement in post-cracking load-bearing ability and flexural toughness. The flexural toughness was highest (36%) for the steel-FRC with EA and LWS, while no significant difference was observed between the STST-7D and STST+EA-7D mixtures. The high toughness of the STST+EA+LWS-7D mixture could be attributed to increased hydration of EA in the presence of LWS, which can lead to improved adhesion between the fibers and concrete matrix [36, 57]. Compared to the STST+EA-7D mixture, the toughness was 50% lower for the SYN+EA-7D mixture. The higher toughness for steel-FRC can be attributed to the better adhesion between the brass-coated micro steel fibers [20, 58] and matrix and the ability of micro and macro steel fibers to mitigate cracking at different scales [21].

Additionally, the hooked ends of macro-steel fibers resulted in a better bond between the matrix and fiber, thereby restricting the relative slippage [59, 60]. Among the 1-d moist cured samples, the relatively higher values of toughness for mixtures with LWS despite the high porosity of LWS could be due to the improvement in the interfacial bond between the fibers and matrix in the presence of LWS as observed by [57].

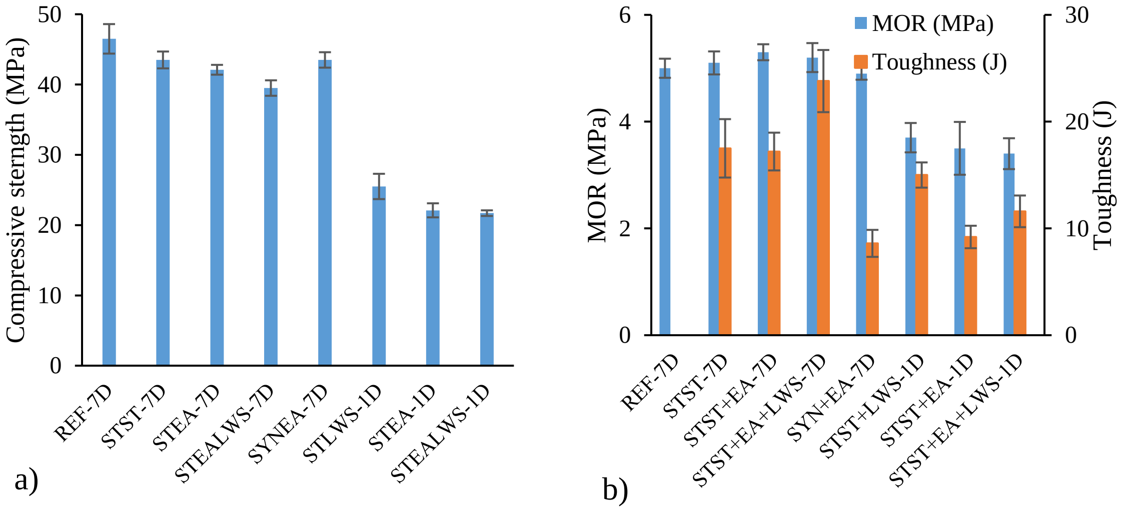

Figure 13. a) Compressive strength, b) MOR and toughness results of investigated mixtures.

3.3. RELATIONSHIP BETWEEN REBAR CORROSION AND CONCRETE PROPERTIES

Rebar corrosion process involves various corrosion initiation and propagation stages, as illustrated in Figure 14. The figure also shows the key concrete properties effecting the duration of each stage, which includes transport properties, porosity, and mechanical properties. During corrosion initiation, the ingress of Cl^-, Fe^{+2}, and OH^- ions through concrete cover results in de-passivation of the rebar. The rate of ingress of ions is mainly controlled by the transport properties of the concrete [66, 67]. The time taken for de-passivation is a function of the macro-cell resistance between the anode and cathode, which is assessed in this study using corrosion indicator, I_{in}.

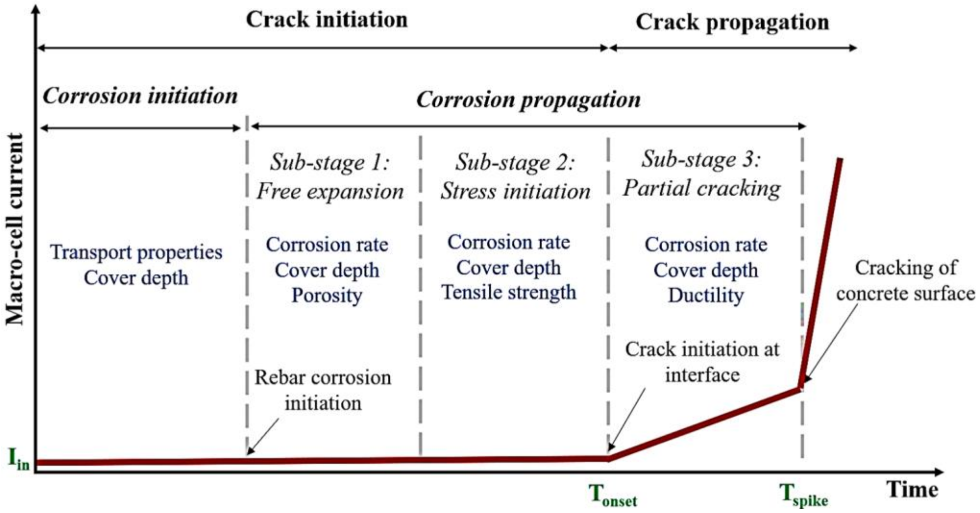

Figure 14. Stages of rebar corrosion and concrete cracking; key parameters affecting duration of each sub-stage are indicated.

Figure 15a shows the relationship between the measured conductivity results and estimated I_{in} values. To account for the influence of cover depth, the ratio of concrete conductivity to cover depth is used. An increasing trend in I_{in} can be observed for rebars with an increase in concrete conductivity. Higher conductivity of concrete implies less resistance to the flow of electrons through concrete, leading to higher I_{in} and lower cell resistivity. The correlation coefficient (R^2 value) of 0.75 indicates scatter in I_{in} data. Hornbostel et al. [68-70] also reported poor correlation between the conductivity of bulk concrete and that of the macro-cell. The authors noted that chloride-induced corrosion often starts in a small anodic region (i.e., not over the entire cross-section of the rebar).

These regions can be smaller or similar in size to inhomogeneities corresponding to aggregates, voids in concrete, and interface between the concrete and rebar. In such a case, the macro-cell corrosion rate is affected by the electrical properties of the inhomogeneities in addition to those of the bulk concrete. As shown in Figure 14, the corrosion propagation stage involves three sub-stages [46, 47, 55]. Sub-stages 1, 2, and 3 correspond to free expansion of corrosion products, stress initiation in concrete, and partial cracking of concrete cover, respectively. No significant cracking occurs in concrete during the first two sub-stages, which are part of the crack initiation phase. The third sub-stage involving the partial cracking of concrete cover is part of the crack propagation phase.

During free expansion (sub-stage 1), corrosion products can occupy some of the porous regions in the concrete matrix and may not exert critical tensile stress on the surrounding material. The duration of free expansion depends on the volume of interconnected pores present around the rebar and rate of corrosion product formation [47]. However, the increase in concrete porosity increases the porous region available for the corrosion products that extends the free expansion duration. Furthermore, concrete porosity can increase the rate of corrosion product formation that reduces the free expansion duration. Therefore, it is difficult to assess the effect of transport properties of the concrete on the duration of the free expansion sub-stage.

During the stress initiation period (sub-stage 2), porous regions in concrete are occupied with corrosion products and expansive pressure (tensile stress) is exerted on the surrounding concrete. No significant cracking or changes in the current occur during this sub-stage. At the end of the sub-stage, stress exerted by corrosion products can exceed the tensile strength of the concrete leading to crack initiation. The time taken for crack initiation is determined using the corrosion indicator, T_{onset}. The duration of the stress initiation period (sub-stage 2) depends on the expansive stress exerted by the corrosion products and tensile strength of the concrete [46, 47]. Figure 15b shows the relationship between T_{onset} and the ratio of conductivity to cover depth. Decreasing trend in T_{onset} was observed with the increase in conductivity to cover depth ratio. Higher concrete conductivity leads to faster ingress of detrimental agents, leading to faster corrosion product formation and consequently crack initiation. However, the lower correlation between T_{onset} and I_{in} (R^2 value of 0.78) is due to the difference in tensile strength of the investigated mixtures. To account for the effect of tensile strength of concrete samples, Figure 15c shows the relationship between the T_{onset} and combined parameter (i.e, ratio of MOR to concrete conductivity and cover depth). The R^2 value between the combined factors and T_{onset} was 0.83 compared to 0.78 (Figure 15b) indicating a better correlation. This illustrates the importance of considering the transport properties, concrete cover, and cracking resistance of the concrete on the duration to crack initiation.

During the crack propagation phase or partial cracking of concrete cover (sub-stage 3), expansive pressure generated by corrosion products can lead to crack propagation in concrete. The visible cracking at concrete surfaces is represented by the corrosion indicator, T_{spike}. The duration between crack initiation and surface cracking (duration of sub-stage 3) depends on the rate of corrosion product formation, cover depth, and residual strength of cracked concrete [55]. Figure 15d shows a relationship between the relative difference of T_{spike} and T_{onset} and flexural toughness of the concrete. The data correspond to specimens with 25 mm cover depth subjected to 7 d of moist curing. The results indicate that the increase in flexural toughness can affect the delay in T_{spike} compared to T_{onset}. The relationship between corrosion indicators and material properties in Figure 15 suggest the influence of shrinkage mitigating systems i.e., fibers, EA, and LWS on transport and mechanical properties of concrete needs to be assessed to understand their influence on corrosion resistance of reinforced concrete samples.

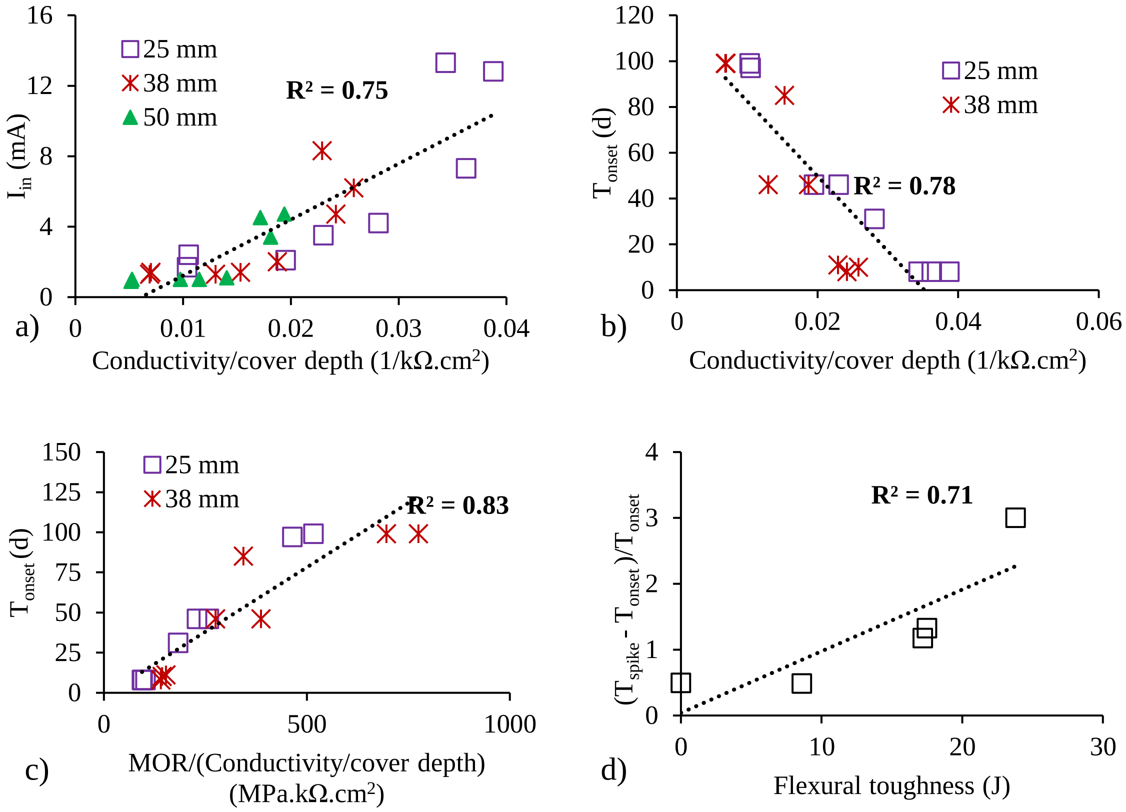

Figure 15. Relationship between corrosion indicators and concrete properties: a) I_{in}, conductivity and cover depth; b) T_{onset}, conductivity and cover depth; c) T_{onset}, MOR, conductivity, and cover depth; and d) relative difference of T_{spike} and T_{onset} vs. flexural toughness for 7-d of moist cured FRC with 25 mm cover depth.

4. CONCLUSIONS

The effect of using steel and synthetic fibers, EA, and LWS on chloride-induced corrosion of rebars embedded in concrete prismatic samples with cover depths of 25, 38, and 50 mm was investigated. Prior to corrosion assessment, the concrete was subjected to limited moist curing duration of 1 or 7 d followed by 90 d of air drying. Transport and mechanical properties of concrete subjected to same curing conditions were investigated. Such curing conditions were selected to allow for drying shrinkage of test samples and evaluate the impact of shrinkage mitigating provided by fibers, EA, and LWS on corrosion resistance of embedded rebars. Based on the above results, the following conclusions are warranted:

1. The initial macro-cell current (I_{in}) is shown to increase with the electrical conductivity of the concrete. The time corresponding to the onset of increase in current due to crack initiation (T_{onset}) increases with the MOR, cover depth, and transport properties. Additionally, the duration between T_{onset} and time corresponding to sudden spike in current due to concrete surface cracking (T_{spike}) increases with the flexural toughness of the concrete.
2. Despite the limited moist curing, the use of steel fibers, EA, and LWS can reduce drying shrinkage and increase cracking resistance; however, such materials can have a detrimental effect on transport properties under these curing conditions, leading to lower macro-cell resistance. On the other hand, the use of synthetic fibers was less effective at shrinkage mitigation and cracking resistance, yet such fibers had no detrimental effect on transport properties and corrosion resistance.

3. Depending on the mixture constituents in use, the increase in moist curing from 1 to 7 d decreased 90-d drying shrinkage by 30% to 60%, water absorption by 15% to 20% and electrical conductivity by 25% to 55% and increased MOR by 50% and flexural toughness by 100%. The enhancement in transport and mechanical properties lead to decrease I_{in} by 42% to 83%, and delay in T_{onset} and T_{spike} by at least 300% and 100%, respectively.
4. Compared to 7-d moist cured concrete made without any fibers, the use of 0.5% micro-macro steel fibers resulted in 35% reduction in 90-d drying shrinkage and enhancement in flexural toughness. The improvement in flexural toughness contributed to 170% increase in the relative duration between T_{onset} and T_{spike}. However, the use of steel fibers also increased water absorption by 10% and electrical conductivity of concrete by 90% leading to 10% to 24% increase in I_{in} and 50% reduction in T_{onset}.
5. Compared to 7-d moist cured concrete samples with only 0.5% steel fibers, the combined use of 0.5% steel fibers and 5% EA led to 30% further reduction in 90-d drying shrinkage. The addition of EA also increased water absorption and electrical conductivity by 20%. Such detrimental effect on transport properties, increased I_{in} and reduced T_{onset} by up to 70% and 85%, respectively.
6. For FRC with 5% EA, the replacement of 0.5% steel fibers with 0.5% synthetic fibers increased 90-d drying shrinkage by 70% but reduced the water absorption, electrical conductivity, and flexural toughness by approximately 80%, 120%, and 50%, respectively. The enhancement in transport properties with the replacement

of steel with synthetic fibers led to 30% reduction in I_{in} and up to 110% and 45% increase in T_{onset} and T_{onset}, respectively

7. The addition of 25% LWS to steel-FRC with 5% EA, reduced 90-d drying shrinkage by 20% and increased flexural toughness by 40% for 1- and 7-d moist cured samples, respectively. However, the high porosity of LWS combined with limited external moist curing and 90 d of air drying impaired the transport properties. Such changes in concrete properties lead to increased I_{in} and reduced T_{onset} by up to 45%, and increased the relative duration between T_{onset} and T_{spike} by 160%

REFERENCES

[1] W. Shi, M. Najimi, B. Shafei, Reinforcement corrosion and transport of water and chloride ions in shrinkage-compensating cement concretes, Cement and Concrete Research 135 (2020) 106121.

[2] W.Y. W. J. Weiss, S.P. Shah, Factors Influencing Durability and Early-Age Cracking in High-Strength Concrete Structures, ACI Symposium Publication 189.

[3] A. Djerbi, S. Bonnet, A. Khelidj, V. Baroghel-Bouny, Influence of traversing crack on chloride diffusion into concrete, Cement and Concrete Research 38(6) (2008) 877-883.

[4] Z. Pan, Y. Zhu, D. Zhang, N. Chen, Y. Yang, X. Cai, Effect of expansive agents on the workability, crack resistance and durability of shrinkage-compensating concrete with low contents of fibers, Construction and Building Materials 259 (2020) 119768.

[5] I. Mehdipour, Characterization and performance of eco and crack-free high-performance concrete for sustainable infrastructure, Missouri University of Science and Technology, 2017.

[6] M. Valipour, K.H. Khayat, Coupled effect of shrinkage-mitigating admixtures and saturated lightweight sand on shrinkage of UHPC for overlay applications, Construction and Building Materials 184 (2018) 320-329.

[7] M. Li, J. Liu, Q. Tian, Y. Wang, W. Xu, Efficacy of internal curing combined with expansive agent in mitigating shrinkage deformation of concrete under variable temperature condition, Construction and Building Materials 145 (2017) 354-360.

[8] P.K. Mehta, Mechanism of expansion associated with ettringite formation, Cement and Concrete Research 3(1) (1973) 1-6.

[9] S. Nagataki, H. Gomi, Expansive admixtures (mainly ettringite), Cement and Concrete Composites 20(2) (1998) 163-170.

[10] S. Chatterji, Mechanism of expansion of concrete due to the presence of dead-burnt CaO and MgO, Cement and Concrete Research 25(1) (1995) 51-56.

[11] D.P. Bentz, K.A. Snyder, Protected paste volume in concrete: Extension to internal curing using saturated lightweight fine aggregate, Cement and Concrete Research 29(11) (1999) 1863-1867.

[12] D.D.D.R. JoAnn Browning, P. Benjamin, Lightweight Aggregate as Internal Curing Agent to Limit Concrete Shrinkage, ACI Materials Journal 108(6).

[13] R. Henkensiefken, D. Bentz, T. Nantung, J. Weiss, Volume change and cracking in internally cured mixtures made with saturated lightweight aggregate under sealed and unsealed conditions, Cement and Concrete Composites 31(7) (2009) 427-437.

[14] A. Bentur, S.-i. Igarashi, K. Kovler, Prevention of autogenous shrinkage in high-strength concrete by internal curing using wet lightweight aggregates, Cement and Concrete Research 31(11) (2001) 1587-1591.

[15] K. Kovler, O. Jensen, Internal curing of concrete, state-of-the-art Report of RILEM Technical Committee 196-ICC, RILEM Report, 2007.

[16] W. Hansen, Report on early-age cracking, Concrete International, 2011, pp. 48-51.

[17] G. Miroslaw, P.S. Surendra, Shrinkage Cracking of Fiber Reinforced Concrete, ACI Materials Journal 87(2).

[18] N. Flores Medina, G. Barluenga, F. Hernández-Olivares, Enhancement of durability of concrete composites containing natural pozzolans blended cement through the use of Polypropylene fibers, Composites Part B: Engineering 61 (2014) 214-221.

[19] M. Briffaut, F. Benboudjema, L. D’Aloia, Effect of fibres on early age cracking of concrete tunnel lining. Part I: Laboratory ring test, Tunnelling and Underground Space Technology 59 (2016) 215-220.

[20] V. Corinaldesi, A. Nardinocchi, J. Donnini, The influence of expansive agent on the performance of fibre reinforced cement-based composites, Construction and Building Materials 91 (2015) 171-179.

[21] W. Sun, H. Chen, X. Luo, H. Qian, The effect of hybrid fibers and expansive agent on the shrinkage and permeability of high-performance concrete, Cement and Concrete Research 31(4) (2001) 595-601.

[22] R. Gagné, Expansive agents, Science and Technology of Concrete Admixtures, Elsevier2016, pp. 441-456.

[23] D.P. Bentz, O.M. Jensen, Mitigation strategies for autogenous shrinkage cracking, Cement and Concrete Composites 26(6) (2004) 677-685.

[24] V. Lilkov, N. Djabarov, G. Bechev, K. Kolev, Properties and hydration products of lightweight and expansive cements Part I: Physical and mechanical properties, Cement and Concrete Research 29(10) (1999) 1635-1640.

[25] P. Carballosa, J.L. García Calvo, D. Revuelta, J.J. Sánchez, J.P. Gutiérrez, Influence of cement and expansive additive types in the performance of self-stressing and self-compacting concretes for structural elements, Construction and Building Materials 93 (2015) 223-229.

[26] J.L. García Calvo, D. Revuelta, P. Carballosa, J.P. Gutiérrez, Comparison between the performance of expansive SCC and expansive conventional concretes in different expansion and curing conditions, Construction and Building Materials 136 (2017) 277-285.

[27] M. Collepardi, A. Borsoi, S. Collepardi, J.J. Ogoumah Olagot, R. Troli, Effects of shrinkage reducing admixture in shrinkage compensating concrete under non-wet curing conditions, Cement and Concrete Composites 27(6) (2005) 704-708.

[28] C. ZHU, H. Li, B. WANG, Y. XIE, Crack Resistance of Internal Curing Shrinkage-Compensating Concrete, Journal of Building Materials (6) (2015) 22.

[29] G.R. de Sensale, A.F. Goncalves, Effects of Fine LWA and SAP as Internal Water Curing Agents, International Journal of Concrete Structures and Materials 8(3) (2014) 229-238.

[30] J. Liu, C. Shi, X. Ma, K.H. Khayat, J. Zhang, D. Wang, An overview on the effect of internal curing on shrinkage of high performance cement-based materials, Construction and Building Materials 146 (2017) 702-712.

[31] P.-C.A. Alejandro Duran-Herrera, P. Nikola, Effect of Saturated Lightweight Sand Substitution on Shrinkage in 0.35 w/b Concrete, ACI Materials Journal 104(1).

[32] L. Wu, N. Farzadnia, C. Shi, Z. Zhang, H. Wang, Autogenous shrinkage of high performance concrete: A review, Construction and Building Materials 149 (2017) 62-75.

[33] L. Yang, C. Shi, Z. Wu, Mitigation techniques for autogenous shrinkage of ultra-high-performance concrete – A review, Composites Part B: Engineering 178 (2019) 107456.

[34] P.H. Bischoff, Tension stiffening and cracking of steel fiber-reinforced concrete, Journal of Materials in Civil Engineering 15(2) (2003) 174-182.

[35] Q. Cao, R. Wang, J. Jia, C. Zhou, Z. Lin, A comparative study of combined treatments for enhanced early-age cracking control of self-consolidating concrete, Construction and Building Materials 248 (2020) 118473.

[36] H.A. He, W. Dong, Z.M. Wu, Study on Long-Term Expansive Deformation of Self-Stressing Concrete with Combined Restrictions of Steel Fibers and Steel Bar, Key Engineering Materials 452-453 (2011) 533-536.

[37] W. Shi, M. Najimi, B. Shafei, Chloride penetration in shrinkage-compensating cement concretes, Cement and Concrete Composites 113 (2020) 103656.

[38] T. Higuchi, M. Eguchi, M. Morioka, E. Sakai, Hydration and properties of expansive additive treated high temperature carbonation, Cement and Concrete Research 64 (2014) 11-16.

[39] L. Fan, W. Meng, L. Teng, K.H. Khayat, Effects of lightweight sand and steel fiber contents on the corrosion performance of steel rebar embedded in UHPC, Construction and Building Materials 238 (2020) 117709.

[40] H.A. Toutanji, Properties of polypropylene fiber reinforced silica fume expansive-cement concrete, Construction and Building Materials 13(4) (1999) 171-177.

[41] I. Mehdipour, K.H. Khayat, Elucidating the role of supplementary cementitious materials on shrinkage and restrained-shrinkage cracking of flowable eco-concrete, Journal of Materials in Civil Engineering 30(3) (2018) 04017308.

[42] K.H. Khayat, I. Mehdipour, Design and performance of crack-free environmentally friendly concrete, Missouri University of Science and Technology 2014.

[43] K.H. Khayat, F. Kassimi, P. Ghoddousi, Mixture Design and Testing of Fiber-Reinforced Self-Consolidating Concrete, ACI Materials Journal 111(2) (2014).

[44] W.Z. Taffese, E. Sistonen, Machine learning for durability and service-life assessment of reinforced concrete structures: Recent advances and future directions, Automation in Construction 77 (2017) 1-14.

[45] M.F. Montemor, A.M.P. Simões, M.G.S. Ferreira, Chloride-induced corrosion on reinforcing steel: from the fundamentals to the monitoring techniques, Cement and Concrete Composites 25(4) (2003) 491-502.

[46] R.E.M. Chun-Qing Li, Z. Jian-Jun, Analytical Model for Corrosion-Induced Crack Width in Reinforced Concrete Structures, ACI Structural Journal 103(4).

[47] L. Youping, E.W. Richard, Modeling the Time-to-Corrosion Cracking in Chloride Contaminated Reinforced Concrete Structures, ACI Materials Journal 95(6).

[48] C.G. Berrocal, I. Löfgren, K. Lundgren, L. Tang, Corrosion initiation in cracked fibre reinforced concrete: Influence of crack width, fibre type and loading conditions, Corrosion Science 98 (2015) 128-139.

[49] M. Otieno, M. Alexander, H. Beushausen, Corrosion propagation in cracked and uncracked concrete, Concrete Repairing Rehabilitation and Retrofitting II (2008) 157-158.

[50] V. Horsakulthai, K. Paopongpaiboon, Strength, chloride permeability and corrosion of coarse fly ash concrete with bagasse-rice husk-wood ash additive, American Journal of Applied Sciences 10(3) (2013) 239.

[51] E. Güneyisi, T. Özturan, M. Gesoğlu, A study on reinforcement corrosion and related properties of plain and blended cement concretes under different curing conditions, Cement and Concrete Composites 27(4) (2005) 449-461.

[52] S.A.O. Nair, S. Panda, M. Santhanam, G. Sant, N. Neithalath, A critical examination of the influence of material characteristics and extruder geometry on 3D printing of cementitious binders, Cement and Concrete Composites 112 (2020) 103671.

[53] J. Cai, B. Zhang, B. Xu, K.K.Y. Chan, G. Chowell, H. Tian, B. Xu, A maximum curvature method for estimating epidemic onset of seasonal influenza in Japan, BMC Infectious Diseases 19(1) (2019) 181.

[54] C. Hansson, A. Poursaee, A. Laurent, Macrocell and microcell corrosion of steel in ordinary Portland cement and high performance concretes, Cement and Concrete Research 36(11) (2006) 2098-2102.

[55] Y. Zhao, J. Yu, W. Jin, Damage analysis and cracking model of reinforced concrete structures with rebar corrosion, Corrosion Science 53(10) (2011) 3388-3397.

[56] W. Nguyen, J.F. Duncan, G. Jen, C.P. Ostertag, Influence of matrix cracking and hybrid fiber reinforcement on the corrosion initiation and propagation behaviors of reinforced concrete, Corrosion Science 140 (2018) 168-181.

[57] W. Meng, K. Khayat, Effects of saturated lightweight sand content on key characteristics of ultra-high-performance concrete, Cement and Concrete Research 101 (2017) 46-54.

[58] V. Corinaldesi, A. Nardinocchi, Mechanical characterization of Engineered Cement-based Composites prepared with hybrid fibres and expansive agent, Composites Part B: Engineering 98 (2016) 389-396.

[59] T. Aly, J.G. Sanjayan, F. Collins, Effect of polypropylene fibers on shrinkage and cracking of concretes, Materials and Structures 41(10) (2008) 1741-1753.

[60] J. Branston, S. Das, S.Y. Kenno, C. Taylor, Influence of basalt fibres on free and restrained plastic shrinkage, Cement and Concrete Composites 74 (2016) 182-190.

[61] I. Mehdipour, K.H. Khayat, Shrinkage Mitigating Strategies for Low Shrinkage Self-Consolidating Concrete, Washington DC, USA (2016) 783.

[62] D. Lockington, J. Parlange, Anomalous water absorption in porous materials, Journal of Physics D: Applied Physics 36(6) (2003) 760.

[63] N. Neithalath, Analysis of Moisture Transport in Mortars and Concrete Using Sorption-Diffusion Approach, ACI Materials Journal 103(3) (2006) 209-217.

[64] H.T. Cam, N. Neithalath, Moisture and ionic transport in concretes containing coarse limestone powder, Cement and Concrete Composites 32(7) (2010) 486-496.

[65] A.O.S. Solgaard, M. Geiker, C. Edvardsen, A. Küter, Observations on the electrical resistivity of steel fibre reinforced concrete, Materials and Structures 47(1) (2014) 335-350.

[66] O.B. Isgor, A.G. Razaqpur, Modelling steel corrosion in concrete structures, Materials and Structures 39(3) (2006) 291-302.

[67] G. Loreto, M. Di Benedetti, R. Iovino, A. Nanni, M. Gonzalez, Evaluation of corrosion effect in reinforced concrete by chloride exposure, SPIE2011.

[68] K. Hornbostel, B. Elsener, U.M. Angst, C.K. Larsen, M.R. Geiker, Limitations of the use of concrete bulk resistivity as an indicator for the rate of chloride-induced macro-cell corrosion, Structural Concrete 18(2) (2017) 326-333.

[69] K. Hornbostel, U.M. Angst, B. Elsener, C.K. Larsen, M.R. Geiker, On the limitations of predicting the ohmic resistance in a macro-cell in mortar from bulk resistivity measurements, Cement and Concrete Research 76 (2015) 147-158.

[70] K. Hornbostel, U.M. Angst, B. Elsener, C.K. Larsen, M.R. Geiker, Influence of mortar resistivity on the rate-limiting step of chloride-induced macro-cell corrosion of reinforcing steel, Corrosion Science 110 (2016) 46-56.

SECTION

2. CONCLUSIONS AND RECOMMENDATIONS

2.1. SUMMARY AND CONCLUSIONS OF DISSERTATION WORK

The main objective of this dissertation is to develop 3D printable shrinkage-resistant mortar mixtures. To this end, the research work contained in this dissertation was carried out to identify the key material properties that effect the printability and their suitable ranges for 3DP using a ram extruder setup. Furthermore, the suitability of different shrinkage mitigating materials such as the expansive agent and internal curing agents commonly used in conventional concrete construction for 3DP application is explored. The work presented in this dissertation contributes to facilitating the implementation of 3DP technology in concrete construction and realize its potential benefits.

In Paper I, a comprehensive review of the literature on individual processing stages involved in extrusion-based 3DP process (pumping and extrusion) is carried out to delineates the effect of flow behavior and process-induced variations on shape stability. This paper provides insight into key material processing parameters that govern the material flow behavior during pumping and extrusion and highlights the dependency of the extruded material shape stability on the material flow behavior during 3DP. The key findings from Paper I are summarized below:

- The flow behavior of cement-based materials during pumping for 3DP depends on the rheological properties and the amount of paste that is available to form the lubrication layer as well as the pipeline diameter and pumping rate. The cement-based materials for 3DP are typically designed to have higher amount of paste and use supplementary cementitious materials to enhance the particle packing density, low water-to-binder ratio to improve shape stability, smaller aggregates and low aggregate content to minimize blockage within the extruder. The typical composition of printable mixtures indicates a low chance of lubrication layer formation, or formation of relatively thin layer and a shearing flow behavior (as opposed to plug flow behavior) during pumping. Limited emphasis is placed in the 3DP literature to assess the pumpability of the printable mixtures.

- The extrudability of the print material is a function of material rheology, rate of fluid filtration during extrusion, particle packing density, aggregate volume fraction, and maximum aggregate size, as well as the extrusion parameters i.e., extrusion speed and dimensions of the extruder. In the absence of fluid filtration and consolidation, the extrusion force is dependent on the extent of shearing in the material. The extent of shearing can be quantified using Bingham number which is a function of yield stress, viscosity, extruder barrel diameter, and extrusion speed. At high values of Bingham number typically > 100, low shearing occurs in the material and low extrusion force is needed i.e., high extrudability. For a given material, high values of Bingham number occur at low values of extrusion speed. The use of low extrusion speed increases the possibility of fluid filtration which can lead to phase separation in the extruder, increase in extrusion force, decrease in shape stability of the extruded material, and blockage during extrusion. The rate of fluid filtration during extrusion is a key parameter that influences material extrudability. Therefore, during the selection of cement-based materials for 3DP, special attention needs to be placed on fluid filtration characteristics. The optimization of print materials in the literature is mainly done to meet the yield stress and viscosity requirements with limited emphasis on fluid filtration characteristics.

- The shearing of the print material during pumping can change rheology and fluid filtration characteristics of the material, which can influence the flow behavior during extrusion. The shearing, filtration and consolidation during extrusion can further alter the static yield stress, modulus, and the rate of structural buildup of the print material, which can result in poor shape stability of the printed elements. Ensuring proper shape stability requires accurate assessment of process-induced variations in the material properties and adjusting the processing parameters, such as pumping rate and extrusion speed based on the anticipated changes in material properties.

In Paper II, the key findings in Paper I pertaining to the importance of assessing rheology and fluid filtration characteristics to assess extrudability is utilized to develop 3D printable mortar mixtures. The rheology and fluid filtration characteristics of mortar mixtures are varied by changing the water-to-cement ratio, superplasticizer dosage, and welan gum content. The influence of these properties on extrudability is evaluated. The fluid filtration is measured in terms of desorptivity, while the extrudability is assessed as the maximum force needed during ram extrusion. The rheology and fluid filtration properties of the material exhibited an opposing influence on extrudability. A printability window i.e., suitable ranges of material properties is proposed for the extrusion of mortar based on the rheology and fluid filtration characteristics. The key findings from Paper II are summarized below:

- The printability window for successful extrusion-based 3DP is identified as region where yield stress ranges from 100- 470 Pa, plastic viscosity from 10-60 Pa.s, and desorptivity is lower than $3x10^{-3}$ $s^{-0.5}$ when measured at an overhead pressure of 120 kPa. The printability window is developed using ram extruder with nozzle size of 9 mm, extrusion speed of 2.5 mm/s, and load capacity of 135 N.
- For the investigated rheological parameters and fluid filtration characteristics, the influence of viscosity on the extrudability is insignificant compared to that of yield stress and desorptivity. Additionally, an improvement in extrudability is observed by reducing yield stress and desorptivity. However, a lower limit of 100 Pa for yield stress is needed to ensure shape stability of extrudable layers extruded using 9 mm nozzle.
- The decrease in water-to-cement ratio from 0.35 to 0.25 improved extrudability due to the change in the material flow behavior during extrusion from frictional plastic to visco-plastic. The increase in superplasticizer dosage from 0.09% to 0.11% improved extrudability due to the reduction in the material rheological properties. However, further increase in superplasticizer to 0.22% and 0.43%) lowered yield stress and reduced shape stability of extruded layers.
- The use of welan gum drastically reduced the desorptivity and enabled the extrusion of print material with high yield stress. Overall, the use of WG enabled development of print materials that are most suitable for extrusion-based 3DP

(i.e., higher yield stress needed for shape stability and lower fluid filtration needed to homogeneous extrusion).

In Paper III, the printability window developed in Paper II is used a guideline for the selection of dosages of shrinkage mitigation materials (expansive agent, pre-saturated lightweight sand, superabsorbent polymers of particles sizes 35 and 850 µm, and shrinkage reducing admixture) and welan gum for the development of 3D printable mortar mixtures. In addition to printability, the plastic and drying shrinkage of the samples is evaluated by subjecting the mixtures specimens to drying i.e., evaporation rate of 1.6 $kg/m^2 \cdot h$. The plastic shrinkage is assessed in terms of the mass loss of the test samples when exposed drying. The influence of the curing condition (lime-saturated moist curing vs. drying) and time on the compressive strength of the mixtures is also evaluated. The exposure drying condition is selected to accelerate the drying process and to simulate the conditions during 3DP process, where the printed elements are exposed to the environment in the plastic state and the conventional moist curing is limited. The key findings from Paper III are summarized below:

- The combined use of 5% expansive agent with 12% pre-saturated lightweight sand enabled development of printable mixtures and is effective at mitigating autogenous shrinkage and reducing the drying shrinkage strain by 21% measured after 28 d. Further increase in lightweight sand content to 25% caused fluid filtration during the ram extrusion and consequently causing the blockage with the extruder.
- The increase in superabsorbent polymer size from 35 to 850 µm lead to increase in absorption time and delay in absorption-desorption kinetics. The slow

desorption of larger sizer polymers at 0.3% dosage enables successful internal curing of mortar mixtures and reduced mass loss in the plastic state by 25% and autogenous shrinkage by 370%. The superabsorbent polymers are effective at reducing the fluid filtration during extrusion; however, the absorption-desorption kinetics needs to be tailored and a slower absorption and desorption is preferred to ensure shape stability and efficient internal curing.

- The use of 2% shrinkage reducing admixture significantly improved mass loss resistance in plastic state and drying shrinkage resistance by 21% and 31%, respectively. The use of shrinkage reducing admixture negatively impacted the compressive strength, hydration kinetics, and total degree of hydration.
- The improvement in water retention with the addition of 0.6% welan gum enabled reducing mass loss in plastic state by 17%. The findings from Paper II and Paper III, suggest that the use of welan gum can enable development of print materials that are most suitable for extrusion-based 3D i.e., high yield stress, low desorptivity, and increased resistance to drying in plastic sate.

One of the concerns with the use of shrinkage mitigating materials for the development of printable mixtures is that that influence of these materials on durability aspects of cement-based materials is not well known. To address this issue, in Paper IV, the influence of shrinkage mitigation materials (expansive agent and pre-saturated lightweight sand), steel and synthetic fibers on chloride-induced corrosion of rebars embedded in concrete prismatic samples with different cover depths is investigated. It should be noted that the investigation carried out in this paper is done on non-3D printable fiber reinforced concrete mixtures. However, the findings from this paper provide an insight into the suitability of these materials to improve the long-term performance of 3D printed elements. The concrete samples are subjected to limited moist curing duration of 1 or 7 d followed by 90 d of air drying prior to corrosion assessment,. Transport and mechanical properties of concrete subjected to same curing conditions are investigated. Such curing conditions are selected to allow for drying shrinkage of test samples and evaluate the impact of shrinkage mitigating provided by shrinkage mitigation materials and fibers on corrosion resistance of embedded rebars. The key findings from Paper IV that provide an insight on the expected performance of 3D printed elements are summarized below:

- The use of steel fibers, expansive agent and lightweight can reduce drying shrinkage and increase cracking resistance; however, such materials can have a detrimental effect on transport properties under the limited moist curing of 1 d, leading to lower corrosion resistance. On the other hand, the use of synthetic fibers is less effective at shrinkage mitigation and cracking resistance, yet these fibers show no detrimental effect on transport properties and corrosion resistance.
- For all the investigated mixtures, the increase in moist curing duration from 1 to 7 d is effective at reducing 90-d drying shrinkage water absorption, and electrical conductivity, and improving flexural strength and toughness. The enhancement in transport and mechanical properties lead to improved corrosion resistance and delayed the corrosion-associated cracking in concrete cover.
- The use of 25% lightweight sand is effective at reducing shrinkage and improving flexural toughness of mixtures at 1 and 7 d of moist curing. However, the high porosity of lightweight sand combined with limited external moist curing

followed by 90 d of air drying impaired the transport properties and lead to decreased corrosion resistance and early onset of cracking in concrete cover. The findings in Paper III suggest that the usage of lightweight sand at high dosages can increase desorptivity and lead to blockage in the extruder. While the findings in Paper IV suggest that LWS is effective at providing internal but can have detrimental effect on the transport properties. Therefore, more studies are warranted to determine an optimum lightweight sand content before its use in 3DP applications.

2.2. RECOMMENDATIONS FOR FUTURE WORK

The implementation of 3DP technology in concrete construction is relatively new and therefore significant work in terms of understanding the influence of different material constituents on the printability and performance of printed element performance as well as development of test methods for the assessment of material performance is needed. Based on the literature review and experimental work carried out in this dissertation, following future research is recommended to bridge the gaps in existing research and for 3DP to be a viable alternative to conventional concrete casting technique.

- The successful 3DP of cement-based materials requires the selection of print materials and processing parameters that can facilitate the formation of lubrication layer during pumping, while minimizing the structural breakdown and phase separation during pumping and extrusion. This requires development of suitable test methods to assess the properties of the lubrication layer of print materials.

The interface rheometers available for the assessment of lubrication layer properties typically do not measure properties for cement-based materials with high yield stress which are used for 3DP.

- The print material can undergo changes in material composition and rheological properties during pumping and extrusion that can affect shape stability of extruded material. Systems to evaluate process-induced variations in key properties need to be developed to improve the robustness of 3DP process. Numerical and analytical models that take into account the effect of processing parameters, material properties at the start of printing, as well as the process-induced changes, need to be developed to ensure a steady and continuous flow of the materials during pumping and extrusion, and to prevent failure of the printed elements.
- The printability window proposed in Paper II provides practical guideline for material properties during the selection and optimization of mixtures for extrusion-based 3DP. This approach can be further expanded by considering the variation in extrusion parameters such as extrusion speed and dimensions of the nozzle. Furthermore, statistical modelling can be carried out to develop models that can predict the force needed for extrusion given the extrusion parameters used, rheology and fluid filtration characteristics of the print material.
- The suitability of shrinkage mitigating materials for 3DP applications is demonstrated in Paper III by assessing their effect on printability and shrinkage performance of the material. This study can be further extended to assess the influence of these materials on the shrinkage performance 3D printed elements,

interlayer bond strength between the successive layers and its microstructure. Paper IV demonstrated that the shrinkage mitigating materials can improve the shrinkage resistance but can have detrimental effect on the transport properties and corrosion resistance of concrete mixtures when the moist curing is limited. Therefore, more studies on the influence of the shrinkage mitigating materials on long-term performance of 3D printed elements is warranted before their use in 3DP.

APPENDIX

PEER-REVIEWED JOURNAL ARTICLES

Published

[1] **Vallurupalli, K.**, Farzadnia, N. and Khayat, K.H., 2021. Effect of flow behavior and process-induced variations on shape stability of 3D printed elements–A review. *Cement and Concrete Composites*, *118*, 103952.

[2] **Vallurupalli, K.**, Meng, W., Liu, J. and Khayat, K.H. (2020). Effect of graphene oxide on rheology, hydration and strength development of cement paste. *Construction and Building Materials*, *265*, 120311.

[3] Khayat, K. H., Meng, W., **Vallurupalli, K.**, and Teng, L. (2019). Rheological properties of ultra-high-performance concrete - An overview. *Cement and Concrete Research*, *124*, 105828.

Submitted

[4] **Vallurupalli, K.**, Farzadnia, N., and Khayat, K.H. Effect of shrinkage mitigating materials on chloride-induced corrosion resistance of fiber-reinforced concrete. *Cement and Concrete Composites* (under review).

[5] **Vallurupalli, K.**, Libre, N.A., and Khayat, K.H. Characterization of print material extrudability using rheology and desorptivity. *ACI Journal* (under review).

Under preparation

[6] **Vallurupalli, K** and Khayat, K.H. Effect of shrinkage mitigating materials on printability and shrinkage resistance of 3D printable mortar.

BIBLIOGRAPHY

[1] M.S. Khan, F. Sanchez, H. Zhou, 3-D Printing of Concrete: Beyond Horizons, Cement and Concrete Research 133 (2020) 106070.

[2] D.D. Camacho, P. Clayton, W.J. O'Brien, C. Seepersad, M. Juenger, R. Ferron, S. Salamone, Applications of Additive Manufacturing in the Construction Industry–a Forward-Looking Review, Automation in construction 89 (2018) 110-119.

[3] R.A. Buswell, W.R. Leal de Silva, S.Z. Jones, J. Dirrenberger, 3d Printing Using Concrete Extrusion: A Roadmap for Research, Cement and Concrete Research 112 (2018) 37-49.

[4] National Ready Mixed Concrete Association. https://www.irmca.org/file/226/Ready-Mixed-Concrete-Production-Statistics-Updated-Through-September-2016.pdf. (Accessed January 16 2020).

[5] National Precast Concrete Association. https://precast.org/. (Accessed January 16 2020).

[6] N. Hack, W.V. Lauer, Mesh-Mould: Robotically Fabricated Spatial Meshes as Reinforced Concrete Formwork, Architectural Design 84(3) (2014) 44-53.

[7] W.F. Chen, J.Y.R. Liew, The Civil Engineering Handbook, 2 ed., CRC Press LLC, New York, 2003.

[8] J. Zhang, J. Wang, S. Dong, X. Yu, B. Han, A Review of the Current Progress and Application of 3d Printed Concrete, Composites Part A: Applied Science and Manufacturing 125 (2019) 105533.

[9] R.A. Buswell, W.R.L. da Silva, F.P. Bos, H.R. Schipper, D. Lowke, N. Hack, H. Kloft, V.Mechtcherine, T. Wangler, N. Roussel, A Process Classification Framework for Defining and Describing Digital Fabrication with Concrete, Cement and Concrete Research 134 (2020) 106068.

[10] A. Bhardwaj, S.Z. Jones, N. Kalantar, Z. Pei, J. Vickers, T. Wangler, P. Zavattieri, N. Zou, Additive Manufacturing Processes for Infrastructure Construction: A Review, International Manufacturing Science and Engineering Conference, American Society of Mechanical Engineers, 2019, p. V001T01A005.

[11] V. Mechtcherine, F.P. Bos, A. Perrot, W.L. da Silva, V. Nerella, S. Fataei, R.J. Wolfs, M. Sonebi, N. Roussel, Extrusion-Based Additive Manufacturing with Cement-Based Materials–Production Steps, Processes, and Their Underlying Physics: A Review, Cement and Concrete Research 132 (2020) 106037.

[12] B. Khoshnevis, D. Hwang, K.-T. Yao, Z. Yeh, Mega-Scale Fabrication by Contour Crafting, International Journal of Industrial and Systems Engineering 1(3) (2006) 301-320.

[13] T.T. Le, S.A. Austin, S. Lim, R.A. Buswell, A.G. Gibb, T. Thorpe, Mix Design and Fresh Properties for High-Performance Printing Concrete, Materials and structures 45(8) (2012) 1221-1232.

[14] V. Nerella, M. Näther, A. Iqbal, M. Butler, V. Mechtcherine, Inline Quantification of Extrudability of Cementitious Materials for Digital Construction, Cement and Concrete Composites 95 (2019) 260-270.

[15] A. Perrot, D. Rangeard, V.N. Nerella, V. Mechtcherine, Extrusion of Cement-Based Materials-an Overview, RILEM Technical Letters 3 (2018) 91-97.

[16] I. Aydin, F.R. Biglari, B.J. Briscoe, C.J. Lawrence, M.J. Adams, Physical and Numerical Modelling of Ram Extrusion of Paste Materials: Conical Die Entry Case, Computational Materials Science 18(2) (2000) 141-155.

[17] H. Alghamdi, S.A.O. Nair, N. Neithalath, Insights into Material Design, Extrusion Rheology, and Properties of 3d-Printable Alkali-Activated Fly Ash-Based Binders, Materials & Design 167 (2019) 107634.

[18] A.S.J. Suiker, R.J.M. Wolfs, S.M. Lucas, T.A.M. Salet, Elastic Buckling and Plastic Collapse During 3d Concrete Printing, Cement and Concrete Research 135 (2020) 106016.

[19] S. Ketel, G. Falzone, B. Wang, N. Washburn, G. Sant, A Printability Index for Linking Slurry Rheology to the Geometrical Attributes of 3d-Printed Components, Cement and Concrete Composites (2018).

[20] Y.W.D. Tay, Y. Qian, M.J. Tan, Printability Region for 3d Concrete Printing Using Slump and Slump Flow Test, Composites Part B: Engineering 174 (2019) 106968.

[21] T.T. Le, S.A. Austin, S. Lim, R.A. Buswell, R. Law, A.G. Gibb, T. Thorpe, Hardened Properties of High-Performance Printing Concrete, Cement and Concrete Research 42(3) (2012) 558-566.

[22] Y. Zhang, Y. Zhang, G. Liu, Y. Yang, M. Wu, B. Pang, Fresh Properties of a Novel 3d Printing Concrete Ink, Construction and Building Materials 174 (2018) 263-271.

[23] Z. Ding, X. Wang, J. Sanjayan, P. Zou, Z.-K. Ding, A Feasibility Study on Hpmc-Improved Sulphoaluminate Cement for 3d Printing, Materials 11(12) (2018) 2415.

[24] N. Khalil, G. Aouad, K. El Cheikh, S. Rémond, Use of Calcium Sulfoaluminate Cements for Setting Control of 3d-Printing Mortars, Construction and Building Materials 157 (2017) 382-391

[25] Z. Jianchao, T. Zhang, M. Faried, C. Wengang, 3d Printing Cement Based Ink, and It's Application within the Construction Industry, MATEC Web of Conferences, EDP Sciences, 2017, p. 02003.

[26] J. Ingaglio, J. Fox, C.J. Naito, P. Bocchini, Material Characteristics of Binder Jet 3d Printed Hydrated Csa Cement with the Addition of Fine Aggregates, Construction and Building Materials 206 (2019) 494-503.

[27] M. Chen, X. Guo, Y. Zheng, L. Li, Z. Yan, P. Zhao, L. Lu, X. Cheng, Effect of Tartaric Acid on the Printable, Rheological and Mechanical Properties of 3d Printing Sulphoaluminate Cement Paste, Materials 11(12) (2018) 2417.

[28] G. Ma, Z. Li, L. Wang, Printable Properties of Cementitious Material Containing Copper Tailings for Extrusion Based 3d Printing, Construction and Building Materials 162 (2018) 613-627.

[29] Z. Liu, M. Li, Y. Weng, T.N. Wong, M.J. Tan, Mixture Design Approach to Optimize the Rheological Properties of the Material Used in 3d Cementitious Material Printing, Construction and Building Materials 198 (2019) 245-255.

[30] Y. Weng, M. Li, M.J. Tan, S. Qian, Design 3d Printing Cementitious Materials Via Fuller Thompson Theory and Marson-Percy Model, Construction and Building Materials 163 (2018) 600-610.

[31] G. Ma, L. Wang, Y. Ju, State-of-the-Art of 3d Printing Technology of Cementitious Material—an Emerging Technique for Construction, Science China Technological Sciences (2017) 1-21.

[32] V.N. Nerella, S. Hempel, V. Mechtcherine, Effects of Layer-Interface Properties on Mechanical Performance of Concrete Elements Produced by Extrusion-Based 3d-Printing, Construction and Building Materials 205 (2019) 586-601.

[33] D.G. Soltan, V.C. Li, A Self-Reinforced Cementitious Composite for Building-Scale 3d Printing, Cement and Concrete Composites 90 (2018) 1-13.

[34] Y.W. Tay, B. Panda, S.C. Paul, M.J. Tan, S.Z. Qian, K.F. Leong, C.K. Chua, Processing and Properties of Construction Materials for 3d Printing, Materials Science Forum, Trans Tech Publ, 2016, pp. 177-181.

[35] T.S. Rushing, G. Al-Chaar, B.A. Eick, J. Burroughs, J. Shannon, L. Barna, M. Case, Investigation of Concrete Mixtures for Additive Construction, Rapid Prototyping Journal 23(1) (2017) 74-80.

[36] P. Shakor, J. Sanjayan, A. Nazari, S. Nejadi, Modified 3d Printed Powder to Cement-Based Material and Mechanical Properties of Cement Scaffold Used in 3d Printing, Construction and Building Materials 138 (2017) 398-409.

[37] M. Hambach, D. Volkmer, Properties of 3d-Printed Fiber-Reinforced Portland Cement Paste, Cement and Concrete Composites 79 (2017) 62-70.

[38] R. Lediga, D. Kruger, Optimizing Concrete Mix Design for Application in 3d Printing Technology for the Construction Industry, Solid State Phenomena 263 (2017).

[39] S. Lim, T. Le, J. Webster, R. Buswell, A. Austin, A. Gibb, T. Thorpe, Fabricating Construction Components Using Layered Manufacturing Technology, Global Innovation in Construction Conference, 2009, pp. 512-520.

[40] D. Marchon, S. Kawashima, H. Bessaies-Bey, S. Mantellato, S. Ng, Hydration and Rheology Control of Concrete for Digital Fabrication: Potential Admixtures and Cement Chemistry, Cement and Concrete Research (2018).

[41] B. Zareiyan, B. Khoshnevis, Effects of Interlocking on Interlayer Adhesion and Strength of Structures in 3d Printing of Concrete, Automation in construction 83 (2017) 212-221.

[42] O.A. Hisseine, N. Basic, A.F. Omran, A. Tagnit-Hamou, Feasibility of Using Cellulose Filaments as a Viscosity Modifying Agent in Self-Consolidating Concrete, Cement and Concrete Composites 94 (2018) 327-340.

[43] B. Panda, N.A. Noor Mohamed, S.C. Paul, G. Bhagath Singh, M.J. Tan, B. Šavija, The Effect of Material Fresh Properties and Process Parameters on Buildability and Interlayer Adhesion of 3d Printed Concrete, Materials 12(13) (2019) 2149.

[44] S. Ma, S. Kawashima, Rheological and Water Transport Properties of Cement Pastes Modified with Diutan Gum and Attapulgite/Palygorskite Nanoclays for 3d Concrete Printing, RILEM International Conference on Concrete and Digital Fabrication, Springer, 2018, pp. 61-69.

[45] D. Asprone, F. Auricchio, C. Menna, V. Mercuri, 3d Printing of Reinforced Concrete Elements: Technology and Design Approach, Construction and Building Materials 165 (2018) 218-231.

[46] S.C. Paul, Y.W.D. Tay, B. Panda, M.J. Tan, Fresh and Hardened Properties of 3d Printable Cementitious Materials for Building and Construction, Archives of Civil and Mechanical Engineering 18(1) (2018) 311-319.

[47] Z. Malaeb, H. Hachem, A. Tourbah, T. Maalouf, N. Zarwi, F. Hamzeh, 3d Concrete Printing: Machine and Mix Design, International Journal of Civil Engineering 6(6) (2015) 14-22.

[48] S. Al-Qutaifi, A. Nazari, A. Bagheri, Mechanical Properties of Layered Geopolymer Structures Applicable in Concrete 3d-Printing, Construction and Building Materials 176 (2018) 690-699.

[49] K. El Cheikh, S. Rémond, N. Khalil, G. Aouad, Numerical and Experimental Studies of Aggregate Blocking in Mortar Extrusion, Construction and Building Materials 145 (2017) 452-463.

[50] D.P. Bentz, O.M. Jensen, Mitigation Strategies for Autogenous Shrinkage Cracking, Cement and Concrete Composites 26(6) (2004) 677-685.

[51] P. Aıtcin, The Durability Characteristics of High Performance Concrete: A Review, Cement and Concrete Composites 25(4-5) (2003) 409-420.

[52] J.G. Sanjayan, B. Nematollahi, M. Xia, T. Marchment, Effect of Surface Moisture on Inter-Layer Strength of 3d Printed Concrete, Construction and Building Materials 172 (2018) 468-475.

[53] M.K. Mohan, A. Rahul, K. Van Tittelboom, G. De Schutter, Extrusion-Based Concrete 3d Printing from a Material Perspective: A State-of-the-Art Review, Cement and Concrete Composites (2020) 103855.

[54] Y.W.D. Tay, G.H.A. Ting, Y. Qian, B. Panda, L. He, M.J. Tan, Time Gap Effect on Bond Strength of 3d-Printed Concrete, Virtual and Physical Prototyping 14(1) (2019) 104-113.

[55] A.S.J. Suiker, Mechanical Performance of Wall Structures in 3d Printing Processes: Theory, Design Tools and Experiments, International Journal of Mechanical Sciences 137 (2018) 145-170.

[56] N. Roussel, Rheological Requirements for Printable Concretes, Cement and Concrete Research (2018).

[57] M. Choi, K. Park, T. Oh, Viscoelastic Properties of Fresh Cement Paste to Study the Flow Behavior, International Journal of Concrete Structures and Materials 10(3) (2016) 65-74.

[58] J. Yammine, M. Chaouche, M. Guerinet, M. Moranville, N. Roussel, From Ordinary Rhelogy Concrete to Self Compacting Concrete: A Transition between Frictional and Hydrodynamic Interactions, Cement and Concrete Research 38(7) (2008) 890-896.

[59] N. Roussel, A. Lemaître, R.J. Flatt, P. Coussot, Steady State Flow of Cement Suspensions: A Micromechanical State of the Art, Cement and Concrete Research 40(1) (2010) 77-84.

[60] T. Lecompte, A. Perrot, V. Picandet, H. Bellegou, S. Amziane, Cement-Based Mixes: Shearing Properties and Pore Pressure, Cement and Concrete Research 42(1) (2012) 139-147.

[61] D. Kaplan, L. François de, T. Sedran, Avoidance of Blockages in Concrete Pumping Process, ACI materials journal 102(3) (2005) 183.

[62] G. De Schutter, D. Feys, Pumping of Fresh Concrete: Insights and Challenges, RILEM Technical Letters 1 (2016) 76-80.

[63] D.B. Roger, B.B. Phillip, Tests to Establish Concrete Pumpability, ACI Journal Proceedings 74(5).

[64] D. Feys, K.H. Khayat, R. Khatib, How Do Concrete Rheology, Tribology, Flow Rate and Pipe Radius Influence Pumping Pressure?, Cement and Concrete Composites 66 (2016) 38-46.

[65] D. Feys, K.H. Khayat, A. Perez-Schell, R. Khatib, Prediction of Pumping Pressure by Means of New Tribometer for Highly-Workable Concrete, Cement and Concrete Composites 57 (2015) 102-115.

[66] M. Choi, N. Roussel, Y. Kim, J. Kim, Lubrication Layer Properties During Concrete Pumping, Cement and Concrete Research 45 (2013) 69-78.

[67] D. Feys, How Much Is Bulk Concrete Sheared During Pumping?, Construction and Building Materials 223 (2019) 341-351.

[68] T. Van Pham, E. Mitsoulis, Viscoplastic Flows in Ducts, The Canadian Journal of Chemical Engineering 76(1) (1998) 120-125.

[69] A. Perrot, D. Rangeard, Y. Mélinge, Prediction of the Ram Extrusion Force of Cement-Based Materials, Applied Rheology 24(5) (2014) 34-40.

[70] Z. Toutou, N. Roussel, C. Lanos, The Squeezing Test: A Tool to Identify Firm Cement-Based Material's Rheological Behaviour and Evaluate Their Extrusion Ability, Cement and Concrete Research 35(10) (2005) 1891-1899.

[71] R.A. Basterfield, C.J. Lawrence, M.J. Adams, On the Interpretation of Orifice Extrusion Data for Viscoplastic Materials, Chemical Engineering Science 60(10) (2005) 2599-2607.

[72] A. Perrot, Y. Mélinge, D. Rangeard, F. Micaelli, P. Estellé, C. Lanos, Use of Ram Extruder as a Combined Rheo-Tribometer to Study the Behaviour of High Yield Stress Fluids at Low Strain Rate, Rheologica Acta 51(8) (2012) 743-754.

[73] A. Perrot, C. Lanos, Y. Melinge, P. Estellé, Mortar Physical Properties Evolution in Extrusion Flow, Rheologica Acta 46(8) (2007) 1065-1073.

[74] H. Khelifi, A. Perrot, T. Lecompte, D. Rangeard, G. Ausias, Prediction of Extrusion Load and Liquid Phase Filtration During Ram Extrusion of High Solid Volume Fraction Pastes, Powder Technology 249 (2013) 258-268.

[75] F.A. Cardoso, V.M. John, R.G. Pileggi, Rheological Behavior of Mortars under Different Squeezing Rates, Cement and Concrete Research 39(9) (2009) 748-753.

[76] C. Ince, M.A. Carter, M.A. Wilson, N.C. Collier, A. El-Turki, R.J. Ball, G.C. Allen, Factors Affecting the Water Retaining Characteristics of Lime and Cement Mortars in the Freshly-Mixed State, Materials and structures 44(2) (2011) 509-516.

[77] A.V. Rahul, A. Sharma, M. Santhanam, A Desorptivity-Based Approach for the Assessment of Phase Separation During Extrusion of Cementitious Materials, Cement and Concrete Composites 108 (2020) 103546.

[78] T. Wangler, E. Lloret, L. Reiter, N. Hack, F. Gramazio, M. Kohler, M. Bernhard, B. Dillenburger, J. Buchli, N. Roussel, Digital Concrete: Opportunities and Challenges, RILEM Technical Letters 1 (2016) 67-75.

[79] M. Bellotto, Cement Paste Prior to Setting: A Rheological Approach, Cement and Concrete Research 52 (2013) 161-168.

[80] R.J. Flatt, P. Bowen, Yodel: A Yield Stress Model for Suspensions, Journal of the American Ceramic Society 89(4) (2006) 1244-1256.

[81] N. Roussel, A Thixotropy Model for Fresh Fluid Concretes: Theory, Validation and Applications, Cement and Concrete Research 36(10) (2006) 1797-1806.

[82] J.E. Wallevik, Rheological Properties of Cement Paste: Thixotropic Behavior and Structural Breakdown, Cement and Concrete Research 39(1) (2009) 14-29.

[83] P. Lura, B. Pease, G.B. Mazzotta, F. Rajabipour, J. Weiss, Influence of Shrinkage-Reducing Admixtures on Development of Plastic Shrinkage Cracks, ACI materials journal 104(2) (2007) 187-194.

[84] M.D. Cohen, J. Olek, W.L. Dolch, Mechanism of Plastic Shrinkage Cracking in Portland Cement and Portland Cement-Silica Fume Paste and Mortar, Cement and Concrete Research 20(1) (1990) 103-119.

[85] F.H. Wittmann, On the Action of Capillary Pressure in Fresh Concrete, Cement and Concrete Research 6(1) (1976) 49-56.

[86] C. Schröfl, V.N. Nerella, V. Mechtcherine, Capillary Water Intake by 3d-Printed Concrete Visualised and Quantified by Neutron Radiography, RILEM International Conference on Concrete and Digital Fabrication, Springer, 2018, pp. 217-224.

[87] R. De Coensel, Printability and Early Age Shrinkage of Cementitious.

[88] Z. Pan, Y. Zhu, D. Zhang, N. Chen, Y. Yang, X. Cai, Effect of Expansive Agents on the Workability, Crack Resistance and Durability of Shrinkage-Compensating Concrete with Low Contents of Fibers, Construction and Building Materials 259 (2020) 119768.

[89] S. Chatterji, Mechanism of Expansion of Concrete Due to the Presence of Dead-Burnt Cao and Mgo, Cement and Concrete Research 25(1) (1995) 51-56.

[90] K.H. Khayat, W. Meng, M. Valipour, M. Hopkins, Use of Lightweight Sand for Internal Curing to Improve Performance of Concrete Infrastructure, Missouri. Department of Transportation. Construction and Materials Division, 2018.

[91] V. Mechtcherine, M. Wyrzykowski, C. Schröfl, D. Snoeck, P. Lura, N. De Belie, A. Mignon, S. Van Vlierberghe, A.J. Klemm, F.C. Almeida, Application of Super Absorbent Polymers (Sap) in Concrete Construction—Update of Rilem State-of-the-Art Report, Materials and structures 54(2) (2021) 1-20.

[92] D.P. Bentz, M.R. Geiker, K.K. Hansen, Shrinkage-Reducing Admixtures and Early-Age Desiccation in Cement Pastes and Mortars, Cement and Concrete Research 31(7) (2001) 1075-1085.

[93] V. Corinaldesi, A. Nardinocchi, J. Donnini, The Influence of Expansive Agent on the Performance of Fibre Reinforced Cement-Based Composites, Construction and Building Materials 91 (2015) 171-179.

[94] W. Sun, H. Chen, X. Luo, H. Qian, The Effect of Hybrid Fibers and Expansive Agent on the Shrinkage and Permeability of High-Performance Concrete, Cement and Concrete Research 31(4) (2001) 595-601.

[95] M. Valipour, K.H. Khayat, Coupled Effect of Shrinkage-Mitigating Admixtures and Saturated Lightweight Sand on Shrinkage of Uhpc for Overlay Applications, Construction and Building Materials 184 (2018) 320-329.

[96] J. Liu, N. Farzadnia, C. Shi, X. Ma, Shrinkage and Strength Development of Uhsc Incorporating a Hybrid System of Sap and Sra, Cement and Concrete Composites 97 (2019) 175-189.

[97] M.F. Montemor, A.M.P. Simões, M.G.S. Ferreira, Chloride-Induced Corrosion on Reinforcing Steel: From the Fundamentals to the Monitoring Techniques, Cement and Concrete Composites 25(4) (2003) 491-502.

[98] W.Z. Taffese, E. Sistonen, Machine Learning for Durability and Service-Life Assessment of Reinforced Concrete Structures: Recent Advances and Future Directions, Automation in construction 77 (2017) 1-14.

[99] V. Marcos-Meson, A. Michel, A. Solgaard, G. Fischer, C. Edvardsen, T.L. Skovhus, Corrosion Resistance of Steel Fibre Reinforced Concrete - a Literature Review, Cement and Concrete Research 103 (2018) 1-20.

[100] R.E.M. Chun-Qing Li, Z. Jian-Jun, Analytical Model for Corrosion-Induced Crack Width in Reinforced Concrete Structures, ACI Structural Journal 103(4).

[101] L. Youping, E.W. Richard, Modeling the Time-to-Corrosion Cracking in Chloride Contaminated Reinforced Concrete Structures, ACI materials journal 95(6).

[102] C.G. Berrocal, I. Löfgren, K. Lundgren, L. Tang, Corrosion Initiation in Cracked Fibre Reinforced Concrete: Influence of Crack Width, Fibre Type and Loading Conditions, Corrosion Science 98 (2015) 128-139.

[103] M. Otieno, M. Alexander, H. Beushausen, Corrosion Propagation in Cracked and Uncracked Concrete, Otieno, MB, Alexander, MG, & Beushausen, HD, Concrete repairing rehabilitation and retrofitting II (2008) 157-158.

[104] Y. Zhao, J. Yu, W. Jin, Damage Analysis and Cracking Model of Reinforced Concrete Structures with Rebar Corrosion, Corrosion Science 53(10) (2011) 3388-3397.

VITA

Kavya Vallurupalli was born in Khammam, Telangana, India. She received her bachelor of technology in Civil Engineering with Honors from Indian Institute of Technology Bombay in May 2014. She received her master of science degree in Construction Materials from University of Illinois at Urbana-Champaign in May 2017. In August 2017, she started as a PhD student in Civil, Architectural and Environmental Engineering at Missouri University of Science and Technology. In May 2022, she received a doctor of philosophy in Civil Engineering from Missouri S&T under the direction of Dr. Kamal H. Khayat.